

11 Přílohy

Biological characterization of a novel hybrid copolymer carrier system based on glycogen

Markéta Jiráťová^{1,2} · Aneta Pospíšilová³ · Maria Rabyk³ · Martin Pařízek⁴ · Jan Kovář¹ · Andrea Gálisová^{1,5} · Martin Hrubý³ · Daniel Jiráček^{1,5}

© Controlled Release Society 2017

Abstract The effective drug delivery systems for cancer treatment are currently on high demand. In this paper, biological behavior of the novel hybrid copolymers based on polysaccharide glycogen were characterized. The copolymers were modified by fluorescent dyes for flow cytometry, confocal microscopy, and in vivo fluorescence imaging. Moreover, the effect of oxazoline grafts on degradation rate was examined. Intracellular localization, cytotoxicity, and internalization route of the modified copolymers were examined on HepG2 cell line. Biodistribution of copolymers was addressed by in vivo fluorescence imaging in C57BL/6 mice. Our results indicate biocompatibility, biodegradability, and non-toxicity of the glycogen-based hybrid copolymers. Copolymers were endocytosed into the cytoplasm, most probably via caveolae-mediated endocytosis. Higher content of oxazoline in polymers slowed down cellular uptake. No strong colocalization of the glycogen-based probe with lysosomes was observed; thus,

it seems that the modified externally administered glycogen is degraded in the same way as an endogenous glycogen. In vivo experiment showed relatively fast biodistribution and biodegradation. In conclusion, this novel nanoprobe offers unique chemical and biological attributes for its use as a novel drug delivery system that might serve as an efficient carrier for cancer therapeutics with multimodal imaging properties.

Keywords Glycogen · Polymers · Drug delivery · Contrast agents · Cancer

Introduction

Nowadays, there is an increasing demand for new efficient biodegradable drug delivery systems based on natural or synthetic polymers. Synthetic polymers are considered less immunogenic, better defined, and provide more possibilities for chemical modifications. On the other hand, natural polymers offer better biodegradability, especially when their degradation depends on enzymes normally presented in cells. Hybrid copolymers containing both natural and synthetic parts may combine advantages of both these polymer types [1]. The sizes of all of these polymers can be specifically defined to enable their targeting by passive accumulation in tumor tissue. Passive accumulation of macromolecules and nanoparticles of a size below approx. 200 nm in solid tumors, known as the enhanced permeability and retention (EPR) effect, is relatively universal for many types of solid tumors and caused by high permeability of newly formed blood vessels and poor or even absent lymphatic drainage [2, 3]. The EPR effect has been noted as a tumor delivery mechanism for nanotherapeutic delivery systems [4]. However, the EPR effect is, in many cases, more complicated phenomena and depends also on tumor

Electronic supplementary material The online version of this article (<https://doi.org/10.1007/s13346-017-0436-x>) contains supplementary material, which is available to authorized users.

✉ Daniel Jiráček
daji@ikem.cz

¹ Institute for Clinical and Experimental Medicine (IKEM), Videnska 1958/9, 140 21 Prague 4, Czech Republic

² Department of Physiology, Faculty of Science, Charles University in Prague, Viničná 7, 128 44 Praha 2, Czech Republic

³ Institute of Macromolecular Chemistry of the Academy of Sciences of the Czech Republic, Heyrovsky Sq. 2, 162 06 Prague 6, Czech Republic

⁴ Institute of Physiology of the Academy of Sciences of the Czech Republic, Videnska 1083, 142 20 Prague 4, Czech Republic

⁵ Institute of Biophysics and Informatics, 1st Medicine Faculty Charles University, Salmovská 1, 12000 Prague 2, Czech Republic

intestinal fluid pressure, etc. [5, 6], and nanoparticles may also enter other organs.

Glycogen (GG), the D-glucose storage polysaccharide in almost all living organisms, which is mainly present in muscles and the liver, provides numerous benefits for use as a polymer carrier in drug delivery systems. GG is a hyperbranched sphere-shaped natural polymer [7]. The hydrodynamic diameter D_H of GG is approx. 50 nm [8], which is good for solid tumor accumulation by the EPR effect even in poorly permeable tumors [9]. Furthermore, the size of D_H (in addition to its molecular weight of approx. 10 MDa) means that GG cannot be eliminated by the kidneys directly (the renal threshold is about 9 nm in D_H which corresponds to a molecular weight of approx. 45 kDa). Therefore, GG must be biodegraded into D-glucose before it passes through renal filtration, enabling a prolonged half-life for GG in the bloodstream.

One of the advantages is that GG is an animal and human storage polysaccharide, which means that it is completely biodegradable. Another major advantage of GG is its intracellular degradation and relative inertness to amylases in the bloodstream [7, 10]. These two characteristics give GG higher stability in the bloodstream after intravenous administration. From this point of view, GG is a highly advantageous, relatively cheap material for medical use and it is still underused for these purposes with only a few published studies on the topic, e.g., GG has been used for coating of gold nanoparticles and to form hydrogels by enzymatic modification with amylose [11].

Grafting of the polysaccharide with succinic acid or biocompatible synthetic polymers can decrease the biodegradation rate for eventual EPR effect-based tumor accumulation in a predictable and adjustable manner and also allow its further chemical modification. This effect has been demonstrated only for polysaccharides other than glycogen (e.g., chitosan and dextrin) [12, 13]; therefore, we prepared a hybrid copolymer platform based on a biodegradable glycogen core and grafted with biocompatible hydrophilic poly(2-methyl-2-oxazoline) grafts. In this paper, we describe biological behavior of the novel nanoprobe platform based on poly(2-methyl-2-oxazoline)-grafted glycogen and compared it with labeled glycogen to determine the effect of grafting. We have proven that grafting with hydrophilic biocompatible poly(2-methyl-2-oxazoline) allows to fine-tune biodegradation rate and also that externally added glycogen (which is not normally present in blood plasma) is fully biodegradable *in vivo*.

We modified the GG conjugates with the fluorescent dyes for examination by flow cytometry and confocal microscopy. We also prepared a modified GG with the covalently bound fluorescent agent Dyomics 615, which can be tracked by fluorescence imaging. Moreover, the contrast agent, gadolinium(III)-DOTA, intended for magnetic resonance imaging (MRI) was also bound to the same molecule of the modified GG allowing its tracking by MRI [8]. Taken together, this new hybrid copolymer carrier system can serve as a

multimodal imaging probe. In the future, there could be bound also various types of therapeutics.

Materials and methods

Chemical part

Materials

The Dyomics 615 NHS ester was purchased from Exbio Praha a.s. (Prague, Czech Republic), the DOTA-NHS ester was purchased from Macrocyclics Inc. (Dallas, TX, USA), and the Sephadex G-25 was purchased from AP Czech Ltd. (Prague, Czech Republic). Dialysis tubing (Spectra/Por 3, molecular weight cutoff 6000–8000 Da) was purchased from Serva Electrophoresis GmbH (Heidelberg, Germany). All other chemicals were purchased from Sigma-Aldrich Ltd. (Prague, Czech Republic).

The conjugate GG-GdDOTA-Dy615 was prepared according to the reference [8], as was the amino group containing glycogen (GG-NH₂) [14]. FTIR spectra of prepared GG conjugates are presented in supplemental data (S.Fig. 1).

Synthesis of amino-group-terminated glycogen-graft-poly(2-methyl-2-oxazoline) (GG-PMeOx-1 and GG-PMeOx-3)

Glycogen-graft-poly(2-methyl-2-oxazolines) were synthesized analogously to the procedure described previously for glycogen-graft-poly(2-isopropyl-2-oxazolines) [14]. 2-Methyl-2-oxazoline (3.15 ml, 37.2 mmol) and allyl bromide (0.595 ml, 6.9 mmol) were dissolved in anhydrous acetonitrile (5 ml), after which the solution was polymerized overnight at 70 °C under argon atmosphere. The molecular weight of polyoxazoline was determined by mass spectrometry (ESI-MS): number-average molecular weight $M_n = 672$ Da, polydispersity $PDI = M_w/M_n = 1.11$, where M_w is the weight-average molecular weight.

Glycogen (type II from oyster, 2.3 g) was mixed with dimethyl sulfoxide (53 ml), and the mixture was stirred at 70 °C until all glycogen had dissolved (approx. 3 h). The solution was dried by the addition (10 ml) and subsequent evaporation of anhydrous toluene and then split into two dry flasks [45 g and 15 g for GG-PMeOx-1 and GG-PMeOx-3, respectively]. Sodium hydride (0.75 g and 0.25 g of a 60% dispersion in mineral oil for GG-PMeOx-1 and GG-PMeOx-3, respectively) was added to the glycogen solutions and the two mixtures were stirred at 70 °C until hydrogen gas evolved (approx. 2 h). Orange viscous solutions were obtained. A solution of polyoxazoline was then added [1.2 g for GG-PMeOx-1 and 3.50 g for GG-PMeOx-3, respectively], and the mixtures were vigorously stirred for 3 h at 70 °C. Water (approx. 10 ml) was

added, and the mixtures were dialyzed against water for 72 h (with a molecular weight cutoff of 6000–8000 to remove unbound POX and other components from the reaction mixture) and washed with diethyl ether (30 ml) to remove residual mineral oil. The aqueous phase was then freeze-dried.

The content of polyoxazoline (% wt.) was calculated according to the following equation:

$$w_{\text{PMeOx}} = \frac{w_N}{w_{N, \text{PMeOx}}} \times 100\%$$

where w_N is the content of nitrogen in the sample and $w_{N, \text{PMeOx}}$ is the calculated content of nitrogen in the polyoxazoline graft (15.12% in our case). Polyoxazoline content was found to be 4% (GG-PMeOx-1) and 44% (GG-PMeOx-3), respectively.

Cysteamine was added to the glycogen-graft-poly(2-methyl-2-oxazolines) according to a procedure described previously for allylated glycogen [8]. The yield from amino-group-terminated glycogen-graft-poly(2-methyl-2-oxazolines) was as follows: 220 mg (88%) of GG-PMeOx-1-NH₂ and 115 mg (46%) of GG-PMeOx-3-NH₂.

Preparation of dansyl-labeled glycogen-graft-poly(2-methyl-2-oxazolines) (GG-PMeOx-1-Ds and GG-PMeOx-3-Ds)

Dansyl glycine (200 mg, 0.65 mmol) and N-hydroxysuccinimide (75 mg, 0.65 mmol) were dissolved in THF (10 ml), and the solution was cooled to 0–5 °C. A solution of DCC (154 mg, 0.75 mmol) in THF (5 ml) cooled to 0–5 °C was added. The mixture was stirred at 0–5 °C for 2 h and then overnight at room temperature. Eighty percent acetic acid (12.5 µl, 0.15 mmol) was added, and the mixture was stirred for additional 0.5 h at room temperature. Dicyclohexylurea was filtered off, and the filtrate was rotoevaporated. Dansylglycine-NHS ester (Ds-NHS) was obtained as yellow powder in quantitative yield (271 mg). ESI MS: m/z : calcd for C₁₈H₂₀N₃O₆S 406.44 [M+H]⁺, found 406.08 [M+H]⁺. Due to its low stability, which was reported previously [15], product was not fully characterized and was used without further purification.

GG-PMeOx500-1-NH₂ or GG-PMeOx500-3-NH₂, respectively (40 mg) was dissolved in DMSO (0.9 ml). Ds-NHS (20 mg) was added, and the mixture was stirred for 0.5 h at room temperature. Water (0.6 ml) was added, and the solution was purified twice using gel permeation chromatography (Sephadex G-25, H₂O as eluent, bed volume of 150 ml). The product was freeze-dried.

The content of dansyl moiety was determined spectrophotometrically in water at 320 nm ($\epsilon = 3400 \text{ cm}^{-1}/\text{M}$ —the average value for dansyl-marked proteins [16]) and was found to

be 74 pmol/mg for GG-PMeOx500-1-Ds and 28 pmol/mg for GG-PMeOx500-3-Ds.

Preparation of fluorescein isothiocyanate (FITC)-labeled glycogen and glycogen-graft-poly(2-methyl-2-oxazolines) (GG-FITC and GG-PMeOx-1-FITC)

GG-NH₂ or GG-PMeOx500-1-NH₂ (100 mg) was dissolved in 5 ml of 0.1 M Na₂CO₃, and 0.5 ml of the FITC solution (in DMSO, 1 mg/ml) was added. As a grafting mechanism aminolysis of the isothiocyanate group on FITC with the primary amino groups on GG/GG-conjugate to form thiourea linkage was used. The mixture was stirred overnight and then purified twice using gel permeation chromatography (Sephadex G-25, H₂O as eluent, bed volume of 150 ml). The product was freeze-dried.

The content of fluorescein moiety was determined spectrophotometrically in 0.1 M borate buffer (pH = 9.3) at 495 nm ($\epsilon = 77,000 \text{ cm}^{-1}/\text{M}$) and was found to be 1.7 nmol/mg for GG-FITC and 0.2 nmol/mg for GG-PMeOx500-1-FITC. The conjugation efficiency was calculated from determined amount of FITC in the final conjugates versus its concentration in the reaction mixture and was found to be 20.1 and 2.4% for GG-FITC and GG-PMeOx500-1-FITC, respectively.

FTIR and NMR of GG-FITC and GG-PMeOx500-1-FITC spectra are presented in supplemental data (S.Fig. 2).

Biological part

Cell line

The HepG2 cell line (ATCC® HB-8065™, Czech Republic) was chosen as a suitable model, because it is a cell line derived from hepatocellular carcinoma, and thus, these cells are able to utilize glycogen in large extent. This cell line was used for all in vitro experiments. The cells were incubated under standard conditions (37 °C, 5% CO₂) in MEM incubation medium (Minimum Essential Medium) without phenol red from Gibco® by LifeTechnologies™ (USA) in order to minimize background during fluorescent microscopy measurement. Fetal bovine serum, L-glutamine (stock solution 200 mM), a non-essential amino acid solution and penicillin/streptomycin (stock solution 10,000 units of penicillin and 10 mg of streptomycin per 1 ml) were added to the media. All of them, excluding the fetal bovine serum, were purchased from Sigma-Aldrich Ltd. (Prague, Czech Republic) and diluted in medium at a final concentration of 5%. The fetal bovine serum was purchased from Gibco® by LifeTechnologies™ (Waltham, MA, USA), and final concentration in media was 10%.

Animal model

Six C57BL/6 mice (Anlab, Czech Republic) were used as an experimental model. Another three C57BL/6 mice (Anlab, Czech Republic) were used as negative controls. The mice were kept in a conventional breeding facility under a 12/12 light cycle regimen, with free access to pelleted food and water.

All protocols were approved by the Ethical Committee of the Institute for Clinical and Experimental Medicine and the experiments were carried out in accordance with the European Communities Council Directive (86/609/EEC).

Fluorescence measurement

The HepG2 cells were incubated in media with the addition of modified glycogen (GG-GdDOTA-Dy615, GG-PMeOx-1-Ds, or GG-PMeOx-3-Ds) to the final concentration at 0.3% and a total volume of 5 ml. Two hundred microliters of incubation media were collected at time points 5 min and then at 1, 2, 4, 8, 24, 48, and 120 h, respectively, after the addition of modified GG with a fluorescent label. The collected samples from the incubation medium were transferred to a 96-well plate and measured immediately on the Synergy™ 2 Multi-Mode Reader from BioTek@Instruments, Inc. (USA) using the following band-pass filters: Dyomics 615: 575/15-nm excitation filter and 620/40-nm emission filter; dansyl 320/20-nm excitation filter and 485/20-nm emission filter. Results were adjusted to the actual volume of media after each sampling.

Confocal microscopy

In their exponential phase of growth, the HepG2 cells were incubated for 4 h in media with a 0.3% concentration of modified glycogen (GG-PMeOx-1-Ds, GG-GdDOTA-Dy615, or GG-PMeOx-1-FITC). The cells were washed with Hanks' balanced salt solution (HBSS, Biosera, France), and fluorescent dyes were added in concentrations according to the producer's manual (60–70 nM for LysoTrackers® and 1 µg/ml for LysoTrackers® and 20 min for Hoechst 33342 [17, 18]). All fluorescent dyes were purchased from Invitrogen™ by Life Technologies, Czech Republic. After incubation, cells were washed with HBSS and measured on a Leica SP2 AOBS confocal microscope (objective: HCX PL APO CS 63.0 × 1.20 W CORR). Where the cells were incubated with the addition of extra glucose, we used a 22 mM final concentration of glucose in the medium. The medium with 22 mM D-glucose (Sigma-Aldrich Ltd., Prague, Czech Republic) was also used during incubation with modified glycogen or fluorescent probes.

Inhibition of internalization into the cells

The HepG2 cells were seeded into the 24-well plates (3.0×10^5 cells/ml) and incubated for 4 days in a humidified atmosphere (37 °C, 5% CO₂). The cells were divided into three groups in triplicates (with GG conjugate only, GG conjugate and hypertonic sucrose, or GG conjugate and methyl-β-cyclodextrin (MBCD)) and a control group in duplicates (untreated HepG2 cells). Four days after seeding, the cells were preincubated for 30 min with one of the inhibitors (0.4 M hypertonic sucrose or 4 mM MBCD, respectively). The same inhibitor was also present during subsequent incubation with GG-PMeOx-1-FITC. At the end of the 4-h incubation with GG-PMeOx-1-FITC, the cells were washed with HBSS, trypsinized, collected, and measured immediately on a flow cytometer FC500 (Beckman Coulter, USA). The 7AAD (20 µl, Molecular Probes™, Life Technologies, Czech Republic) was added before each measurement for 10 min to distinguish live from dead and debris cells. Each measurement was performed for 300 s.

Methylthiazolyldiphenyl-tetrazolium bromide (MTT) assay

The MTT assay was performed according to the standard protocol [19]. The highest concentration involved (0.6%) reflects the doubled concentration that was used for all other in vitro experiments. Other concentrations were prepared by fivefold serial dilution of the initial concentration. After a 24-h incubation with modified GG, the cells were washed with HBSS; then, 200 µl of fresh media were added, and cells were incubated for another 5 days. The medium was removed and the MTT solution (5 mg/ml in MEM, 250 µl per well) was added for 6 h. The MTT solution was changed for dimethyl sulfoxide (DMSO, 200 µl per well) and glycine buffer (30 µl per well). Absorbance at 600 nm was immediately measured on the Multi-Mode Reader (Synergy™ 2, BioTek@Instruments, Inc., USA). The tests were held in octuplicates. Both MTT and DMSO were purchased from Sigma-Aldrich Ltd. (Prague, Czech Republic).

In vivo fluorescence imaging

One hundred microliters of GG-Dy615 stock solution (14.3 mg of GG-GdDOTA-Dy615 in 1.2 ml 0.15 mol/L aqueous NaCl) were administered by intravenous injection into the tail vein of the experimental animals. The mice were anesthetized with 2% isoflurane (Chiesi Pharmaceuticals GmbH, Austria) and shaved in the abdominal area before scanning in order to minimize scattering and attenuation of optical signal. In vivo fluorescence imaging of mice was performed at an IVIS® Lumina XR optical imager (PerkinElmer Inc., USA) with 5-min exposure time, excitation filter 605 nm and emission filter Cy5.5 (695–770 nm). The mice were measured

immediately and then 2, 6, and 24 h after application of GG-Dy615. After the last measurement, all mice were sacrificed by overdose of anesthesia, and fluorescence of the internal organs (liver, spleen, kidneys) was measured with the same parameters used in *in vivo* measurement. Evaluation of fluorescent signal was performed using either region of interest (ROI) covering the whole mouse body or separate internal organs, for which the average radiant efficiency ($[\text{photon}/\text{cm}^2/\text{sr}]/[\mu\text{W}/\text{cm}^2]$) was measured and compared.

Statistical methods

One-way analysis of variance (ANOVA) was calculated for each of the MTT assays using the GraphPad InStat 3 (GraphPad Software, Inc., USA) program.

Results

Glycogen-*graft*-poly(2-methyl-2-oxazolines) (GG-PMeOxs) were prepared analogously to the previously described procedure for thermoresponsive glycogen-*graft*-poly(2-isopropyl-2-oxazoline-*co*-2-butyl-2-oxazolines) [12]. Cysteamine was added analogously to a procedure we previously published for allylated glycogen [8]. This involved an amino group containing glycogen conjugates, which were subsequently marked with different fluorescent dyes, leading to fluorescent glycogen conjugates in high yields with fluorophore content sufficient for both *in vitro* and *in vivo* imaging. Rate of intracellular degradation, cytoplasmic localization, and cytotoxicity parameters of these hybrid copolymers were then compared to the biological properties of the non-poly(2-methyl-2-oxazoline)-containing conjugate GG-GdDOTA-Dy615 to determine the effect of poly(2-methyl-2-oxazoline) conjugation.

Our biological experiments first addressed the dependence of the endocytosis rate on glycogen grafting density. The three different types of materials were used—GG-GdDOTA- and two dansyl-labeled glycogen-*graft*-poly(2-methyl-2-oxazolines), differing in the content of poly(2-methyl-2-oxazoline) grafts (GG-PMeOx-1-Ds with 4 wt.% of poly(2-methyl-2-oxazoline) and GG-PMeOx-3-Ds with 44 wt.% of poly(2-methyl-2-oxazoline)). In the case of the non-poly(2-methyl-2-oxazoline)-containing GG-GdDOTA-Dy615 (Fig. 1a), there was a constant decrease of fluorescence in incubation media. On the other hand, in the case of both GG-PMeOxs, there was a constant decrease in the first 4 h only, after which the level of fluorescence in the media increased again (Fig. 1b). A comparison between the two different types of GG-PMeOxs showed that the initial decrease in the level of fluorescence in the incubation media (corresponding to the cellular uptake) was greater for GG-PMeOx with the lower content of poly(2-methyl-2-oxazoline) than for the one with the higher content of polyoxazoline (Fig. 1c).

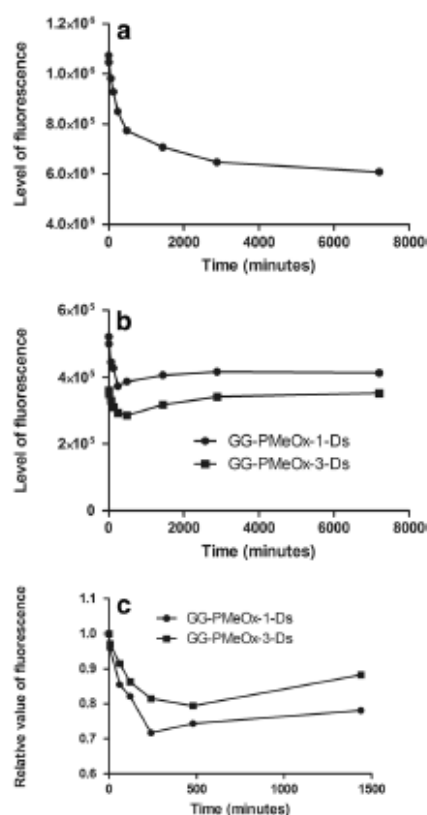


Fig. 1 Changes in fluorescence levels in media. Medium a with GG-GdDOTA-Dy615 (sensitivity 50), b with GG-PMeOx-1-Ds or GG-PMeOx-3-Ds (sensitivity 80), and c with GG-PMeOx-1-Ds or GG-PMeOx-3-Ds for the first 8 h

Results from the confocal fluorescent microscopy with confirmed the absence of GG-PMeOx-1-Ds in the nucleus and the presence of the fluorescent-labeled dansyl of the polymer-modified glycogen in the cytoplasm (Fig. 2). This presence was not continuous, but we were able to observe a more intensive fluorescence in clusters. These clusters were not more frequent in specific areas but were continuously present in the cytoplasm of the HepG2 cells.

Similar results to GG-PMeOx-1-Ds were obtained for glycogen conjugate without poly(2-methyl-2-oxazoline)—GG-GdDOTA-Dy615 (Fig. 2).

Two types of colocalization studies were also performed. First, we carried out colocalization of GG-GdDOTA-Dy615 with Hoechst 33342 (cell nucleus-staining fluorescent dye with a high intercalation affinity to DNA) to further confirm the absence of modified glycogen in the nucleus (Fig. 2). We did not observe any colocalization of the two types of fluorescent labels used. Pearson's coefficient (calculated for Dyomics 615 in combination with Hoechst 33342) was below 0.2.

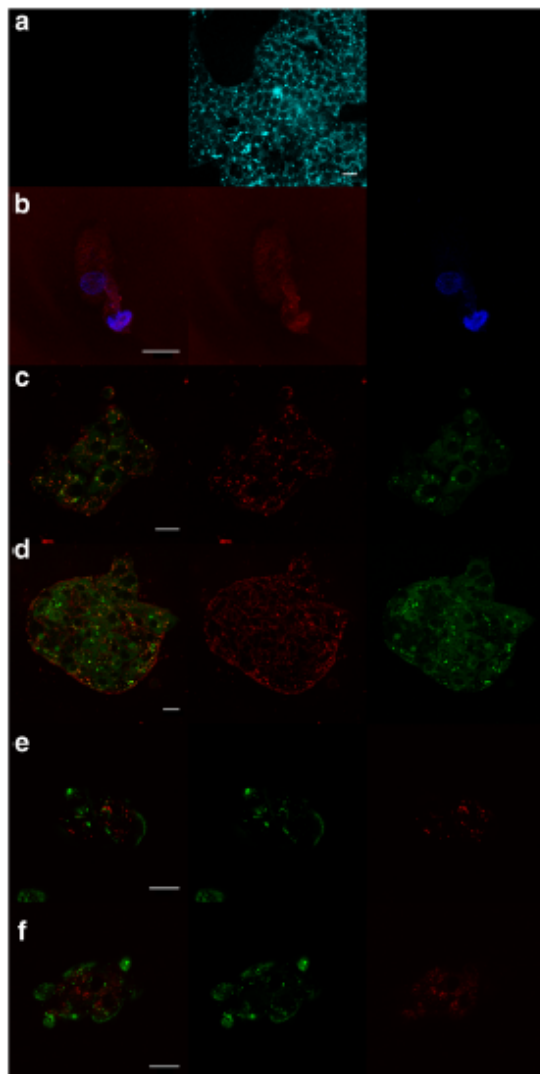


Fig. 2 Images from confocal microscopy (Leica SP2). HepG2 cells incubated with three different types of modified glycogen (0.3% solution in incubation media for all types of modified GG) are displayed. The left column shows merged images, the middle column displays fluorescent signals for modified GG in HepG2 cells, and the right column displays fluorescent signals for Hoechst 33342, LysoTracker® Green and LysoTracker® Deep Red. Scale bars 20 μ m. Rows: **a** GG-PMeOx-1-Ds, **b** GG-GdDOTA-Dy615 with Hoechst 33342, **c** GG-GdDOTA-Dy615 with LysoTracker® Green, **d** GG-GdDOTA-Dy615 with LysoTracker® Green and D-glucose addition (final concentration 22 mM), **e** GG-PMeOx-1-FITC with LysoTracker® Deep Red, and **f** GG-PMeOx-1-FITC with LysoTracker® Deep Red and D-glucose addition (final concentration 22 mM)

The second colocalization study was carried out in order to precisely determine the metabolism of the externally administered glycogen to assess if it is degraded inside lysosomes or by

enzymes that are used for intracellular glycogen. All values of Pearson's coefficient obtained from confocal microscopy that compares colocalization of the signal from fluorophore on the conjugate and the particular LysoTracker® (GG-PMeOx-1-FITC, 0.1–0.18; GG-GdDOTA-Dy615 incubated without adding extra D-glucose, 0.3–0.45; GG-GdDOTA-Dy615 incubated with extra D-glucose, 0.42–0.46) were relatively low. It indicates a very weak correlation for GG-PMeOx-1-FITC and a moderate correlation for GG-GdDOTA-Dy615. The addition of D-glucose had only a negligible effect.

Flow cytometry studies using two different types of inhibitors, hypertonic sucrose for clathrin-mediated endocytosis and MBCD for caveolae-mediated endocytosis, showed decreased x-mean of fluorescence upon cells incubation with GG-PMeOx-1-FITC and MBCD (Fig. 3).

A classic MTT cytotoxicity assay was used to determine toxicity of our polymers. This test confirmed non-toxicity of the all used concentrations of GG-PMeOx-1-FITC, and these levels of viability were similar to the HepG2 control cells (Fig. 4a). Results for GG-GdDOTA-Dy615 indicate that this type of modified glycogen is also non-toxic to cells (Fig. 4b). Although viability continuously rose with the lower concentrations, we did not observe any significant difference in viability between treated cells and control cells. Cell viability was also not affected by incubation with native (unmodified) glycogen (Fig. 4c).

After *in vitro* tests, the probe GG-Dy615 containing a fluorescent dye suitable for fluorescence imaging was *in vivo* administered into the experimental animals and *in vivo* biodistribution, biodegradation, and elimination of the probe was assessed by optical imaging. Average radiant efficiency exhibited an initial decrease after *in vivo* application for the ROI covering the whole mouse body (Fig. 5). Over 24 h, fluorescence signal was still detectable and slowly increasing after initial decrease. After sacrifice of the animals, fluorescent signals from the internal organs were acquired (Fig. 6). The liver and kidneys were fluorescently positive. In contrast, fluorescent signal from the spleen was just negligible. The detected fluorescent signals in experimental mice were one order bigger compared to control animals (Fig. 6).

Discussion

Biological behavior of a novel glycogen-based polymer with biocompatible hydrophilic poly(2-methyl-2-oxazoline) grafts ensuring its tunable biodegradability rate and solid tumor targeting due to the EPR effect was examined for the first time.

All of the differences in the endocytosis rate that occurred between different types of modified glycogens (GG-GdDOTA-Dy615, GG-PMeOx-1-Ds, and GG-PMeOx-3-Ds) originated in their chemical structure. Unsurprisingly, the major difference was between the two most different groups of

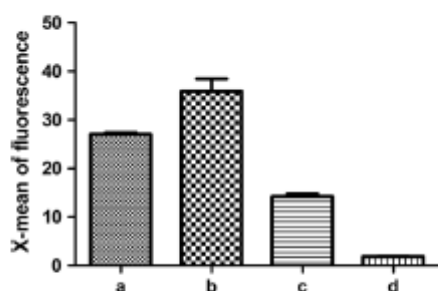


Fig. 3 Results from flow cytometry studies; determination of endocytosis type using two types of inhibitors. HepG2 cells were incubated with GG-PMeOx-1-FITC for 4 h. Columns represent (a) modified glycogen alone; (b) modified glycogen plus hypertonic sucrose; (c) modified glycogen plus MBCD; (d) untreated control cells

modified glycogens (GG-GdDOTA-Dy615 versus both types of GG-PMeOx-Ds). This difference in the levels of fluorescence in the incubation media over the course of time was likely due to the non-covalent interactions between organelles in cells and fluorescent label Dyomics 615 released after glycogen carrier degradation in low-molecular-weight form. Therefore, the most plausible scenario is that the fluorescent label, but not the whole molecule of glycogen, remained inside the cells and was not transported back into the incubation media. In the case of both types of GG-PMeOx-Ds, there was a decrease in the level of fluorescence during the first 4 h, after which the level of fluorescence in the incubation media started to rise again. We assume that degradation fragments [non-biodegradable poly(2-methyl-2-oxazoline) chains] were transported from the cells with the fluorescent label (dansyl) too. Most probably, this was because poly(2-methyl-2-oxazoline) is biocompatible and also fluorescent-labeled dansyl does not stick to intracellular components, especially because it remains on poly(2-methyl-2-oxazoline).

A higher degree of functionalization of polymer grafts should affect the endocytosis rate. Uptake is slower for GG with the higher content of polyoxazoline because poly(2-methyl-2-oxazoline) makes the glycogen core stealthier for cells. These findings are in accordance with previous studies focusing on dextrin succinylation, which is also a type of chemical functionalization. Dextrin with a higher level of succinylation shows slower biodegradation [12, 13]. Slower uptake of GG with a higher content of polyoxazoline may also contribute to prolonged blood circulation time, which can be beneficial for diagnostic purposes.

Confocal microscopy results showed that Pearson's coefficient for Dyomics 615 in combination with Hoechst 33342 was below 0.2, which indicates that colocalization of the two used dyes was random, quite possibly due to noise in the picture. It means that modified GG is not present in the nucleus. This result is also in accordance with our previous studies [8].

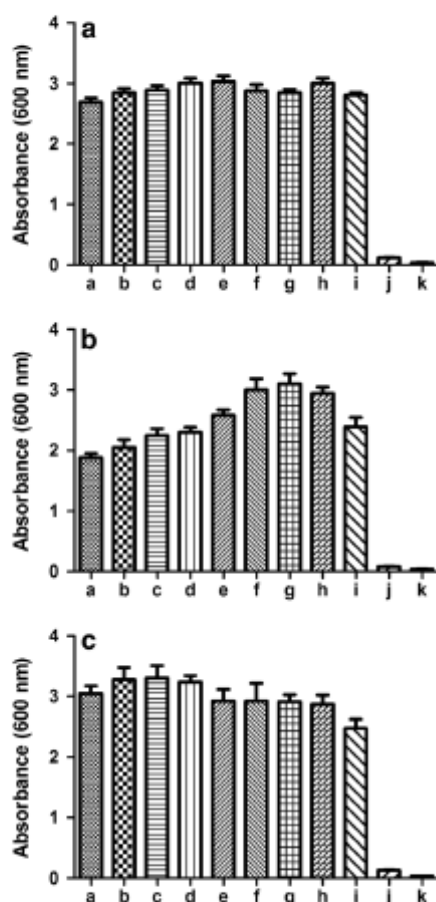
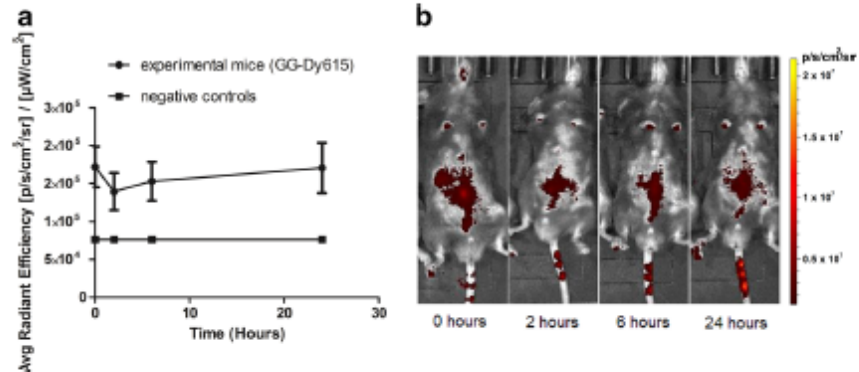


Fig. 4 MTT assay results for a GG-PMeOx-1-FITC, b GG-GdDOTA-Dy615, and c GG without modifications; presented as mean \pm SEM ($n = 8$). Columns represent HepG2 cells exposed to (a) 0.6% concentration of modified/unmodified GG; (b) 0.12% concentration of modified/unmodified GG; (c) 0.024% concentration of modified/unmodified GG; (d) 0.0048% concentration of modified/unmodified GG; (e) 0.00096% concentration of modified/unmodified GG; (f) 0.000192% concentration of modified/unmodified GG; (g) 0.0000384% concentration of modified/unmodified GG. Columns represent (h) control A; (i) control B; (j) incubation medium without cells and with MTT; (k) incubation medium alone. One-way ANOVA was performed for all MTT assays. Differences between j, k, and other columns were always at a level of $P \leq 0.001$ (not indicated in the graphs)

Glycogen can be degraded in two ways. The first occurs via physiological degradation by specific enzymes for glycogen. The second involves a rarer pathway which occurs in lysosomes by α -glycosidase [20]. Because glycogen is not present extracellularly under normal conditions, we try to distinguish which pathway is utilized. Results from confocal microscopy colocalization studies indicate that the physiological pathway used by glycogen specific enzymes is the one that is most likely used for the degradation of endogenous glycogen. We

Fig. 5 **a** Fluorescence signals in the C57BL/6 mice after i.v. administration of GG-Dy615 in comparison with the negative controls—the C57BL/6 mice without administration of GG-Dy615. **b** Example of fluorescence signal changes from one C57BL/6 mouse after i.v. administration of GG-Dy615. The scale bar on the right is valid for all four images and is presented as radiance ($\text{pW}/\text{cm}^2/\text{sr}$)—the minimum is $1.19\text{e}6$ and maximum is $2.14\text{e}7$

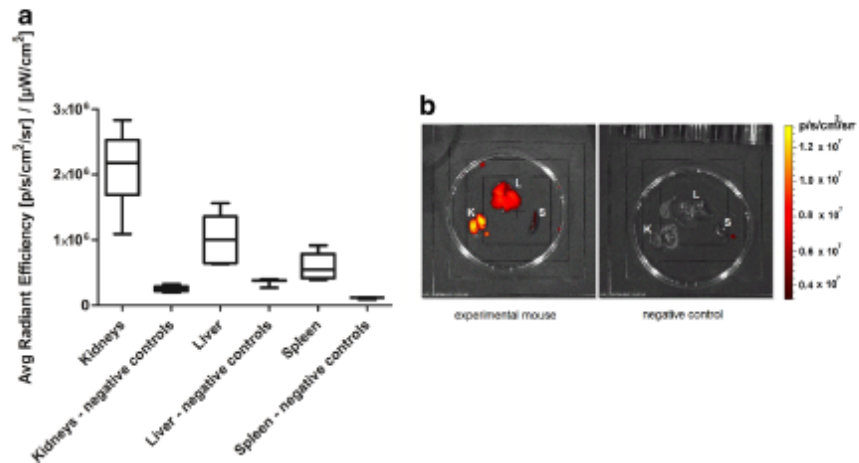


can assume that the degradation of all modified GGs is mostly dependent on the specific physiological pathway, in combination with lysosomal degradation. If degradation of modified GG is reliant on the physiological pathway for endogenous glycogen, it favors the hypothesis that exogenously administered glycogen is treated like the cells' own glycogen. This could be beneficial for its potential use as a diagnostic and therapy drug delivery system. The lower Pearson's coefficient observed obtained for GG-PMeox-1-FITC in comparison with GG-GdDOTA-Dy615 (GG-PMeOx-1-FITC, 0.1–0.18; GG-GdDOTA-Dy615 incubated without adding extra D-glucose, 0.3–0.45) may have been due to the pH-dependent fluorescent signal of FITC.

It is known that glycogen should be located in the cytoplasm of hepatic cells in the absence of glucose, be completely absent in the nucleus and be of no more prominent density close to the cytoplasmic membrane [21–23]. This is in accordance with our findings, as we did not add any extra glucose to hepatic cells either. The presence of clusters with more intensive fluorescence perhaps indicates that (fluorescent-labeled)

glycogen is associated with its enzymes in what are known as glycosomes [10]. Nonetheless, we did not find any visible distinct difference in modified GG storage between cells that were either incubated without adding extra glucose or by adding extra D-glucose after analysis of microscopic pictures by experienced users. This unexpected difference, however not statistically proved, between physiological states may be possibly explained by the fact that we had already used a whole molecule of modified GG. In its physiological state, glycogen is synthesized by glycogen synthase (for HepG2 cells it is synthesized by liver glycogen synthase (LGS)) from glucose. When cells are in a high glucose state, LGS is translocated from cytosol to proximity of the cytoplasmic membrane [21] and glycogen is synthesized from externally added D-glucose on the cytoplasmic membrane towards the center of the cells [24]. Translocation of LGS and changes in glycogen synthesis most probably do not exert any impact on storage of this whole, already synthesized, modified glycogen molecule. Therefore, in our case, our conjugate was the subject of degradation, and not glycogen resynthesis.

Fig. 6 **a** Average radiant efficiency for organs (kidneys, liver, and spleen) from the C57BL/6 mice 24 h after i.v. application of GG-Dy615 in comparison with organs from the negative controls—the C57BL/6 mice without application of GG-Dy615. **b** Comparison of fluorescence signal from the C57BL/6 mice 24 h after i.v. application of GG-Dy615 in comparison with organs (K, kidneys; L, liver; S, spleen) from negative controls—the C57BL/6 mice without application of GG-Dy615. The scale bar on the right is valid for both images and is presented as radiance ($\text{pW}/\text{cm}^2/\text{sr}$)—the minimum is $3.18\text{e}6$ and maximum is $1.33\text{e}7$



We also studied the uptake mechanism of the GG conjugates into the cells. MBCD serves as an inhibitor for caveolae-mediated endocytosis. Because x -mean of fluorescence was lowered in case of adding MBCD to the cells media, we can assume that this type of endocytosis occurred in the case of exogenously administered GG. Our findings are in agreement with other studies which conclude that caveolae-mediated endocytosis is preferred in most cases when designating endocytosis type with several types of dendrimers other than GG [25]. However, there is no such study for the same type of dendrimer that we used for exact comparisons (GG). Moreover, endocytosis of GG-PMEOX-1-FITC was inhibited only partially by MBCD, which may suggest that GG uses other means of entering cells that are more complex.

The fluorescent/MRI label is always non-cleavably covalently bound to the biggest fragment produced (i.e., polyoxazoline in the case of polymer-glycogen conjugates) and is stable. The other degradation product is D-glucose, which is metabolized. And therefore, the most plausible scenario is that whole molecule is endocytosed by caveolae-mediated endocytosis and then glycogen is degraded into D-glucose inside the cells by its specific enzymes. The fragments of modified glycogen should be up to tens of nanometers, and these are typically exocytosed within tens of minutes-several hours [26].

Results from the MTT assays completely support our hypothesis that modified glycogen is non-toxic, because it is physiologically present in almost all living organisms. The non-significantly lower absorbance level in higher concentrations of GG-GdDOTA-Dy615 is most probably caused by gadolinium (Gd^{3+}), which may be toxic when cleaved out from a molecule of glycogen. Toxicity of Gd^{3+} has been proved in many previous studies [27–30]. However, Gd^{3+} chelates are approved for use in clinical practice and the high level of concentration that we used as a starting concentration is not generally used in vivo. We also found native glycogen non-toxic to HepG2 cells. Therefore, we may suppose that the cytotoxicity of modified glycogen was not due to glycogen alone, but caused by its modifications. This in turn indicates that it should be possible to lower cytotoxicity through the careful selection of fluorescent probes, ligands, MRI contrasts, etc. for future prospective clinical use.

Finally, elimination of GG-Dy615 in vivo through the kidneys in a few hours correlates with data obtained by MRI [8]. Moreover, our system is biodegradable with scope for further modifications. Initial decrease (2 h time point) of fluorescence signal could be caused by fact that GG-Dy615 was not just in superficial vessels and at application site as it was immediately after application but also GG-Dy615 was not yet concentrated in the liver and kidneys. The increase in the fluorescence signal from the kidneys after 24 h indicates that GG-Dy615 was degraded, since the size of the whole GG-Dy615 molecule was above the renal threshold. Therefore, it is most

likely that only the fluorescence label alone (Dyomics 615) was detected in the kidneys. Fluorescent signal from the spleen was quite low (in comparison to controls that did not get GG-Dy615); thus, we can assume that modified glycogen was not taken up by the reticuloendothelial system in great amounts.

Conclusions

We proved high potential of our novel glycogen-based copolymers for medical use due to no adverse effect during in vitro and in vivo experiments. The copolymers are non-toxic, biocompatible, and possess tunable biodegradable using poly(2-methyl 2-oxazoline) grafting. We showed that these hybrid copolymers avail more caveolae-mediated in comparison to clathrin-mediated endocytosis and that they are located in the cytoplasm after endocytosis. In vitro and in vivo experiments confirmed relatively fast in vivo biodistribution. Thanks to these attributes, the glycogen-based probes are superior to commonly used drug delivery systems and would be suitable as polymer carriers for biomedical use, particularly for its prospective use for cancer-diagnostic and therapeutic purposes.

Acknowledgements This work was supported by the Grant Agency of the Ministry of Health, Czech Republic [grant number 15-25781a], the Czech Science Foundation [grant number 13-08336S], the Charles University in Prague (Faculty of Science), and project GA UK [grant number 282216], and the confocal microscopy part (M. Pafizek) was supported by the Czech Science Foundation [grant number P108/12/1168]. We would like to thank Alena Sekerková for help with flow cytometry measurements.

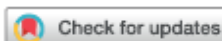
Compliance with ethical standards All protocols were approved by the Ethical Committee of the Institute for Clinical and Experimental Medicine and the experiments were carried out in accordance with the European Communities Council Directive (86/609/EEC). All institutional and national guidelines for the care and use of laboratory animals were followed.

Conflict of interest The authors declare that they have no conflict of interest.

Abbreviations 7-AAD, 7-aminoactinomycin D; DMSO, dimethyl sulfoxide; DOTA, 1,4,7,10-tetraazacyclododecane-1,4,7,10-tetraacetic acid; EPR, enhanced permeability and retention; ESI-MS, electrospray ionization mass spectrometry; FITC, fluorescein isothiocyanate; GG, glycogen; HBSS, Hanks' Balanced Salt Solution; LGS, liver glycogen synthase; MBCD, methyl- β -cyclodextrin; MEM, Minimum Essential Medium; MRI, magnetic resonance imaging; NHS, N-hydroxysuccinimide ester; ROI, region of interest

References

1. Cho K, Wang X, Nie S, Chen ZG, Shin DM. Therapeutic nanoparticles for drug delivery in cancer. *Clin Cancer Res Off J Am Assoc Cancer Res.* 2008;14:1310–6.

Cite this: *J. Mater. Chem. B*, 2018,
6, 2584Received 6th November 2017,
Accepted 3rd January 2018

DOI: 10.1039/c7tb02888a

rsc.li/materials-b

Mannan-based conjugates as a multimodal
imaging platform for lymph nodes†M. Rabyk,^a A. Galisova,^b M. Jiratova,^b V. Patsula,^a L. Srbova,^a L. Loukotova,^a
J. Parnica,^a D. Jirak,^b P. Stepanek^a and M. Hruby^{✉*}

We show that mannan-based conjugates possess exceptional features for multimodal imaging because of their biocompatibility, biodegradability and self-targeting properties. Two new mannan conjugates, containing a gadolinium complex and a fluorescent probe, one based only on polysaccharide and the other one comprising polysaccharide with poly(2-methyl-2-oxazoline) grafts, were prepared and simultaneously visualized *in vitro* and *in vivo* by magnetic resonance and fluorescence imaging. The synthesis of these mannan-based complexes was based on alkylation with allyl bromide or grafting with poly(2-methyl-2-oxazoline) chains, followed by a thiol-ene click reaction with cysteamine to introduce primary amino groups into their structure. Finally, the obtained conjugates were functionalized with contrast labels using the corresponding *N*-hydroxysuccinimide esters. When used to detect lymph nodes, the polymers showed better imaging properties than a commercially available contrast agent.

Introduction

Recently, the usage of polysaccharides for pharmaceutical and biomedical applications has been the subject of numerous studies^{1,2} because of their unique physicochemical and biological properties.^{3,4} Polysaccharides may serve as carriers suitable for the construction of delivery systems for drugs,⁵⁻⁷ as vaccine adjuvants,⁸ as components of designed gene delivery systems⁹ and tissue engineering scaffolds,¹⁰⁻¹² etc. Such carbohydrate-based systems are often produced by polyelectrolyte complexation,¹³ covalent chemical modification of the polysaccharide,¹⁴ chemical crosslinking¹⁵ or grafting with a synthetic polymer.¹⁶

Polysaccharides may also be used for the preparation of diagnostic probes.¹⁷⁻¹⁹ Although most of the studies conducted in this biomedical field are dedicated to cancer diagnostics, there is also a need to investigate methods for detecting possible complications related to cancer. One of these complex issues connected with cancer is the detection of sentinel lymph nodes (SLNs). As part of immune system, lymph nodes (LNs) play a very important role in the body. Among other types of cells, they include B- and T-lymphocytes, which monitor lymph for the presence of "foreign" bacteria and viruses; when such objects are detected, they become activated by migratory

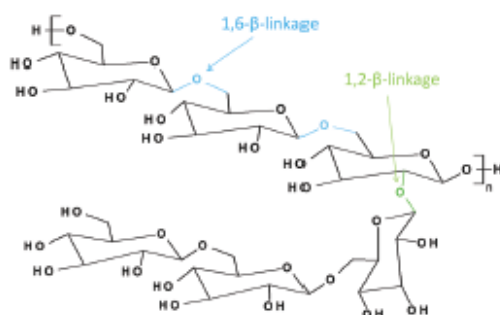
dendritic cells (DC), and an immune response is subsequently triggered.²⁰

LNs also play a key role in metastatic process. Although the mechanism is not absolutely clear yet, it is well known that because of the large cavity of lymph vessels and slow velocity of lymph itself, the lymphatic system possesses a huge capacity for tumour metastasis. Many types of malignant tumours, such as melanoma and breast and prostate cancers, are prone to metastasize to the regional LNs through the tumour-associated lymphatic vessels.²¹ Consequently, the LN nearest to where cancer cells are spread to from a primary tumour is called the SLN. Currently, the typical procedure for SLN diagnosis is biopsy (SLNB)²² with subsequent pathological analysis, which is based on immunohistochemical staining with cytokeratin 19 (CK19).²³ Although SLNB is less burdensome for patients than axillary lymph node dissection, it still possesses all the drawbacks associated with any surgery.²⁴⁻²⁷ Nevertheless, the clinical advantage of SLNB over node dissection is unquestionable, and the procedure has become the favoured choice for patients with breast cancer, melanoma, and colorectal and prostate cancers.^{28,29} A few studies using magnetic resonance imaging (MRI) for cancer diagnosis and LN visualization were reported,^{30,31} showing a considerable potential of the method. However, this technique remains an additional diagnostic tool rather than a primary one, and deeper research in the field is justified. Additionally, a few other works have promoted SLNs investigation using combined methods, for instance, with the single-photon emission computed tomography (SPECT)/MRI³² and positron emission tomography (PET)/near infrared fluorescence (NIRF)³³ techniques. The available methods and materials

^a Institute of Macromolecular Chemistry, Academy of Sciences of the Czech Republic, Prague, Czech Republic. E-mail: mhruby@centrum.cz

^b Institute for Clinical and Experimental Medicine, Czech Republic

† Electronic supplementary information (ESI) available. See DOI: 10.1039/c7tb02888a



Scheme 1 Chemical structure of native mannan from *Saccharomyces cerevisiae*.

used for these purposes were nicely and thoroughly reviewed elsewhere.^{34,35} Undoubtedly, the development of new prospective methodology and materials for use in SLN diagnostics is currently essential.

The useful biological properties of mannan (MN) inspired us to use it as a platform for preparing new multimodal probes. For this work, commercially available MN from *Saccharomyces cerevisiae* was selected, which consists of an α -1,6-linked mannose backbone with a high percentage of α -1,2 and α -1,3 side chains of different compositions³⁶ (Scheme 1). MN is biocompatible, biodegradable, and nontoxic, and due to the presence of numerous hydroxyl groups in its structure, it can easily be modified to achieve the desired properties. These characteristics all make MN a promising candidate for the development of new polysaccharide-based nanocarriers for biomedical applications.

In a living organism, MN binds to the mannose receptors, which are a class of multilectin receptor proteins that provide a link between innate and adaptive immunity.³⁷ Consequently, MN is preferably accumulated in immune cells³⁸ overexpressing the DC-SIGN receptors (dendritic cell-specific ICAM-grabbing non-integrin receptors, where ICAM is intracellular adhesion molecule), which could be useful for detecting SLNs and inflammations, which are heavily infiltrated with macrophages and DCs. This raises the possibility of using MN as a probe for investigating pathological processes and developing corresponding therapies.

In the past few decades, numerous works have contributed to the synthesis and characterization of poly(2-alkyl-2-oxazoline)s as perspective materials for biomedical applications.^{39–42} The reason for such high interest lies in the biocompatibility and non-toxicity of these bio-inspired polymers along with the wide variety of accessible properties, which depend on the structure and can be easily tailored during synthesis or by a post-modification procedure. Thus, the aim of this study was preparing new hybrid polymer contrast agents based on MN intended for detecting of SLNs by multimodal imaging. We designed and critically compared two new MN-based conjugates: one based only on polysaccharide and the other one comprising polysaccharide with poly(2-methyl-2-oxazoline) (POX) grafts. Both conjugates contained a gadolinium complex and a fluorescent probe for the magnetic resonance imaging (MRI) and optical

fluorescence imaging (FLI) modalities, respectively. These conjugates were simultaneously visualized *in vitro* and *in vivo* by MRI and FLI; moreover, the accumulation of the conjugates in LNs was also shown. Grafting with POX was performed to slow down biodegradation and therefore prolong the diagnostic window for imaging. Both MN-based contrast agents were compared with clinically used gadoterate meglumine (GM) in an *in vitro/in vivo* animal model, showing the striking potential of our probes for LN detection.

Experimental part

Materials

Mannan (MN) from *Saccharomyces cerevisiae*, 2-methyl-2-oxazoline and gadolinium(m) chloride (anhydrous) were purchased from Sigma-Aldrich Ltd (Prague, Czech Republic). Diethyl ether, dimethyl sulfoxide (DMSO), sodium chloride and toluene were purchased from Lachner Ltd (Neratovice, Czech Republic). 1,4,7,10-Tetraazacyclododecane-1,4,7,10-tetraacetic acid *N*-hydroxy-succinimide ester (DOTA-NHS-ester) was purchased from Macrocyclics, Inc. (Plano, USA). IR800CW-NHS-ester was purchased from LI-COR Biotechnology – GmbH (Bad Homburg, Germany). 2,4,6-Trinitrobenzene-1-sulfonic acid (TNBSA) solution was purchased from Thermo Fisher Scientific (Prague, Czech Republic). Ultrapure Q-water ultrafiltered with a Milli-Q Gradient A10 system (Millipore, Molsheim, France) was used throughout the work. Spectra/Por dialysis membranes (molecular weight cut-offs (MWCOs) of 3.5×10^3 and $6–8 \times 10^3$ g mol⁻¹) were purchased from P-LAB (Prague, Czech Republic). All other chemicals were purchased from Sigma-Aldrich Ltd (Prague, Czech Republic) and were used without further purification unless stated otherwise.

Synthesis and preparation

Preparation of allylated mannan (MN_allyl). MN from *S. cerevisiae* (0.6 g, 3.7 mmol glucose units) and sodium hydroxide (0.296 g, 7.4 mmol) were dissolved in water (22 mL), and the solution was cooled to 0 °C. Allyl bromide (100 μ L, 1.16 mmol) was added, and the mixture was stirred for 10 h at 0 °C and then overnight at room temperature. Acetic acid (0.65 mL, 11.4 mmol) was added to neutralize the residual sodium hydroxide; the resulting solution was dialyzed against water using Spectra/Por 3 membrane tubing with a MWCO of 3500 g mol⁻¹ for 48 h and freeze-dried. Yield: 0.597 g (99%) of allylated mannan (MN_allyl, 12.66 mol%).

¹H-NMR of MN_allyl (300 MHz, D₂O), δ (ppm): 3.5–4.2 (–CH₂–CH–, mannose; CH₂=CH–CH₂–), 4.9–5.3 (–O–CH–O, acetal), 5.95 (CH₂=CH–).

Preparation of mannan-graft-poly(2-methyl-2-oxazoline) with theoretical molecular weight of grafts $M_{n,graft} = 1000$ g mol⁻¹ (synthesis of MN_POX). 2-Methyl-2-oxazoline (1.5 mL, 17.71 mmol) and allyl bromide (0.259 mL, 2.99 mmol) were mixed with 7 mL of anhydrous acetonitrile, and the reaction mixture was stirred overnight at 70 °C under an argon atmosphere. MN from *S. cerevisiae* (1 g, 6.17 mmol of glucose units) was dissolved in 23 mL of anhydrous DMSO and the solution was azeotropically

dried by multiple additions of anhydrous toluene (5 mL) and subsequent evaporation at 70 °C under reduced pressure. Sodium hydride (1.7 g of a 60% dispersion in mineral oil, 42.5 mmol) was added to the MN solution, and the mixture was stirred for 3 h at 70 °C. The poly(2-methyl-2-oxazoline) (POX) polymerization mixture (6.86 g) was added to solution of MN sodium alkoxide in DMSO, and the resulting mixture was stirred overnight at 70 °C. Water (10 mL) was added to the reaction mixture, and the resulting suspension was washed twice with diethyl ether (~50 mL) to remove the mineral oil. Finally, the aqueous layer was dialyzed (MWCO of $6-8 \times 10^3 \text{ g mol}^{-1}$) against water for 72 h and freeze-dried to provide the desired product, mannan-graft-poly(2-methyl-2-oxazoline) (MN_POX, 0.943 g, 94.25% yield). The remaining 0.65 mL of POX solution was mixed with 0.25 mL water and purified on a Sephadex[®] LH-20 column using methanol as the mobile phase and evaporated to obtain only the corresponding polymer grafts terminated with -OH groups.

¹H-NMR of POX grafts (300 MHz, CD₃OD), δ (ppm): 2.04 (-CH₃), 3.5–4.3 (-N-CH₂-CH₂-, CH₂=CH-), 5.85 (CH₂=CH-). Matrix-assisted laser desorption/ionization (MALDI) mass spectrometry of POX grafts: $M_n = 870 \text{ g mol}^{-1}$, $I = 1.14$. ¹H-NMR of MN_POX (300 MHz, D₂O), δ (ppm): 1.99 (-CH₃, POX), 3.5–4.2 (-CH₂-CH-, mannose; -N-CH₂-CH₂-, POX; CH₂=CH-), 4.99–5.24 (-O-CH-O, acetal), 5.9 (CH₂=CH-). Elemental analysis of MN_POX: C 41.83%, H 7.13%, N 3.28%.

Addition of cysteamine to MN_allyl or MN_POX (synthesis of MN_NH₂ or MN_POX_NH₂). The product MN_allyl (0.612 g, 0.489 mmol) or MN_POX (0.834 g, 1.029 mmol), cysteamine (0.616 g, 7.98 mmol or 0.836 g, 10.84 mmol for MN_allyl and MN_POX, respectively) and hydrochloric acid (36%, 649 μL , 7.96 mmol or 886.5 μL , 10.87 mmol for MN_allyl and MN_POX, respectively) were dissolved in 13 mL or 17 mL of distilled water (for MN_allyl and MN_POX, respectively) and cooled to 0 °C. A solution of 2-hydroxy-2-methylpropiophenone in ethanol (0.33 vol%, 490 μL or 667 μL for MN_allyl and MN_POX, respectively) was added, and the reaction mixture was irradiated by a UV lamp (TESLA RVK 6 \times 125 W) for 60 min. Then, a solution of sodium carbonate (10 wt%, 30.75 mL or 41.69 mL for MN_allyl and MN_POX, respectively) was added, and the aqueous layer was washed with diethyl ether (~20 mL), dialyzed (MWCO $3.5 \times 10^3 \text{ g mol}^{-1}$) against water for 48 h and freeze-dried. The resulting products were purified on a Sephadex[®] G-25 column using water as the mobile phase and freeze-dried to afford the products MN_NH₂ and MN_POX_NH₂ (514 mg and 689 mg, respectively). The content of -NH₂ groups was determined by their specific reaction⁴³ with TNBSA, which provided a soluble coloured product that was determined spectrophotometrically (0.236 mmol g⁻¹ and 0.195 mmol g⁻¹ of -NH₂ groups for MN_NH₂ and MN_POX_NH₂, respectively).

¹H-NMR of MN_NH₂ (600 MHz, DMSO), δ (ppm): 2.64 (-S-CH₂-CH₂-NH₂), 2.8 (-S-CH₂-CH₂-NH₂), 3.4–4.2 (-CH₂-CH-, mannose; CH₂=CH-), 4.9–5.2 (-O-CH-O, acetal), 5.92 (CH₂=CH-). Elemental analysis of MN_NH₂: C 40.52, 20%, H 6.67%, N 0.69%, S 0.89%. ¹H-NMR of MN_POX_NH₂ (600 MHz, DMSO), δ (ppm): 1.95 (-CH₃, POX), 2.66 (-S-CH₂-CH₂-NH₂),

2.8 (-S-CH₂-CH₂-NH₂), 3.3–4.3 (-CH₂-CH-, mannose; -N-CH₂-CH₂-, POX), 4.97–5.22 (-O-CH-O, acetal). Elemental analysis of MN_POX_NH₂: C 53.20%, H 8.35%, N 5.2%, S 1.83%.

Conjugation of IR800CW-NHS-ester and DOTA-NHS-ester with the primary amino groups contained in MN_NH₂ or MN_POX_NH₂ (synthesis of MN_IR_DOTA or MN_POX_IR_DOTA). MN_NH₂ or MN_POX_NH₂ (454.8 mg, 0.107 mmol of -NH₂ groups or 629.5 mg, 0.123 mmol of -NH₂ groups, respectively), Na₂HPO₄ 12H₂O (4.674 g, 13.05 mmol or 6.541 g, 18.26 mmol for MN_NH₂ and MN_POX_NH₂, respectively) and KH₂PO₄ (293.5 mg, 2.16 mmol or 413 mg, 3.035 mmol for MN_NH₂ and MN_POX_NH₂, respectively) were dissolved in 32 mL or 42 mL of water (for MN_NH₂ and MN_POX_NH₂, respectively) and cooled down to 0 °C. A weighted amount of IR800CW-NHS-ester was added (1.8 mg, 0.001545 mmol or 2 mg, 0.00172 mmol for MN_NH₂ and MN_POX_NH₂, respectively). The reaction mixtures were stirred for 3 h at room temperature. DOTA-NHS-ester (75 mg, 0.0985 mmol or 150 mg, 0.1969 mmol for MN_NH₂ and MN_POX_NH₂, respectively) was added, and the reaction mixtures were stirred overnight at room temperature. The crude products were purified on a Sephadex[®] G-25 column using water as the mobile phase and freeze-dried to afford the products MN_IR_DOTA and MN_POX_IR_DOTA (437 mg and 629.5 mg, respectively).

¹H-NMR of MN_IR_DOTA (600 MHz, DMSO), δ (ppm): 2.51 (-S-CH₂-CH₂-NH₂), 2.65 (-S-CH₂-CH₂-NH₂), 3.4–4.2 (-CH₂-CH-, mannose), 4.7–5.2 (-O-CH-O, acetal). ¹H-NMR of MN_POX_IR_DOTA (600 MHz, DMSO), δ (ppm): 1.15 (-CH₃, POX), 2.58 (-S-CH₂-CH₂-NH₂), 2.7 (-S-CH₂-CH₂-NH₂), 3.4–4.2 (-CH₂-CH-, mannose; -N-CH₂-CH₂-, POX), 4.95–5.2 (-O-CH-O, acetal).

Finally, MN_IR_DOTA or MN_POX_IR_DOTA was chelated with Gd(III) according to the following procedure: the MN-based conjugate (402 mg or 620 mg for MN_IR_DOTA and MN_POX_IR_DOTA, respectively), ammonium acetate (1.171 g, 15.19 mmol or 1.868 g, 24.23 mmol for MN_IR_DOTA and MN_POX_IR_DOTA, respectively) and gadolinium(III) chloride (171.5 mg, 0.651 mmol or 270 mg, 1.024 mmol for MN_IR_DOTA and MN_POX_IR_DOTA, respectively) were dissolved in water (30 mL or 50 mL for MN_IR_DOTA and MN_POX_IR_DOTA, respectively), and the reaction mixture was stirred overnight at room temperature. The crude products were twice purified on a Sephadex[®] G-25 column using water as the mobile phase and freeze-dried to provide MN_IR_DOTA-Gd and MN_POX_IR_DOTA-Gd (342 mg and 533 mg, respectively). The content of Gd(III) was determined by energy-dispersive X-ray spectroscopy (EDS) and was found to be 3.94% (0.252 mmol g⁻¹) and 4.22% (0.27 mmol g⁻¹) for MN_IR_DOTA and MN_POX_IR_DOTA-Gd, respectively.

The amount of the IR800CW label was determined spectrophotometrically (0.1 wt%, $\lambda = 774 \text{ nm}$, $\epsilon = 240\,000 \text{ L mol}^{-1} \text{ cm}^{-1}$) and was found to be 0.72 μmol and 0.66 μmol for MN_IR_DOTA and MN_POX_IR_DOTA-Gd, respectively.

Characterization

¹H NMR measurements were conducted on a Bruker Avance DPX-300 spectrometer operating at 300.13 MHz and on a

Bruker Avance III 600 spectrometer operating at 600 MHz (both Bruker Co., Austria). Fourier transform infrared (FT-IR) spectra were obtained on a Perkin-Elmer Paragon 1000PC spectrometer (Perkin-Elmer Co., USA) equipped with a Specac MKII Golden Gate single attenuated total reflection (ATR) system (Perkin-Elmer Co., USA). Elemental analysis was performed on a Perkin-Elmer Series II CHNS/O Analyzer 2400 (PE Systems Ltd, Czech Republic) instrument. UV-Vis absorption spectra of the obtained conjugates were acquired at a 1 mg mL⁻¹ concentration (in phosphate buffered saline, PBS) using a Specord® 250 Plus UV-Vis spectrometer (Jena, Germany) (Fig. S1-1, ESI†). Fluorescence spectra of the samples were recorded (90° angle geometry, 1 × 1 cm quartz cell) at a concentration of 1 mg mL⁻¹ (in PBS) using an FP-6200 spectrofluorometer (Jasco Europe, Italy) with an excitation wavelength of 774 nm (Fig. S1-2, ESI†).

The molecular weight of POX was determined using MALDI. The MALDI-TOF mass spectra were acquired with an Ultraflex (Bruker Daltonics, Bremen, Germany) in positive ion reflection mode using delayed extraction. The spectra were taken as the sum of 30 000 shots with a DPSS Nd:YAG laser (355 nm, 1000 Hz). External calibration was used. The specimens were prepared by the dried droplet method. The sample solution (10 mg mL⁻¹), DHB (2,5-dihydroxybenzoic acid; 20 mg mL⁻¹) used as the matrix and sodium trifluoroacetate (NaCF₃COO; 10 mg mL⁻¹) as a cationization agent in methanol were mixed at a volume ratio of 4 : 20 : 1.1 μL, and the mixture was deposited on the ground-steel target plate. The drop was dried under ambient atmosphere. The molecular weight of the prepared MN-based polymers was determined by SEC; the system contains a Delta-chrom SDS030 pump (Watrex Co., Prague, Czech Republic), a MIDAS autosampler (Spark HOLLAND B.V., Netherlands), a column (STR SEC-100, 5 μm) and a DAWN® HELEOS® multi-angle static light scattering detector (Wyatt Technology Corporation, USA) with acetate buffer used as the mobile phase.

The behaviour of the prepared conjugates in water was studied using dynamic light scattering (DLS) and electrophoretic mobility to determine their hydrodynamic radius (R_{hyd}) and ζ-potential (ZP), respectively. The measurements were conducted on a Zetasizer Nano-ZS, Model ZEN3600 (Malvern Instruments, UK), at a scattering angle $\theta = 173^\circ$ at 25 °C (using DTS software – version 6.20 for data evaluation); data from the volume distribution function were used to determine the hydrodynamic radius R_{hyd} .

Cell viability assay

The cytotoxicity profile of the MN-based conjugates was evaluated using macrophages isolated from the ascites of mice with Abelson murine leukaemia virus-induced tumours (RAW 264.7), macrophages isolated from the ascites of mice with reticulum cell sarcoma (J774A.1), human breast cancer cells from the mammary gland (4T1) and human adenocarcinoma cells from the mammary gland (MCF7) by an Alamar Blue assay. The RAW 264.7 and J774A.1 cell lines were purchased from Merck Ltd (Czech Republic), and the 4T1 and MCF7 cell lines were purchased from LGC Standard Spz.o.o. (Poland). The cells

were seeded in 96-well flat-bottom plates at concentrations of 8×10^3 cells per well for the RAW 264.7 and J774A.1 cell lines and 5×10^3 cells per well for the 4T1 and MCF7 cell lines in 100 μL of cultivation media at 24 h before adding the polymer conjugates. The cells were incubated at 37 °C in 5% CO₂ with 2 different MN-based conjugates over an equivalent concentration range of 0.004–0.5 mg mL⁻¹ for 72 h. Cell viability was measured using Alamar Blue cell viability assay reagent (Thermo Fischer Scientific, Czech Republic). Non-treated cells were used as a viability control (100% viability). The experiment was performed three times in triplicates.

In vitro studies

To characterize the imaging properties of the probes, MN_IR_DOTA-Gd, MN_POX_IR_DOTA-Gd and gadoterate meglumine (GM) were dissolved in distilled water to obtain the same Gd³⁺ concentration (0.36, 0.24, 0.18, 0.12, 0.06, 0.03 mmol L⁻¹) or IR800 dye concentration (1.13, 0.75, 0.56, 0.28, 0.14, 0.07 μg mL⁻¹) for magnetic resonance (MR) and fluorescence (FL) imaging, respectively. The MR properties of the probes were assessed on a 0.5 T Minispec NMR relaxometer (Bruker BioSpin, Germany) by T_1 (saturation recovery sequence, recycle delay of 12 s or 5 s) and T_2 relaxometry (Carr-Purcell–Meiboom–Gill (CPMG) sequence, recycle delay of 10 s, interpulse delay of 1 ms, 5000 points).

MRI was performed on a 4.7 T Bruker Biospec scanner using a resonator coil (Bruker, BioSpin, Germany). T_1 -Weighted images were acquired by a turbo spin echo sequence with the following parameters: repetition time TR = 125 ms, echo time TE = 11 ms, turbo factor TF = 2, spatial resolution = $0.27 \times 0.27 \times 1.5$ mm³, scan time = 6.5 min and fluorescence imaging (10 s of exposure, excitation of 745 nm, and emission of 810–875 nm). Regions of interest (ROIs) were manually outlined around each sample in the MR and FL images, and the signal intensity was assessed. Contrast-to-noise ratio (CNR) values from the MR images were calculated as the difference between the signal intensity from the sample and the water signal intensity (normalized to the water signal). The average FL radiance efficiency was assessed from ROIs covering the samples in the FL images using Living Image software (Perkin-Elmer, USA).

In vivo experiments

The animal experiments described below were performed in the accordance with The Law of Animal Protection against Cruelty (Act No. 359/2012) of the Czech Republic, which is fully compatible with the European Communities Council Directive 86/609/EEC.

For 3 weeks of monitoring *in vivo*, 100 μL of MN_IR_DOTA-Gd or MN_POX_IR_DOTA-Gd (both at concentration of 3.5 mg of Gd³⁺ per mL and 0.64 mg mL⁻¹ of IR800 dye) were administered into the calf muscle of the right hind leg of healthy C57/6J B6 mice ($n = 3$ for each group). MRI was performed on a 4.7 T MR Bruker Biospec scanner (Bruker BioSpin, Germany) using a homemade surface coil. T_1 -Weighted axial and coronal MR images of the calf muscles and LNs of mice were acquired using a turbo spin echo sequence with the following parameters: TR = 339 ms, TE = 12 ms, TF = 2, spatial resolution

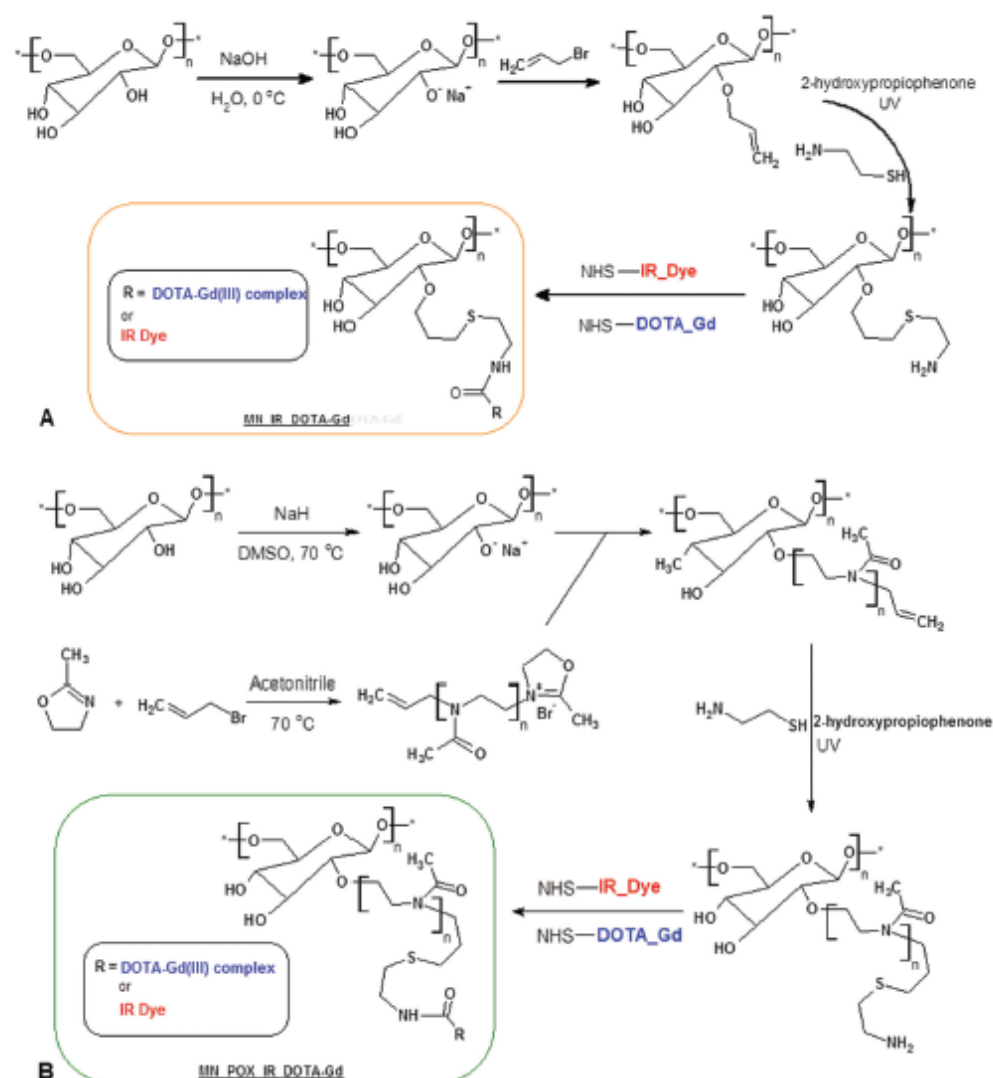
was $0.16 \times 0.16 \times 0.70$ mm, 9 slices and scan time = 8 min 40 s. *In vivo* FL images were acquired within a 60 s exposure time using an excitation wavelength at 745 nm and an emission wavelength at 810–875 nm. MRI was performed immediately after agent injection and then at 6 h and 1, 2, 3, 4, 7, 14 and 21 days after contrast agent administration. FLI was conducted at the same time points as MRI and before and 2 h after agent administration. One animal per group was sacrificed at days 7, 14 and 21, and its internal organs were excised and subjected to *ex vivo* FLI.

CNR values of the inguinal LNs were calculated in percentage from the MR images as the difference between the signal intensities of the LN and the surrounding fat (normalized to the fat signal) to suppress inhomogeneity originating from the

surface coil. FL was evaluated from *in vivo* images of the liver and the lymph nodes and from *ex vivo* images of excised organs (spleen, liver, kidney, and inguinal LNs).

Results and discussion

The natural biodegradable polysaccharide MN was modified in two different ways to obtain conjugates bearing a fluorescent label and a probe for MRI. The first approach was focused on the synthesis of a polysaccharide-based conjugate without polyoxazoline in the structure (Scheme 2A). The modification procedure began with the alkylation of commercial MN (from *S. cerevisiae*) with allyl bromide in alkaline aqueous solution to



Scheme 2 Synthetic route for mannan modification: preparation of MN_IR_DOTA-Gd (A) and MN_POX_IR_DOTA-Gd (B).

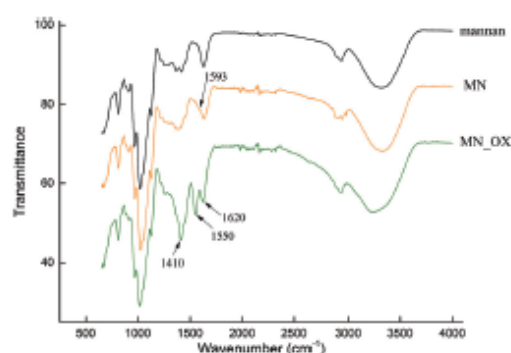


Fig. 1 FTIR spectra of native mannan (black line), MN_IR_DOTA-Gd (orange line) and MN_POX_IR_DOTA-Gd (dark green line).

obtain the vinyl-containing derivative of MN (MN_allyl, 12.66 mol% of allyl). This derivative was later reacted with cysteamine using 2-hydroxy-2-methylpropiophenone as initiator under UV irradiation. This primary amino group-containing MN was then conjugated with *N*-hydroxysuccinimide (NHS) esters of an infrared dye (IR800CW NHS-ester) and 1,4,7,10-tetraazacyclododecane-1,4,7,10-tetraacetic acid (DOTA NHS-ester). Finally, the obtained product was reacted with gadolinium(III) chloride to chelate Gd^{3+} , resulting in an MN-based conjugate with FL and MR imaging labels, denoted MN_IR_DOTA-Gd.

Grafting with a synthetic polymer decreases the biodegradation rate^{44,45} of the polysaccharide and introduces the possibility of easy functionalization of the ends of the polymer grafts with active cargo. The synthetic approach for the preparation of MN-based conjugate with grafted polyoxazoline chains was slightly different from that for MN_IR_DOTA-Gd (Scheme 2B). After dissolution in anhydrous DMSO, MN sodium alkoxide was reacted with active POX chains obtained by ring-opening cationic polymerization in anhydrous acetonitrile. Different MN grafting

Table 1 Characteristics of native and modified mannan

Name	$M_w \times 10^{-3}$, ^b g mol ⁻¹	R_{hyd} , ^c nm		ZP, ^c mV	
		H ₂ O	PBS	H ₂ O	PBS
Mannan ^a	44.6	1.2	3.6	0.2	-5.6
MN_IR_DOTA-Gd	52	3.1	3.3	-4.0	-11.5
MN_POX_IR_DOTA-Gd	71.2	3.0	3.6	2.9	-6.7

^a Commercial (native) mannan from *Saccharomyces cerevisiae*. ^b Determined by mass spectrometry. ^c Obtained from dynamic light scattering and electrophoretic mobility measurements.

reactions with POX were performed (data not shown) to determine the maximal achievable grafting density, which was found to be 30 mol%. Consequently, mannan-graft-poly(2-methyl-2-oxazoline) (denoted MN_POX) with a grafting density of 1 graft per 5 glucose units (29.73 mol% of POX from ¹H NMR) was selected for this work. The molecular weight of POX grafts was determined by mass spectrometry after termination of active chains with water: number-average molecular weight $M_n = 870$ g mol⁻¹, polydispersity PDI = $M_w/M_n = 1.14$, where M_w is the weight-average molecular weight.

Because the starting MN from *S. cerevisiae* contained less than 0.3 wt% nitrogen, the weight content of POX in the prepared polymers could be calculated from elemental analysis (CHN) according to the following equation:

$$w_{pMeOx} = \frac{w_N}{w_{N,pMeOx}} \times 100\%$$

where w_N is the content of nitrogen in the sample (determined by CHN elemental analysis) and $w_{N,pMeOx}$ is the calculated content of nitrogen in the POX graft (16.45% in our case). The POX content for MN_POX was found to be 19.94 wt%.

Next, allyl-containing mannan derivatives were modified by radically initiated thiol-ene click chemistry with cysteamine to obtain conjugates with primary amino groups (Scheme 2B). These primary amino groups then can be easily modified with

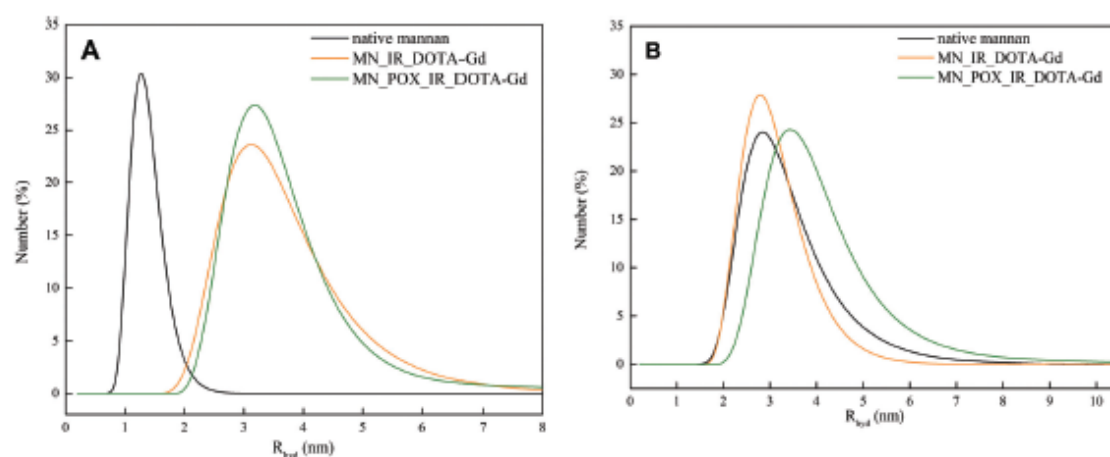


Fig. 2 Dynamic light scattering results of native mannan from *Saccharomyces cerevisiae* and of the mannan-based conjugates in water (A) and PBS (pH = 7.4) (B) at a concentration of 1 mg mL⁻¹.

fluorescence- and/or MRI-active labels. For this purpose, the amino-functionalized polysaccharides were reacted with the NHS ester of IR800CW dye as infrared (IR) active fluorescence label and the NHS ester of an MRI T_1 contrast agent – Gd^{3+} -DOTA (Scheme 2B).

Both of the resulting mannan-based conjugates – those without and with POX chains in the structure, MN_IR_DOTA-Gd and MN_POX_IR_DOTA-Gd, respectively – were twice purified on a Sephadex G-25[®] column using water as the eluent, and then their aqueous solutions were lyophilized. The content of IR dye was determined spectrophotometrically in water ($\lambda = 774$ nm, $\epsilon = 240\,000$ M⁻¹ cm⁻¹) and was found to be 0.72 and 0.66 $\mu\text{mol g}^{-1}$ in the MN_IR_DOTA-Gd and MN_POX_IR_DOTA-Gd conjugates, respectively. The content of gadolinium in the final products was determined by inductively coupled plasma mass spectrometry and was found to be 0.252 and 0.26 mmol g⁻¹ for MN_IR_DOTA-Gd and MN_POX_IR_DOTA-Gd, respectively. The obtained concentrations

of Gd^{3+} in the prepared mannan probes correspond to 13 and 19 gadolinium atoms per molecule of MN_IR_DOTA-Gd and MN_POX_IR_DOTA-Gd, respectively.

Fourier transform infrared (FTIR) spectroscopy was used to prove the bonding of the IR and DOTA labels to both MN derivatives. The IR spectrum of neat MN shows peaks at 3320, 2934, 1635 and 1022 cm⁻¹, which correspond to $\nu(\text{OH})$, $\nu_{\text{as}}(\text{CH}_2)$, $\nu(\text{CO})$ and $\nu(\text{COC})$ vibrations, respectively (Fig. 1). Because the MN used was extracted from baker's yeast, we attribute the appearance of carbonyl groups in the spectrum to the presence of a small amount of peptide residues in its structure. The FTIR spectrum of MN_IR_DOTA-Gd exhibits the appearance of a weak $\delta(\text{NH})$ deformation vibration peak located at 1593 cm⁻¹, confirming the successful bonding of the IR and DOTA labels through amide groups. For the MN_POX_IR_DOTA-Gd conjugate, this peak is probably overlapped by strong $\nu(\text{CO})$ vibrations at 1620 and 1550 cm⁻¹ originating from the grafted POX chains.

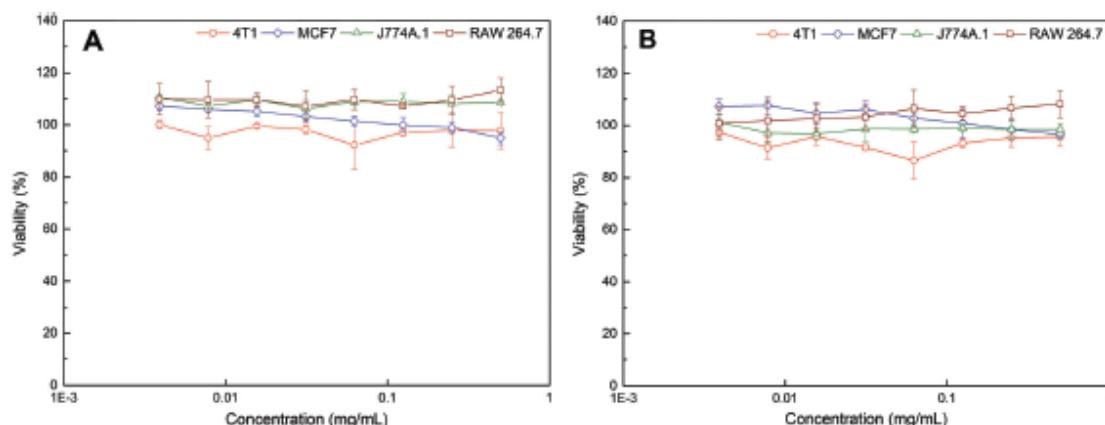


Fig. 3 Viability of MN_IR_DOTA-Gd (A) and MN_POX_IR_DOTA-Gd (B) in macrophage (RAW 264.7 and J774A.1) and mammary gland (4T1 and MCF7) cell lines as a function of conjugate concentration (0.004–0.5 mg mL⁻¹) after 72 h of incubation at 37 °C in 5% CO₂. Treated cells were compared to controls (without addition of MN-based conjugates) to obtain percent viability.

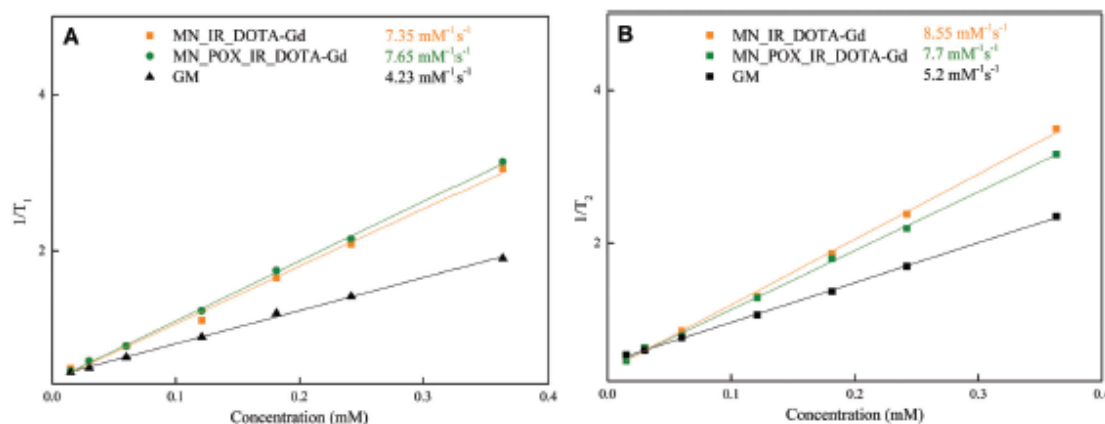


Fig. 4 Characterization of the probes – ¹H r_1 (A) and r_2 (B) relaxivities of the tested probes measured at 0.5 T (25 °C).

Another confirmation of the successful grafting of MN with the POX chains is the appearance of a strong $\nu(\text{C}=\text{C})$ vibration at 1410 cm^{-1} of the vinyl end group of POX.

To characterize the behaviour of the prepared conjugates in aqueous solution, dynamic light scattering (DLS) measurements were conducted using a Zetasizer Nano-ZS (Malvern)

instrument. To determine the difference in hydrodynamic diameter due to the modification procedure, native MN from *S. cerevisiae* and both of the prepared conjugates were dissolved in Q-water or phosphate buffered saline (PBS) at a concentration of 1 mg mL^{-1} , and DLS measurements were performed (Fig. 2).

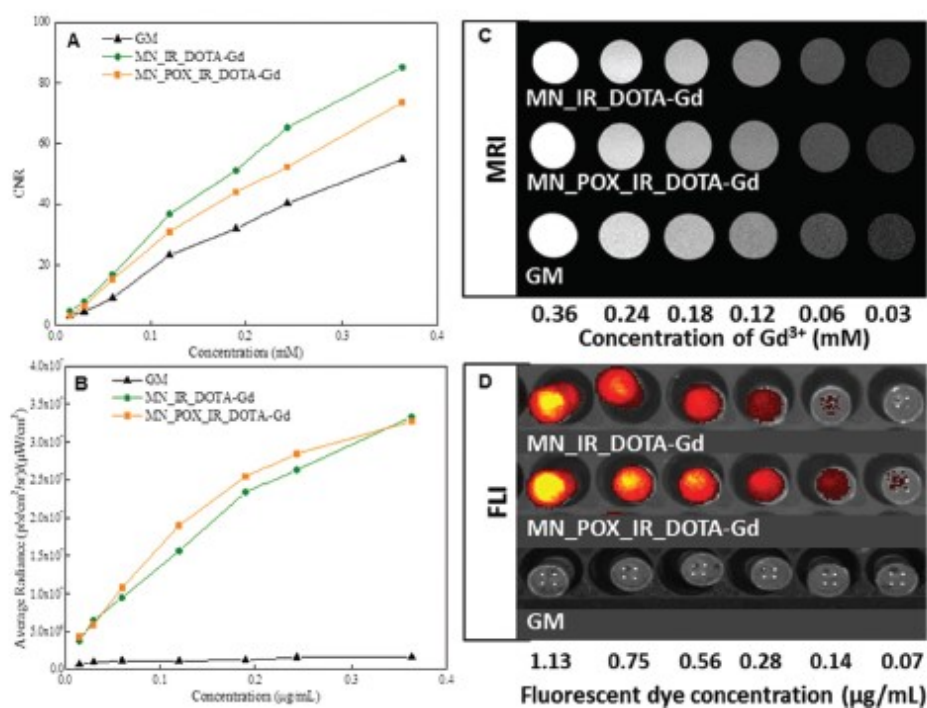


Fig. 5 The magnetic resonance (MR) and fluorescence (FLI) signals of the MN_IR_DOTA-Gd, MN_POX_IR_DOTA-Gd and gadoterate meglumine (GM). Contrast-to-noise ratio (CNR) was calculated from the MR images (A) and FLI signal (B) of the probes at various concentration of Gd^{3+} or fluorescent dye. Representative MR images of the probes with different Gd^{3+} concentrations (C) – the numbers represent Gd^{3+} concentration expressed in mM; the FLI images of the probes with different dye concentrations (D); the numbers represent the concentration of fluorescent dye expressed in $\mu\text{g mL}^{-1}$.

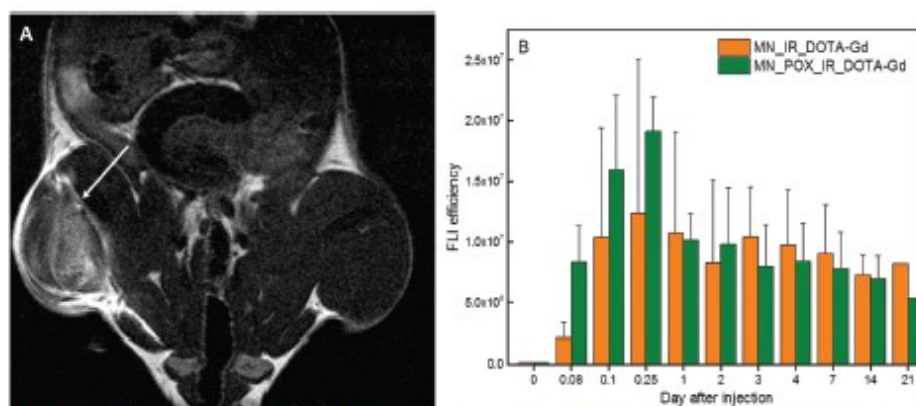


Fig. 6 Representative T_1 -weighted magnetic resonance (MR) image of a mouse injected in its hind leg with the MN_IR_DOTA-Gd probe (A); the arrow denotes the injection site. The time course of the fluorescence (FLI) signal from the injection site (muscle) (B).

Fig. 2 presents the size distributions of the neat and modified MN in water and in PBS. Because of the modification procedure described above, the hydrodynamic radius of MN was found to increase. In aqueous solution, the R_{hyd} of both MN_IR_DOTA-Gd and MN_POX_IR_DOTA-Gd were *ca.* two times larger (~ 3 nm) than native MN (1.2 nm). In comparison to that of native MN, the ζ -potential (ZP) of MN_IR_DOTA-Gd decreased to -4 mV (Table 1), confirming the presence of ionic carboxylate groups from the FLI and MRI contrast labels. In the case of MN_POX_IR_DOTA-Gd, the ZP had increased to 2.9 mV, indicating the presence of grafted POX chains in its structure. When PBS was used as solvent (pH = 7.4), no significant difference in hydrodynamic radius could be observed between native MN and the modified MN derivatives ($R_{hyd} \sim 3.5$ nm). In contrast to aqueous solution, the ZP values in PBS (pH = 7.4) of all three samples were small and negative, probably due to formation of a counter ion layer (Table 1). Moreover, the DLS measurements performed in water at different pH ranging from 5 to 9 did not show a significant change in hydrodynamic radius of either of the prepared MN-based probes (R_{hyd} from 2 to 4 nm). Those results show that the behaviour of the prepared conjugates is insensitive to different pH or increased ionic strength, which is beneficial for the intended application.

To study the biocompatibility of the synthesized MN-based conjugates, *in vitro* testing with four different cell lines was conducted. As shown in Fig. 3, no significant changes in the viabilities of any of the treated cells were observed after incubation with the prepared conjugates. The viability varied within the experimental error between 85 and 110% of the

control (non-treated cells). There were no concentration-dependent changes in the cytotoxicity of the conjugates. The obtained results prove the potential of the new MN derivatives for use in biomedical applications, for instance as a drug delivery system targeted to immune and metastatic cells or as a diagnostic probe with enhanced tumour accumulation and specific targeting for LNs.

To demonstrate the imaging performance of the prepared conjugates, an *in vitro* experiment on phantoms was performed first. Both MN-based agents showed higher r_1 and r_2 relaxivities than commercially available GM (Fig. 4A and B) based on Gd^{3+} concentration, probably due to the decreased mobility of the chelated gadolinium arising from the conjugation to relatively high-molecular-weight polymers. On the other hand, the relaxivities of MN_IR_DOTA-Gd and MN_POX_IR_DOTA-Gd were comparable. Similarly, the MR signals and corresponding contrast-to-noise ratio (CNR) values of the MN-based probes were higher than those of GM (Fig. 5A and C).

The MN-based agents also showed a strong FL signal, whereas the FL of GM was in the range of the background as expected (Fig. 5B and D). Therefore, these promising *in vitro* results encouraged us to perform pilot *in vivo* experiments on healthy mice. GM is not fluorescent and is not an actively LN-targeted probe; thus, only MN-based contrast agents are discussed hereinafter for the *in vivo* experiments.

After intramuscular administration to the mice, both the MN_IR_DOTA-Gd and MN_POX_IR_DOTA-Gd agents were visualized at the injection sites by MRI and FLI for 21 days. The 21-day imaging was performed to monitor the *in vivo* fate

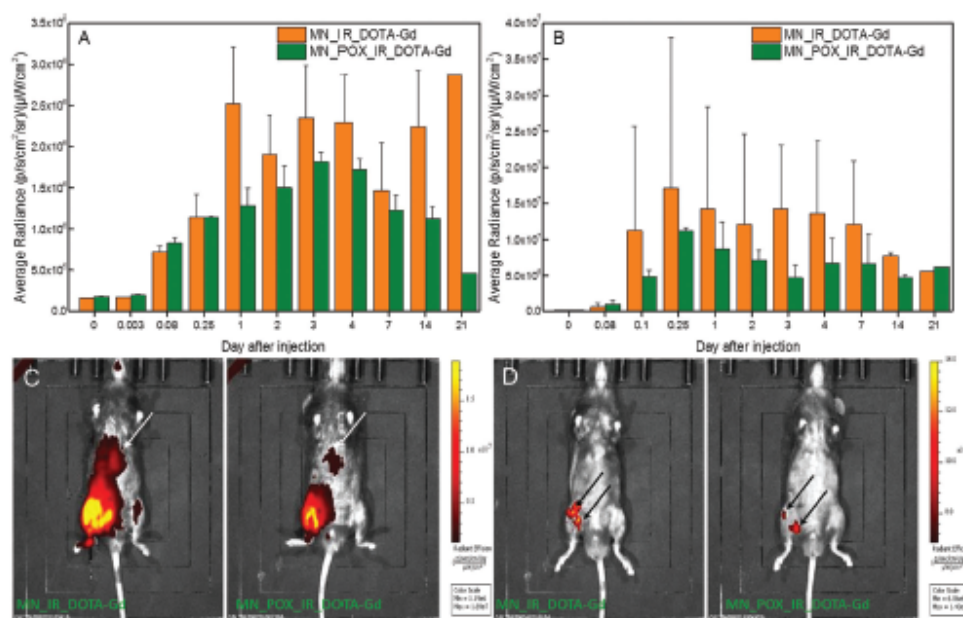


Fig. 7 Time course of the *in vivo* fluorescence (FL) signal originating from the liver (A) and the lymph nodes (B). Representative fluorescence images of mice after injection with MN_IR_DOTA-Gd and MN_POX_IR_DOTA-Gd (C and D). The arrows denote the liver (C) and the lymph nodes (D).

and biodegradability of the conjugates and to find the optimal time for the highest contrast against the surrounding tissues. The FL signal increased within the first day and then continuously decreased until the end of the examination. The most plausible explanation for this effect is that immediately after administration, the contrast agent is concentrated within a small volume, and because of the high concentration, it self-quenches. Over time, the contrast agent spreads to a larger volume (and the emitting area exposed to the detector is therefore larger). Thus, the quenching effect is no longer as prominent, and as a result, paradoxically, more photons capable of penetrating through the skin, are detected. Fig. 6B shows that the fluorescence signal of MN_POX_IR_DOTA-Gd in muscle was higher than that of MN_IR_DOTA-Gd within the first two days after injection, demonstrating that POX grafting prolonged the imaging window and that biodegradation of the conjugate was slower.

Moreover, the FL signal was visualized in the liver site after injecting the probes. After 1 day, the FL signal originating from MN_IR_DOTA-Gd was higher than that originating from MN_POX_IR_DOTA-Gd, and this trend persisted to the end of the examination time (Fig. 7A and C). Within the first day after probe administration, higher FL and MR signals from the

LN were detected in case of MN_IR_DOTA-Gd, confirming its faster degradation (Fig. 7B, D and 8).

MRI confirmed the presence of the injected probes at the muscle sites (Fig. 6A) and in the LNs of both mice (*i.e.*, those treated with MN_IR_DOTA-Gd and MN_POX_IR_DOTA-Gd) (Fig. 8B). Within the first day after probe administration, the MR signal of MN_IR_DOTA-Gd was higher than that of MN_POX_IR_DOTA-Gd, which in agreement with the results obtained from FLI. As seen in Fig. 6B and 7B, which present the time courses of the FL signal originating from injected site and LNs, respectively, the signals were similar, with an average value of 1.5×10^7 . The MR signal in the non-injected muscle (*i.e.*, background; see Fig. 6A) was much lower, which is important for the intended use, and the evaluated MR signal data from the LNs (Fig. 8A) clearly show the stable presence of the contrast agents.

In addition, *ex vivo* FLI of the harvested organs also confirmed the lower accumulation of MN_POX_IR_DOTA-Gd in the liver, spleen and kidneys for all time intervals (7, 14, and 21 days) (Fig. 9). The signals originating from the LNs were comparable for both the MN_IR_DOTA-Gd and MN_POX_IR_DOTA-Gd conjugates within 7, 14 and 21 days after probe administration (Fig. 9J–L). Although the FL signal

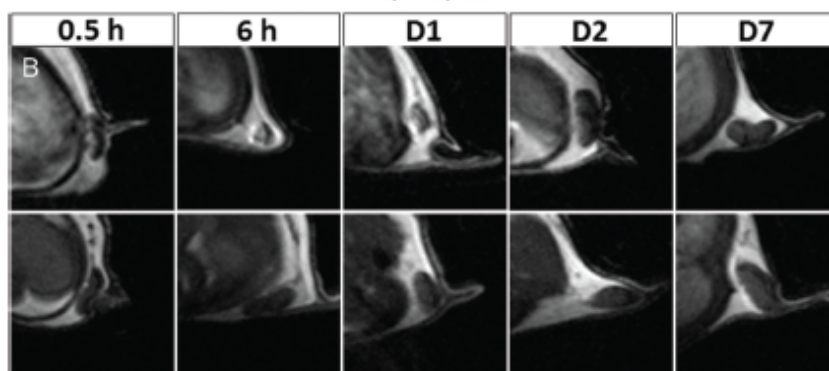
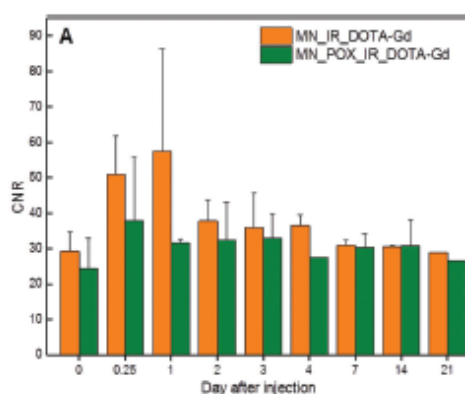


Fig. 8 Time course of the magnetic resonance (MR) signal in the lymph nodes of mice after injection with MN_IR_DOTA-Gd or MN_POX_IR_DOTA-Gd (A). Representative T_1 -weighted MR images show the lymph nodes at different time points (B) after MN_IR_DOTA-Gd (top) or MN_POX_IR_DOTA-Gd (bottom) administration.

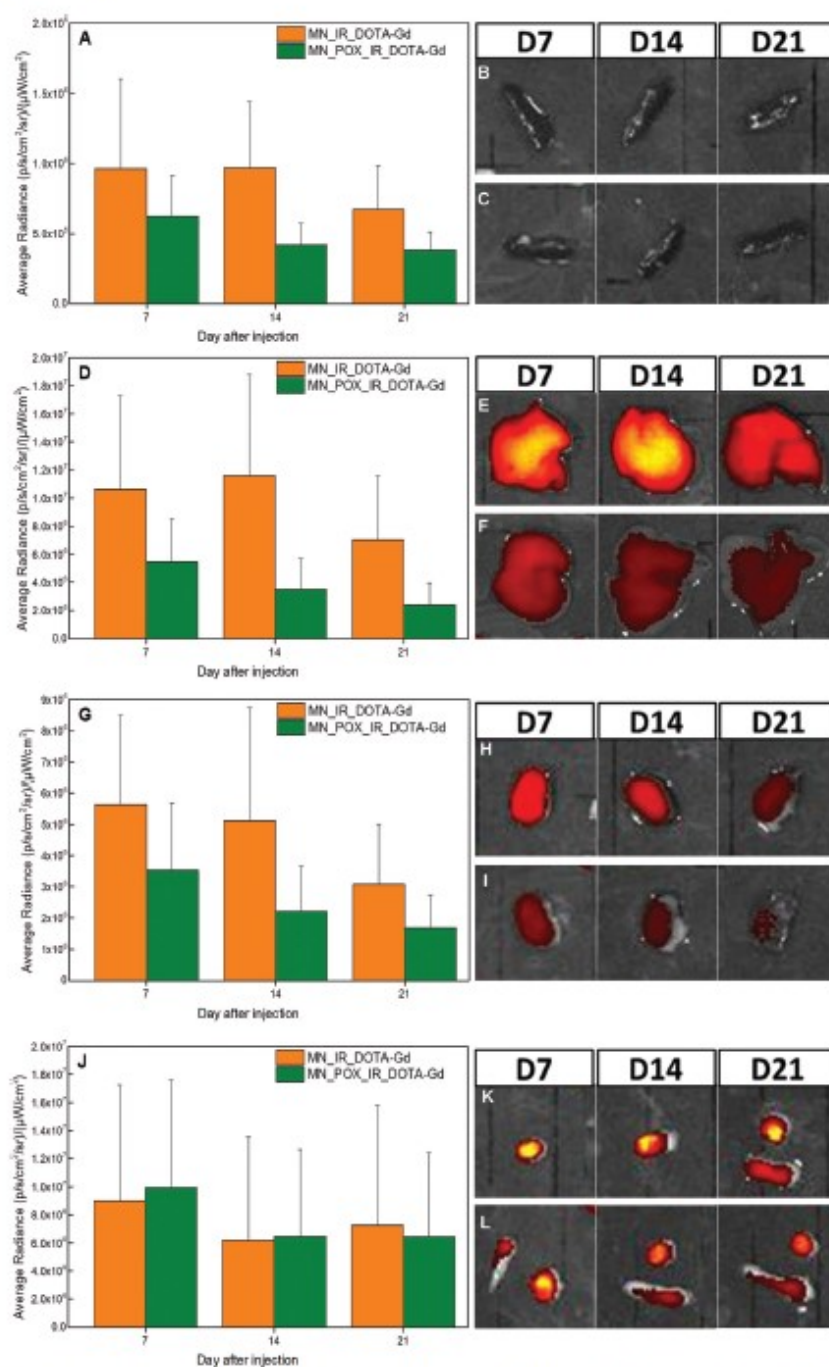


Fig. 9 Average radiant efficiency in the spleen (A), liver (D), kidney (G) and lymph nodes (J) *ex vivo*. Fluorescence (FL) signal after 7, 14 and 21 days from the spleen (B and C), liver (E and F), kidney (H and I) and lymph nodes (K and L) after administration of MN_IR_DOTA-Gd (B, E, H and K) or MN_POX_IR_DOTA-Gd (C, F, I and L).

from the LNs remained very similar throughout whole examination time, the signal from organs (liver, spleen, kidneys)

continuously decreased over time for both conjugates, indicating the gradual biodegradation of the MN probes.

Therefore, the novel MN-based compounds possess superior properties compared to the commercially available contrast agent GM, including their MR relaxivity and FLI capability. The visualized accumulation of the agents in the LNs confirmed their immune system-targeted properties and possible use in metastasis diagnostics.

Conclusions

We demonstrated an easy synthetic approach for preparing novel multimodal MN-based probes intended for immune cell detection. The obtained conjugates contained both a fluorescent IR dye and a Gd³⁺ MRI contrast agent in their structures. The content of the FL label was estimated spectrophotometrically and was found to be 0.72 and 0.66 $\mu\text{mol g}^{-1}$ for MN_IR_DOTA-Gd and MN_POX_IR_DOTA-Gd, respectively. The chelation efficiency of DOTA with Gd³⁺ was analysed by inductively coupled plasma mass spectrometry, and the concentration of Gd³⁺ in MN_IR_DOTA-Gd and MN_POX_IR_DOTA-Gd was 0.252 and 0.26 mmol g^{-1} , respectively. The prepared probes possessed sufficient sensitivity for *in vivo* FLI and exhibited superior MRI properties compared to a commercial contrast agent. The MN-based conjugates were detected in organs 3 weeks after probe administration, indicating their slow biodegradation; however, the strongest MRI and FLI signals were detected within the first day following agent administration. Moreover, the appearance of a lower FL signal at the liver and higher FL signal at the administrated site in the mouse injected with MN_POX_IR_DOTA-Gd suggested its slower elimination process due to the addition of POX chains in its structure. The possibility of further chemical modification of the obtained MN-based conjugates for incorporating specific drugs, for obtaining structures with a suitable size for enhanced accumulation in tumours and for achieving specific targeting of LNs makes these agents promising as a drug delivery system targeted to immune and metastasis cells.

Conflicts of interest

There are no conflicts to declare.

Acknowledgements

The authors acknowledge financial support from the Ministry of Health of the Czech Republic (grant # 15-25781a). The authors also acknowledge the Charles University in Prague for the opportunity for doctoral studies provided to M. Rabyk.

References

- 1 A. Basu, K. R. Kunduru, E. Abtey and A. J. Domb, *Bioconjugate Chem.*, 2015, **26**, 1396.
- 2 E. Muntimadugu, D. E. Ickowicz, A. J. Domb and W. Khan, *Isr. J. Chem.*, 2013, **53**, 787.
- 3 S. N. Lakshmi and C. T. Laurencin, *Prog. Polym. Sci.*, 2007, **32**, 762.

- 4 K. M. Colvin, V. D. Gordon, K. Murakami, B. R. Borlee, D. J. Wozniak, G. C. L. Wong and M. R. Parsek, *PLoS Pathog.*, 2011, **7**(1), e1001264.
- 5 Z. Liu, Y. Jiao, Y. Wang, C. Zhou and Z. Zhang, *Adv. Drug Delivery Rev.*, 2008, **60**, 1650.
- 6 Y. Zhang, H. F. Chan and K. W. Leong, *Adv. Drug Delivery Rev.*, 2013, **65**, 104.
- 7 N. B. Shelke, R. James, C. T. Laurencin and S. G. Kumbar, *Polym. Adv. Technol.*, 2014, **25**, 448.
- 8 C. Goncalves, S. A. Ferreira, A. L. Correia, C. Lopes, C. E. Fleming, E. Rocha, M. Vilanova and M. Gama, *J. Bioact. Compat. Polym.*, 2016, **31**, 453.
- 9 T. Azzam, H. Elyahu, L. Shapira, M. Linial, Y. Barenholz and A. J. Domb, *J. Med. Chem.*, 2002, **45**, 1817.
- 10 T. Kutlusoy, B. Oktay, N. K. Apohan, M. Suleymanoglu and S. C. Kuruca, *Int. J. Biol. Macromol.*, 2017, **103**, 366.
- 11 M. Lepore, M. Portaccio, I. Delfino, L. Sironi, A. La Gatta, A. D'Agostino, E. Izzo and C. Schiraldi, *J. Appl. Polym. Sci.*, 2017, **134**, 45243.
- 12 S. Naahidi, M. Jafari, M. Logan, Y. Wang, Y. Yuan, H. Bae, B. Dixon and P. Chen, *Biotechnol. Adv.*, 2017, **5**, 530.
- 13 N. P. Birch and J. D. Schiffman, *Langmuir*, 2014, **30**, 3441.
- 14 N. Goodarzi, R. Varshochian, G. Kamalinia, F. Atyabi and R. Dinarvand, *Carbohydr. Polym.*, 2013, **92**, 1280.
- 15 A. Shimoda, S. Sawada, A. Kano, A. Maruyama, A. Moquin, F. M. Winnik and K. Akiyoshi, *Colloids Surf., B*, 2012, **99**, 38.
- 16 Y. Yu, H. Zhang, H. Sun, D. Xing and F. Yao, *Front. Chem. Sci. Eng.*, 2013, **7**, 388.
- 17 Z. Odabasi, G. Mattiuzzi, E. Estey, H. Kantarjian, F. Saeki, R. J. Ridge, P. A. Ketchum, M. A. Finkelman, R. H. Rex and L. Ostrosky-Zeichner, *Clin. Infect. Dis.*, 2004, **2**, 199.
- 18 S. Pan, T. A. Brentnall and R. Chen, *World J. Gastroenterol.*, 2016, **22**, 9288.
- 19 S. B. Majee, D. Avlani and G. R. Biswas, *Afr. J. Pharm. Pharmacol.*, 2017, **11**, 68.
- 20 A. Martín-Fontecha, A. Lanzavecchia and F. Sallusto, in *Handbook of Experimental Pharmacology*, ed. G. Lombardi and Y. Riffó-Vasquez, Springer-Verlag, Berlin, 2009, vol. 188, pp. 31–49.
- 21 S. Karaman and M. Detmar, *J. Clin. Invest.*, 2014, **124**, 922.
- 22 G. H. Lyman, S. Temin, S. B. Edge, L. A. Newman, R. R. Turner, D. L. Weaver, A. B. Benson, L. D. Bosserman, H. J. Burstein, H. Cody, J. Hajman, C. L. Perkins, D. A. Podoloff and A. E. Giuliano, *J. Clin. Oncol.*, 2014, **13**, 1365.
- 23 P. Szycha, B. Westfal, R. Maciejczyk, B. Smolarz, H. Romanowicz, T. Krawczyk and M. Zadrozny, *Arch. Med. Sci.*, 2014, **12**, 1239.
- 24 S. M. Ha, J. H. Cha, H. H. Kim, H. J. Shin, E. Y. Chae and W. J. Choi, *Acta Radiol.*, 2017, **10**, 1198.
- 25 J. P. Hoogendam, R. P. Zweemer, M. G. G. Hobbelink, M. A. A. J. van den Bosch, R. M. H. Verheijen and W. B. Veldhuis, *J. Nucl. Med.*, 2016, **4**, 551.
- 26 P. T. Soliman, S. N. Westin, S. Dioun, C. C. Sun, E. Euscher, M. F. Munsell, N. D. Fleming, C. Levenback, M. Frumovitz, P. T. Ramirez and K. H. Lu, *Gynecol. Oncol.*, 2017, **2**, 234.
- 27 L. Huang, T. Wei, J. Chen and D. Zhou, *World J. Surg. Oncol.*, 2017, **15**(1), 103.

- 28 E. A. Newman and L. A. Newman, *Surg. Clin. North Am.*, 2007, **87**, 353.
- 29 C. Tausch, A. Baege and C. Rageth, *Oncotargets Ther.*, 2014, **7**, 1151.
- 30 M. J. Stoutjesdijk, C. Boetes, G. J. Jager, L. Beex, P. Bult, J. H. C. L. Hendrik, R. J. F. Laheij, L. Massuger, L. E. Van Die, T. Wobbes and J. O. Barentsz, *J. Natl. Cancer Inst.*, 2001, **93**, 1095.
- 31 S. K. Shetty and M. G. Harisinghani, *Appl. Radiol.*, 2004, **232**, 897.
- 32 R. Madru, P. Kjellman, F. Olsson, K. Wingardh, C. Ingvar, F. Stahlberg, J. Olsrud, J. Latt, S. Fredriksson, L. Knutsson and S. E. Strand, *J. Nucl. Med.*, 2012, **53**, 459.
- 33 R. Ting, T. A. Aguilera, J. L. Crisp, D. J. Hall, W. C. Eckelman, D. R. Vera and R. Y. Tsien, *Bioconjugate Chem.*, 2010, **21**(10), 1811, DOI: 10.1021/bc1001328.
- 34 M. R. S. Keshtgar and P. J. Ell, *Eur. J. Nucl. Med.*, 1999, **26**, 57.
- 35 G. Niu and X. Chen, Lymphatic Imaging: Focus on Imaging Probes, *Theranostics*, 2015, **5**(7), 686.
- 36 M. Yamabhai, S. Sak-Ubol, W. Srilaand and D. Haltrich, *Crit. Rev. Biotechnol.*, 2014, **1**, 32.
- 37 S. A. Ferreira, P. J. G. Coutinho and F. M. Gama, *Langmuir*, 2010, **26**, 11413.
- 38 Z. Cui, C. H. Hsu and R. J. Mumper, *Drug Dev. Ind. Pharm.*, 2003, **29**, 689.
- 39 N. Adams and U. S. Schubert, *Adv. Drug Delivery Rev.*, 2007, **59**, 1504, DOI: 10.1016/j.addr.2007.08.018.
- 40 H. Schlaad, C. Diehl, A. Gress, M. Meyer, A. L. Demirel, Y. Nur and A. Bertin, *Macromol. Rapid Commun.*, 2010, **31**, 511.
- 41 R. Hoogenboom and H. Schlaad, *Polymers*, 2011, **3**(1), 468.
- 42 P. Wilson, P. C. Ke, T. P. Davis and K. Kempe, *Eur. Polym. J.*, 2017, **88**, 486, DOI: 10.1016/j.eurpolymj.2016.09.011.
- 43 G. T. Hermanson, in *Bioconjugate techniques*, ed. J. Audet and M. Preap, Elsevier Inc., 3rd edn, 2013, vol. 3, pp. 229–258.
- 44 G. Pitarresi, C. Fiorica, F. S. Palumbo, S. Rigogliuso, G. Gherzi and G. Giammona, *J. Biomed. Mater. Res., Part A*, 2014, **102A**, 1334.
- 45 X. Xu, A. K. Jha, D. A. Harrington, M. C. Farach-Carson and X. Jia, *Soft Matter*, 2012, **8**, 3280.



OPEN Glycogen as an advantageous polymer carrier in cancer theranostics: Straightforward *in vivo* evidence

Andrea Gálisová¹, Markéta Jiráťová^{1,2}, Mariia Rabyk³, Eva Sticová^{4,5}, Milan Hájek¹, Martin Hrubý³ & Daniel Jiráček^{1,6,7}

As a natural polysaccharide polymer, glycogen possesses suitable properties for use as a nanoparticle carrier in cancer theranostics. Not only it is inherently biocompatible, it can also be easily chemically modified with various moieties. Synthetic glycogen conjugates can passively accumulate in tumours due to enhanced permeability of tumour vessels and limited lymphatic drainage (the EPR effect). For this study, we developed and examined a glycogen-based carrier containing a gadolinium chelate and near-infrared fluorescent dye. Our aim was to monitor biodistribution and accumulation in tumour-bearing rats using magnetic resonance and fluorescence imaging. Our data clearly show that these conjugates possess suitable imaging and tumour-targeting properties, and are safe under both *in vitro* and *in vivo* conditions. Additional modification of glycogen polymers with poly(2-alkyl-2-oxazolines) led to a reduction in the elimination rate and lower uptake in internal organs (lower whole-body background: 45% and 27% lower MRI signals of oxazoline-based conjugates in the liver and kidneys, respectively compared to the unmodified version). Our results highlight the potential of multimodal glycogen-based nanopolymers as a carrier for drug delivery systems in tumour diagnosis and treatment.

The majority of anticancer drugs are highly toxic and adversely affect healthy cells due to a lack of specific targeting^{1,2}. Therefore, a safe drug delivery system capable of accumulating and providing controlled drug release at the tumour site is highly desirable. Nanoparticles represent a versatile carrier for drug delivery due to their ability to passively accumulate in solid tumours. This occurs via the enhanced permeability and retention (EPR) effect, a relatively universal phenomenon whereby nano-sized structures (up to approx. 200 nm in size) become entrapped in tumour tissue due to either leaky endothelia or aberrant tumour vessel architecture. Restricted or even completely absent lymphatic drainage in tumours limits the release and passive accumulation of compounds³. Nanotherapeutic carrier can accumulate in tumours via the EPR effect without any targeting ligand⁴⁻⁶. Their size above the renal threshold (molecular weight > ca 45 kDa/hydrodynamic diameter > 8 nm) leads to prolonged circulation in the bloodstream increasing the probability of accumulation at the target site³. Importantly, polymers can control the release of drugs, being composed of a structure responsive to external stimuli, such as pH changes in acidic cancer-cell environments⁷, the presence of enzymes, and redox potential^{8,9}. Thus to minimise the drug release in the bloodstream and the cytotoxic effect on healthy cells¹⁰⁻¹².

One limitation of nanoparticles is that they tend to opsonise, clearing quickly through the reticuloendothelial system in the liver and spleen¹³. However, this can be mitigated by surface modification: for instance, grafting nanoparticles with poly(ethylene oxide) (PEO) (known also as poly(ethylene glycol) – PEG) is a well-established procedure for reducing nanoparticle toxicity, prolonging circulation in the bloodstream, and minimising interactions

¹MR Unit, Department of Radiodiagnostic and Interventional Radiology, Institute for Clinical and Experimental Medicine, Prague, Czech Republic. ²Department of Physiology, Faculty of Science, Charles University, Prague, Czech Republic. ³Institute of Macromolecular Chemistry, Academy of Sciences of the Czech Republic, Prague, Czech Republic. ⁴Department of Clinical and Transplant Pathology, Institute for Clinical and Experimental Medicine, Prague, Czech Republic. ⁵Department of Pathology, Third Faculty of Medicine, Charles University, Prague, Czech Republic. ⁶Institute of Biophysics and Informatics, First Faculty of Medicine, Charles University in Prague, Prague, Czech Republic. ⁷Department of Science and Research, Faculty of Health Studies, Technical University of Liberec, Liberec, Czech Republic. e-mail: daniel.jirak@ikem.cz

with the immune system¹⁴. On the other hand, PEO also has the potential to be both immunogenic and antigenic and degrading to produce reactive oxygen species^{15,16}. Therefore, alternative polymers such as poly(2-oxazolines) (POx) are currently the subject of extensive testing^{15,17,18}. POx are significantly more stable compared to PEO^{19,20}, retain their non-fouling (protein-repellent) potential, have low unspecific organ deposition and do not exhibit immunogenicity^{15,21,22}. This so-called “stealth” effect leads to the prolonged circulation of coated nanoparticles in the blood and increases the likelihood of accumulation in tumour tissue via the EPR effect²².

In addition to other tried-and-tested drug delivery systems such as proteins²³, synthetic polymers^{24–27} and carbon nanotubes²⁸, natural carbohydrate polymers such as polysaccharides are versatile and unique carriers due to their high biocompatibility, biodegradability, and availability^{29–32}. Polysaccharides can also be easily modified to control drug release while incorporating both diagnostic and therapeutic entities. Polysaccharide surfaces can also be tailored with ligands for more specific targeted delivery, e.g. using folate to bind to overexpressed folate receptors on cancer cells³³.

Most studies of polysaccharide drug delivery systems use alginate³⁴, dextran^{35,36}, chitosan^{37,38}, pectin^{39–42}, starch⁴³ or hyaluronic acid^{44,45}. However, only a few studies have explored the potential of glycogen^{32,46}. Glycogen is a natural hyperbranched polymer of suitable size for the EPR effect (hydrodynamic diameter \approx 50 nm, molecular weight \approx 10 MDa) and above the renal threshold, it is degraded into D-glucose by intracellular enzymes and further metabolized by normal physiological glycolysis⁴⁶. Moreover, it is biocompatible, biodegradable⁴⁷, widely available as a natural renewable resource (oysters, plants)^{48,49}, and can be easily modified with drugs or diagnostic moieties, what makes glycogen ideally suited for use in the construction of a multimodal drug delivery system^{32,46,50}.

In the absence of evidence to indicate glycogen is efficient as a nanocarrier in a clinically relevant model such as a tumour-bearing animal, we performed a detailed characterisation of a modified glycogen carrier under *in vivo* conditions on an animal tumor model of hepatocellular carcinoma (HUH7 human cancer cell line). Glycogen was modified with two imaging moieties: a gadolinium chelate for magnetic resonance (MR) and a near-infrared fluorescent dye for fluorescence imaging. A multimodal agent was deemed most favourable given each method provides a different set of information on biodistribution, accumulation, and clearance of probes under *in vivo* conditions. In order to enhance tumour-targeting properties and eliminate any possible adverse effects on other organs, the polymers were modified with POx. Using tumour-bearing rats, we evaluated imaging properties, biodistribution, safety, *in vivo* accumulation, and clearance. To the best of our knowledge, this is the first demonstration of imaging potential of these contrast agents on *in vivo* animal model.

Results

Imaging properties of polymers. Two polymer conjugate variants were synthesized: glycogen-based conjugates modified with POx (GOX) and glycogen-based conjugates without POx (GG). A commercially available MR contrast agent gadoterate meglumine (GM) served as a control. MR properties of the conjugates were examined by MR imaging at 4.7 T and relaxometry at 0.5 T. T_1 -weighted MR signals and corresponding contrast-to-noise ratio (CNR) values were linearly dependent on concentration of Gd^{3+} in the conjugates (Fig. 1a,c), with the highest signal issuing from GG. Relaxivity of the GG probe ($10.3 \pm 0.12 \text{ mM}^{-1} \text{ s}^{-1}$) was higher compared to the GM ($4.2 \pm 0.07 \text{ mM}^{-1} \text{ s}^{-1}$) and GOX ($3.0 \pm 0.16 \text{ mM}^{-1} \text{ s}^{-1}$) probes (Fig. 1e,f). Relaxivity of unmodified glycogen without imaging agents and oxazolines was $0.1 \pm 0.03 \text{ mM}^{-1} \text{ s}^{-1}$ (Fig. 1e,f). The higher CNR values of GG and GOX compared to GM reflect higher r_1 relaxivities. Fluorescence emission of probes was measured after specific excitation at 745 nm. While conjugates containing the fluorescent dye emitted a strong fluorescence signal linearly dependent on probe concentration, the control sample (GM) emitted no fluorescence signal after excitation (Fig. 1b,d). The fluorescence signals of GG and GOX were similar.

MR and fluorescence *in vivo* imaging of rats administered with conjugates. After intravenous administration of conjugates, we assessed biodistribution and accumulation of the glycogen-based probes (GG and GOX) and control agent (GM) using MR and fluorescence *in vivo* imaging (Fig. 2). The MR imaging experiment revealed accumulation of the glycogen-based conjugates in the tumour tissue with a higher uptake of GG and GOX agents compared to GM (Fig. 2b). The highest CNR values were obtained from tumours injected with GG throughout the whole examination (Fig. 2b,c). The GOX signal was lower than GG but higher than GM (Fig. 2c). The highest content of the probes in tumours was found on day 2 (Fig. 2b,c); the CNR values in tumours on day 2 reflecting accumulation of probes are shown in Fig. 2c. Accumulation of GG of concentration 0.02 mmol/kg increased between day 2 and 3, however this increase was within the standard deviation and not statistically significant. With the administration of higher probe concentrations, MR signals in tumours increased (Fig. 2b). The signals of the control sample (GM) was lower than GG and GOX throughout the whole examination confirming the target properties of the glycogen-based conjugates toward the tumour tissue. A CNR map analysis revealed increased MR signals, predominantly in tumour centres (Fig. 2a). To confirm that MR signals increased in line with accumulation in glycogen-based conjugates and not in fatty tissue (which gives also a positive signal on T_1 -weighted MR images), we carried out histological analysis of tumour tissues. Histology excluded the presence of fibrosis and steatosis, only necrosis was found in tumour centres.

Accumulation of GG and GOX in tumour tissues was confirmed also by fluorescence *in vivo* imaging (Fig. 2e). Fluorescence signals of all probes rapidly declined on day 1 (Fig. 2d) and therefore fluorescence is not suitable for assessing the long-term changes of probe accumulation. GG and GOX at 0.04 mmol Gd^{3+} /kg concentration levels remained above pre-injection values even 3 days after injection.

The probes tested were also accumulated in liver tissue. Higher MRI and fluorescence signals were observed in rat livers injected with GG compared to GOX throughout the whole examination ($p < 0.05$, paired t-test) (Fig. 3). The highest uptake was observed 2 hours after intravenous administration, with GG accumulation significantly higher than GOX ($p = 0.0001$) (Fig. 3f). MRI signals of all probes decreased to pre-injection values on day 7, despite the presence of a slightly elevated fluorescence of GG in the liver (Fig. 3d). Both MRI and fluorescence

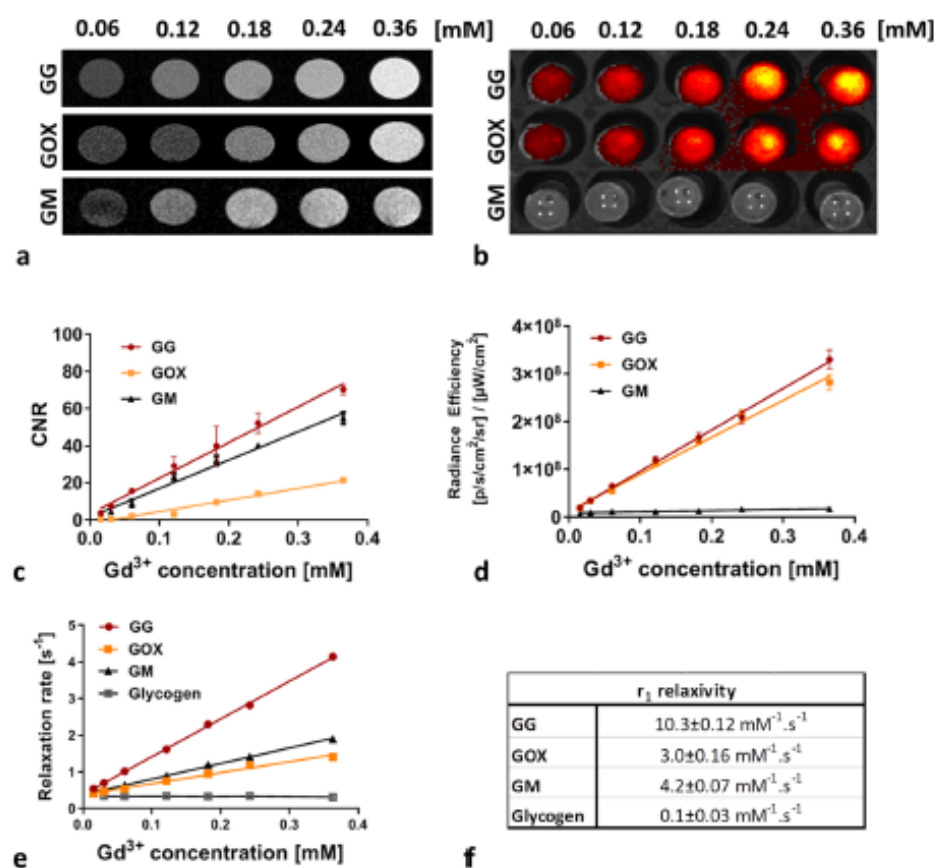


Figure 1. Characteristics of glycogen-based conjugates: (a) MR and (b) fluorescence images of conjugates at different Gd³⁺ concentrations, (c) with corresponding contrast-to-noise ratios (CNR) and (d) fluorescence radiance efficiency values; (e) dependence of MR relaxation rates R₁ on Gd³⁺ concentration of probes and (f) the corresponding r₁ relaxivities measured at 0.5 T.

signals showed a similar trend in the liver (Fig. 3e,f). The accumulation of the commercially-available probe (GM) was observed only within the first post-injection day.

Due to the attenuation of fluorescence in deeper tissues, probe uptake in the kidneys was analysed by MRI only. Signals from the GM control and modified glycogen-based GOX conjugate decreased to initial values 2 h after injection. The GG signal increased above the pre-injection value throughout the whole examination even at the lowest probe concentration (Fig. 4b) ($p < 0.01$, paired ANOVA test; $p < 0.01$ between GG and GOX, GG and GM on day 7, unpaired ANOVA) (Fig. 4d). The signal from the control probe GM was observed immediately after injection only and then it was cleared out.

Ex vivo fluorescence imaging. Fluorescence imaging is limited by its attenuation and refraction of optical signals in biological tissues, particularly in deeper structures. Therefore, to assess probe accumulation more precisely and to confirm the results of *in vivo* imaging, *ex vivo* fluorescence analysis of the internal organs (liver, kidneys, spleen and tumours) was performed at two time points: day 2 and day 7.

Corresponding to our *in vivo* MRI data, *ex vivo* analysis revealed GG continuously accumulated in tumours, with the highest uptake on day 7 following probe injection (Fig. 5a). GOX accumulation on day 2 was lower than GG, again in line with our *in vivo* imaging results. GOX shows relatively the same accumulation in the tumours on day 2 and day 7 in contrast to GG, which was uptaken faster on day 2. Fluorescence signal values from GOX and GM were within background signal ranges.

Apart from the lowest GG probe concentration, probe uptake in the liver was higher on day 2 than on day 7, a finding that corresponds with our *in vivo* results (Fig. 5b).

Similar to *in vivo* MRI, *ex vivo* fluorescence analysis of the kidneys confirmed higher accumulation of GG than GOX on day 7 (Fig. 5c) with a decrease in accumulation from day 2 to day 7. There was an initial accumulation of GG in the spleen on day 2, but no uptake of the other agents (GOX, GM). A persistent low fluorescence GG signal was also present in the spleen on day 7 (Fig. 5c). This discrepancy between the MRI and FLI signals from the kidneys on day 2 could be explained by lower r₁ relaxivity of the GOX conjugate and thus lower T₁ signal on

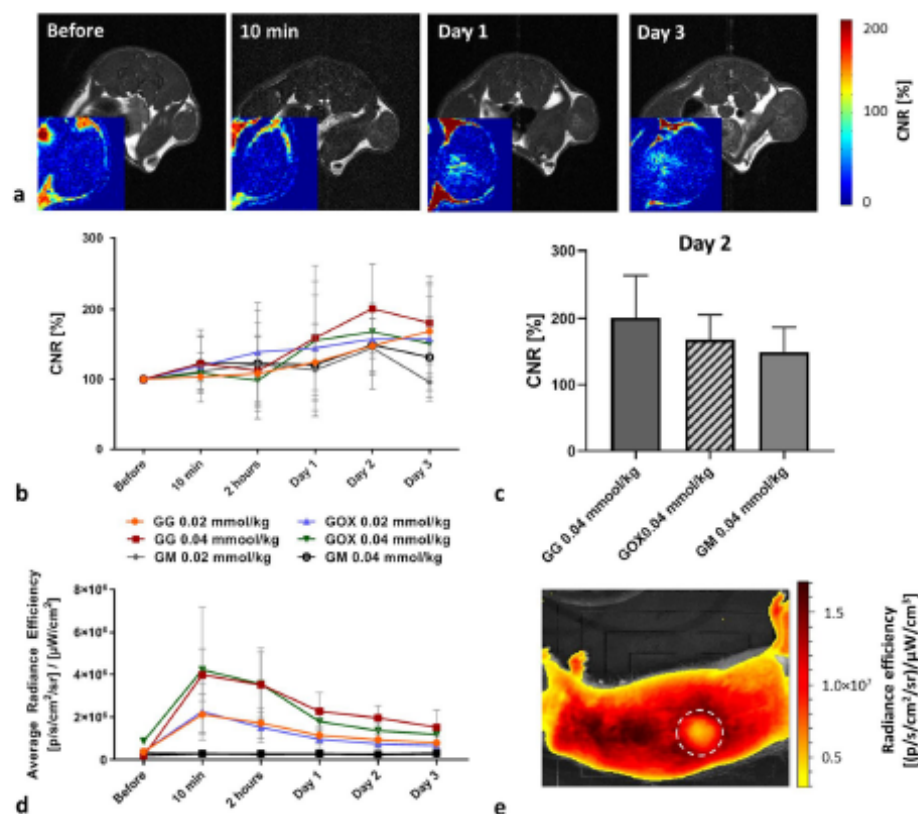


Figure 2. Accumulation of glycogen-based conjugates in tumours: (a) T_1 -weighted images of rats injected with GG; corresponding CNR maps (insets) show the accumulation of probes in tumour centres; (b) quantification of MR signals from tumours before and after probe injection; (c) CNR values in tumours on day 2 show higher accumulation of GG compared to GOX and GM; (d) fluorescence signals originating from tumours at different time points after glycogen probe injection; (e) representative fluorescence image of a rat injected with GG (sagittal plane); dotted circle marks the tumour area.

the T_1 -weighted MR images. Nevertheless, the fluorescence signals of GOX and GG on day 2 obtained by the *ex vivo* fluorescence are very similar and not statistically different.

Overall, probe accumulation increased over time in the tumours and kidneys. However, probe signals diminished over time after initial uptake in the liver and spleen.

Toxicity and biocompatibility of conjugates. MTT assay revealed no signs of toxicity in the conjugates tested. The level of absorbance at 570 nm reflected the level of cell proliferation. Compared to non-treated control cells, HUH7 cells incubated with glycogen-based polymers showed comparable or slightly higher absorbance (see Supplementary Table S1 online).

Serum levels of ALT, bilirubin, creatinine, and albumin were within physiological range, reflecting the healthy status of the polymer-injected rats. AST levels slightly increased after agent administration (including GM). However, it should be noted that control rats without tumours also exhibited higher AST values. Therefore, the increase might be connected to the specific rat strain used. Importantly, no difference was found between biochemical levels of all measured compounds in rats injected with glycogen-based probes and in those injected with commercial GM probes (see Supplementary Fig. S1 online).

Histological analysis confirmed the absence of significant pathological changes in parenchymal organs after administration of glycogen-based conjugates (Fig. 6). There were no necroinflammatory changes, steatosis or fibrosis in the liver tissue.

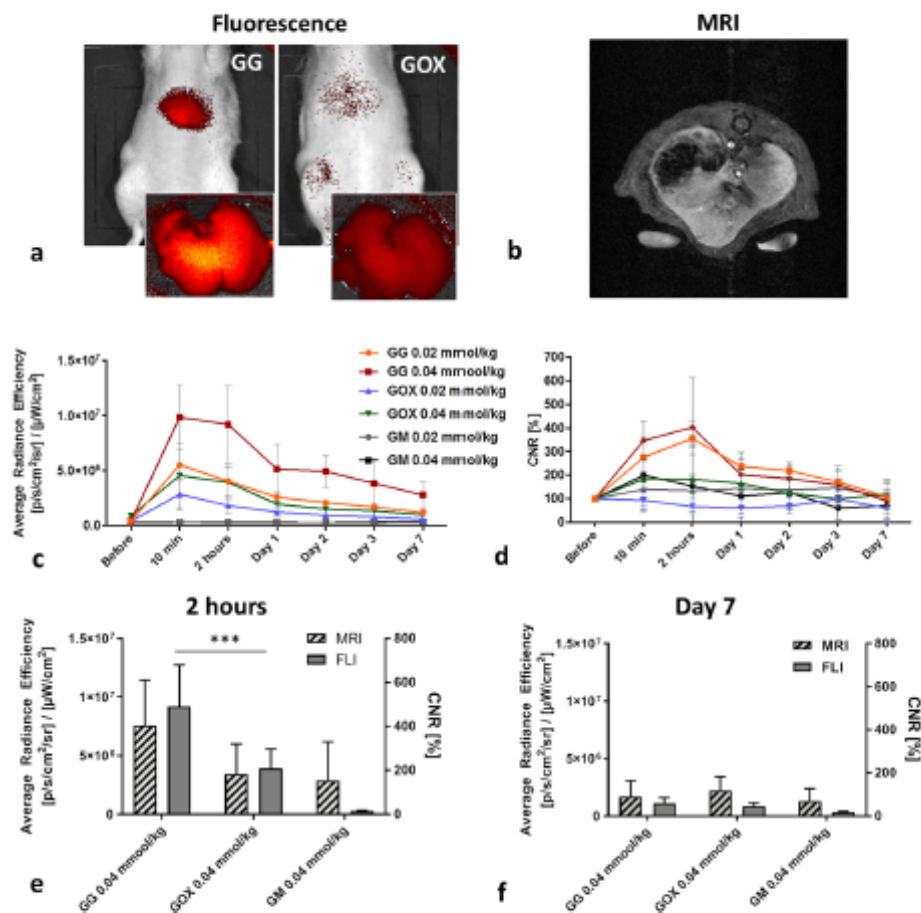


Figure 3. Accumulation of glycogen-based conjugates in the liver: (a) Representative fluorescence and (b) MRI images of rat livers injected with glycogen-based probes, (a) with insets showing detailed *ex vivo* fluorescent liver images; (c) quantification of fluorescence and (d) MRI signals from rat livers at different time points after probe administration; fluorescence (FLI) and MRI signals (e) 2 hours and (f) 7 days after injection reveal differences in the highest probe concentrations (0.04 mmol Gd^{3+}/kg).

Discussion

Glycogen nanoparticles represent a versatile, biocompatible, and biodegradable platform for polymer-based carriers, possessing advantageous physicochemical properties for biomedical applications³². They can also be modified with imaging probes, allowing them to be tracked using non-invasive imaging methods. In this study, we tested glycogen-based conjugates bearing imaging entities for MR visualisation and optical imaging in rats with solid tumours. Our aim was to monitor under experimental conditions *in vivo* behaviour of a glycogen-based carrier suitable for a wide variety of imaging methods and biological applications. Our polymers were also modified with bioconfluent POx to increase conjugate accumulation in tumour tissue, thus prolonging biodegradation and blood circulation time.

To prove the visualisation ability and sensitivity of probes using MR and optical imaging methods, we examined solutions of different conjugate concentrations. MR imaging, MR relaxometry, and fluorescence imaging proved suitably sensitive to glycogen nanoparticles. Boasting high MR relaxivity, good contrast on T_1 -weighted MR images, and strong fluorescence signals, the nanoparticles enable multimodal *in vivo* tracking. Even at the lowest tested concentrations, probe signals were clearly detectable (0.06 mM of Gd^{3+}) on MR images. Notably, glycogen concentrations of synthesised nanoparticles can even be increased where required. Although POx can enhance tumour targeting by slowing biodegradation and blood circulation time, our POx-modified polymers exhibited lower MR relaxivity, decreasing imaging effectiveness as a result. This effect may have been due either to the more restricted availability of water molecules in gadolinium chelates, or to the higher conformational mobility of gadolinium chelates at the end of POx chains compared to chelates directly attached to the glycogen core.

To evaluate drug delivery, polymer probes were tested for biodistribution, accumulation, and clearance in hepatocellular xenograft tumours using an animal cancer model. Our *in vivo* multimodal imaging results clearly

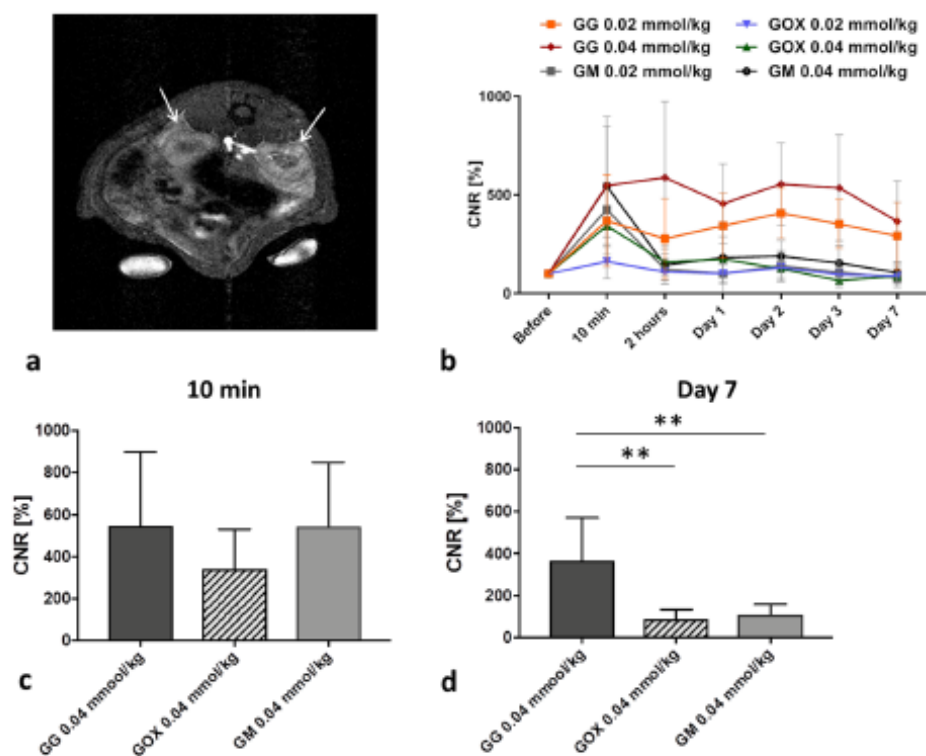


Figure 4. Accumulation of glycogen-based conjugates in the kidneys: (a) Representative MR image of kidneys (marked with arrows) after GG administration; (b) CNR values over time after glycogen-based probe administration; (c) quantification of CNR values originating from the highest probe concentrations (0.04 mmol Gd^{3+}/kg) at two different time points – (c) 10 min and (d) day 7.

confirmed the accumulation of glycogen-based conjugates in tumour tissue, displaying sustained MR contrast enhancement. Contrast in glycogen-based conjugates was higher than that observed in the commercial MR contrast agent, the plausible explanation being continuous accumulation due to the EPR effect. The difference between the commercial GM agent and the glycogen-based conjugates was highest on day 3 after i.v. injection. Glycogen-based probe accumulation peaked on day 2 in the case of GG (concentration of 0.04 mmol Gd^{3+}/kg), confirming it the carrier most suitable for drug delivery to tumours. It should be noted that tumours were monitored only until day 7, at which point massive tumour necrosis occurred (confirmed by histology), a finding that obviously compromises the validity of our MR data. Probe accumulation in tumours was also confirmed by *in vivo* and *ex vivo* fluorescence imaging. We observed a rapid decline in the *in vivo* fluorescence signal within the first days after administration. Previous animal model studies to have used other imaging probes report the dissociation of MR and fluorescence signals, a similar effect possibly caused by lysosomal degradation of fluorescent dyes^{51,52}.

Our *in vivo* MR data show that throughout the entire examination POx conjugates issued the lower MR signals, a result more attributable to lower MR relaxivity (3.4-times lower compared to GG) than to lower accumulation in tumours considering the corresponding fluorescence signals revealed no significant differences between the probes with and without POx. However, non-POx probes exhibited slightly higher fluorescence signals (for both *in vivo* and *ex vivo*), accumulating in greater amounts as a result.

All drug delivery systems need to minimise the toxic effect of the drug incorporated while mitigating effects on non-targeted tissue^{1,2}. To that end, the use of beneficial non-biofouling (protein-repellent) compounds such as POx and PEO¹⁴ is recommended. Confirming the stealth effect of POx, our model demonstrates that conjugates modified with POx slowed the elimination rate and reduced the uptake of POx-modified conjugates in rat livers, spleens and kidneys compared to the unmodified version (lower body background ratio; 45% and 27% lower MRI signals of oxazoline-based conjugates in the liver and kidneys, respectively compared to the unmodified version). We observed significantly lower *in vivo* MRI and fluorescence signals from POx-modified conjugates in the liver and kidneys throughout the whole examination, a finding supported by our *ex vivo* analysis of fluorescence signals from internal organs. Based on our results comparing tumours with other organs, POx not only caused internal organs to be protected against probe uptake but, in contrast to our expectations, inhibited accumulation in target tumour tissue.

The merits of any drug delivery system are largely dependent on its ability to ensure efficient clearance from the body. In our study, both MR and fluorescence imaging revealed that probes were eliminated from the

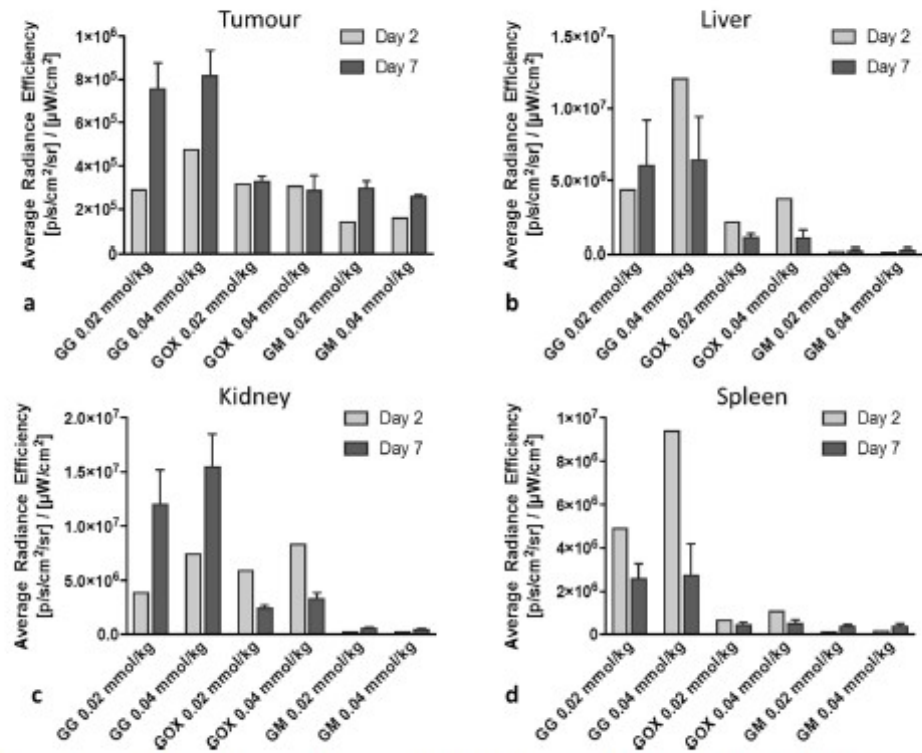


Figure 5. Quantification of *ex vivo* fluorescence signals in (a) tumours, (b) livers, (c) kidneys, and (d) spleens; fluorescence signals were higher on day 7 in tumours and kidneys.

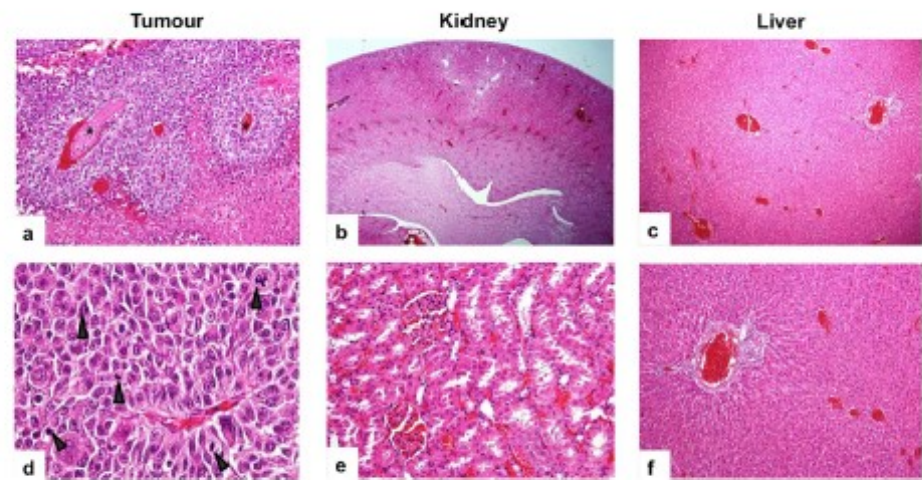


Figure 6. Histology of tumor and parenchymal organs after administration of the glycogen-based conjugates. (a) Tissue sections stained with haematoxylin-eosin (H&E) show tumor tissue with confluent coagulation necrosis (magnification 400×). (d) Neoplastic cells display significant nuclear atypia with increased mitotic activity (arrows) (magnification 600×). (b,e) H&E staining shows renal parenchyma (b, magnification 20×; e, magnification 400×) and (c,d) liver tissue (c, magnification 40×; f, magnification 100×) of preserved architecture with no apparent pathological changes after administration of the glycogen-based probes.

organism mainly through the kidneys, similar to the preferred elimination route of MR chelates such as DOTA. As predicted, polymer modification with oxazolines reduced renal clearance. Elevated MR signals in the kidneys of rats administered polymers without POx persisted even 7 days after application, raising safety concerns and underscoring the importance of oxazoline modification. However, it should be noted that Gd^{3+} probe concentrations were much lower (up to 0.04 mmol Gd^{3+} /kg) compared to standard doses routinely administered in human medicine (approximately 0.1 mmol Gd^{3+} /kg)⁵². Therefore, we assume any adverse effect of Gd^{3+} was minimal. Moreover, in our model, we found no pathological changes in organs, confirmed by histological and biochemical analysis of blood proteins. Given our glycogen-based conjugates were uptaken by cells via endocytosis and intracellularly degraded into D-glucose units⁴⁶, we assume they degraded to form water and carbon dioxide in tumour tissue. Similar to commercial clinically approved Gd-based MR contrast agents, we hypothesise the released chelate (DOTA) and fluorescent dye were then cleared from the body by the kidneys or liver. Nevertheless, it should be noted that these conjugates can carry other imaging moieties, thus impacting on sensitive radionuclides and certain applications such as ¹⁹F MR probes.

The most important factor to consider when designing any drug delivery system is toxicity risk. Our biochemistry and immunohistochemistry results confirm the non-toxicity and biocompatibility of the glycogen-based carriers tested. Incubated cells exposed to probes showed comparable viability and proliferation to controls. Moreover, no prominent changes in blood serum protein levels were detected after intravenous probe administration in rats. Importantly, histology examination revealed no pathological changes in internal organs (liver, kidneys or spleen) after administration.

A key advantage of our drug delivery model for future applications is that it can be tailored to release drugs at particular sites of interest and/or under specific biological conditions, e.g. pH changes in solid tumours⁵⁴, thus providing safe and effective anticancer treatment for specific types of tumours.

Conclusion

In this study, we demonstrate that our novel glycogen-based compounds are suitable for multimodal imaging of solid tumours, being of the requisite biological properties for tumour targeting. Biocompatible and safe, these compounds can be easily modified to control the biological fates of these conjugates. Although oxazoline modification prevents uptake of probes in internal organs, it also inhibits accumulation in target tumour tissue. Both our *in vitro* and *in vivo* results highlight the potential of glycogen-based probes as carriers for drug delivery systems in tumour diagnosis and treatment.

Methods

Glycogen (type II from oysters) was used for nanoparticle synthesis. Two polymer conjugate variants were prepared: glycogen-based conjugates modified with POx (GOX) and glycogen-based conjugates without POx (GG). Glycogen conjugates grafted and non-grafted with GOX were synthesised as previously described⁴⁶.

MR imaging and relaxometry of polymers. MR imaging was performed on a 4.7 T scanner (Bruker BioSpin, Germany) using a resonator coil with an internal diameter of 7 cm (Bruker BioSpin, Germany). MR images were processed using ImageJ software (version 1.46r, National Institute of Health, USA). All optical images (fluorescence) were acquired on an IVIS Lumina XR imager (Perkin Elmer, USA) and processed using Living Image software (Perkin Elmer, USA).

We examined the MR and optical properties of GG, GOX, and GM, a commercial MR contrast agent used as a control. MR relaxivity (r_1) of conjugates was assessed by measuring T_1 relaxation times at various probe concentrations (0.01–0.36 mM Gd^{3+}) on a 0.5 T relaxometer (Bruker BioSpin, Germany) using a saturation recovery sequence (recycle delay 12 s or 5 s depending on T_1 values).

T_1 -weighted MR images of conjugates in tubes were acquired using a Rapid Acquisition with Refocused Echoes (RARE) sequence (repetition time (TR) = 125 ms, echo time (TE) = 11.6 ms, spatial resolution $0.2 \times 0.2 \times 1.5$ mm³, scan time 6 min 24 s). A tube filled with water served as a reference. Regions of interest (ROI) of the same size were drawn around each sample in MR images, with the CNR between the reference and sample of choice calculated for each agent concentration.

Fluorescence images of the same samples were acquired during a 2-second exposure using aperture (f/stop) 4 and binning 4. Fluorescence excitation was set at 745 nm and emission at 810–875 nm. ROIs were drawn around each tube, with the emitted optical signal expressed as the radiance efficiency ([photons/sec/cm²/sr]/(μW/cm²)). Fluorescence images were overlaid on photographs to localise the optical signal.

Animal model. All animal protocols were approved by the Ethics Committee of the Institute for Clinical and Experimental Medicine and the Ministry of Health of the Czech Republic (No. 58/2014) in accordance with the European Communities Council Directive (2010/63/EU). Animals were kept in ventilated cages under a 12-h light cycle and given free access to food and water.

Tumours were induced in immunodeficient RNU nude rats (Velaz, Czech Republic) by subcutaneous injection of HUH7 cells (5×10^6) above the right hind leg. During implantation, animals were anaesthetised by isoflurane inhalation (5% for induction, 1% for maintenance). Prior to implantation, cells were cultured for 2 weeks in a DMEM culture medium supplemented with 10% foetal bovine serum (FBS), 5% L-glutamine, and a 5% penicillin/streptomycin solution (37°C, 5% CO₂).

Animals (n = 48) were divided into 6 experimental groups according to the type of conjugate administered and based on two concentrations: GG 0.02 mmol Gd^{3+} /kg; GG 0.04 mmol Gd^{3+} /kg; GOX 0.02 mmol Gd^{3+} /kg; GOX 0.04 mmol Gd^{3+} /kg; GM 0.02 mmol Gd^{3+} /kg and GM 0.04 mmol Gd^{3+} /kg (n = 8 in each group).

In vivo examination – MR and fluorescence imaging. Animals were kept under general inhalation anaesthesia for the duration of all *in vivo* imaging experiments (isoflurane: 5% for induction, 1% for maintenance). Body temperature was maintained using a heating system, with breathing monitored throughout.

Three weeks after tumour induction, T₁-weighted MR images of tumours, livers and kidneys were acquired before and after intravenous administration of GG, GOX and GM at two concentrations (0.02/0.04 mmol Gd³⁺/kg). MR imaging was performed before, immediately after, and then 10 min, 2 h, 1, 2, 3 and 7 days after conjugate administration.

MRI examination parameters were as follows: spin-echo sequence for tumour imaging with TR = 125 ms, TE = 11.6 ms, spatial resolution 0.25 × 0.25 × 1.50 mm³, 8 acquisitions, scan time 4 min 16 s; gradient echo sequence for the liver and kidneys: TR = 72 ms, TE = 4.6 ms, spatial resolution 0.25 × 0.25 × 1.50 mm³, 12 acquisitions, scan time 3 min 41 s. CNR values of the tumour, liver and kidneys in relation to muscle tissue were calculated at each time point from ROIs manually outlined around each tissue type. CNR maps were calculated based on pixel-wise processing of MR images using a custom-written script in Matlab (Matlab, MathWorks, Natick, MA, USA).

After MRI, near-infrared fluorescence images (excitation at 745 nm, emission at 810–875 nm) of rat tumours and livers were acquired based on a 30-second exposure time, aperture 4 (*f*/stop) and binning 4. Fluorescence images were overlaid on photographs for anatomic localisation of the optical signal. The average fluorescence efficiency ([(photons/sec/cm²/sr)/(μW/cm²)] was calculated from each ROI outlined around the liver and tumour tissues.

Toxicity and biocompatibility was evaluated with the MTT test and biochemical analysis of the blood serum proteins. Details of the tests are listed in the Supplementary Information.

One week after intravenous administration of the probes, selected rats were sacrificed (n = 2 per each group) and internal organs removed for histological analysis. Tumours, livers, kidneys and spleens were placed in a 4% formaldehyde solution overnight (pH 7.4) at 4°C and then embedded in paraffin blocks. Paraffin samples were cut into 4-μm tissue sections and routinely stained with haematoxylin and eosin. Each organ was examined for the presence of pathological changes by an experienced pathologist.

Statistical analysis. Statistical analysis was performed using GraphPad Prism 6.02 (GraphPad Prism Software Inc, USA). A standard two-tailed Student's t-test was used to compare differences between groups. Comparisons of three or more groups were performed by analysis of variance (one-way ANOVA), with the significance level set at p < 0.05. For mean values and standard deviations, see graphs.

Data availability

All relevant data are included in the manuscript and the supplementary information. Used datasets are available from the corresponding author on reasonable request.

Received: 7 February 2020; Accepted: 2 June 2020;

Published online: 26 June 2020

References

- Sikes, R. Chemistry and pharmacology of anticancer drugs. *Br. J. Cancer* **97**, 1713 (2007).
- Nussbaumer, S., Bonnabry, P., Veuthey, J. & Fleury-Souverain, S. Analysis of anticancer drugs: A review. *Talanta* **85**, 2265–89 (2011).
- Greish, K. Enhanced permeability and retention (EPR) effect for anticancer nanomedicine drug targeting. *Methods Mol. Biol.* **624**, 25–37 (2010).
- Duncan, R. The dawning era of polymer therapeutics. *Nat. Rev. Drug Discov.* **2**, 347–360 (2003).
- Seymour, L. *et al.* Tumouritropism and anticancer efficacy of polymer-based doxorubicin prodrugs in the treatment of subcutaneous murine B16F10 melanoma. *Br. J. Cancer* **70**, 636–641 (1994).
- Fang, J., Nakamura, H. & Maeda, H. The EPR effect: Unique features of tumor blood vessels for drug delivery, factors involved, and limitations and augmentation of the effect. *Adv. Drug Deliv. Rev.* **63**, 136–151 (2011).
- Dadsetan, M. *et al.* Controlled release of doxorubicin from pH-responsive microgels. *Acta Biomater.* **9**, 5438–5446 (2014).
- Gao, S. *et al.* Stimuli-responsive bio-based polymeric systems and their applications. *J. Mater. Chem. B* **7**, 709–729 (2019).
- Bruneau, M. *et al.* Systems for stimuli-controlled release: Materials and applications. *J. Control. Release* **294**, 355–371 (2019).
- Jinhyun, H. L. & Yoon, Y. Controlled Drug Release from Pharmaceutical Nanocarriers. *Chem. Eng. Sci.* **125**, 75–84 (2015).
- Maeda, H., Nakamura, H. & Fang, J. The EPR effect for macromolecular drug delivery to solid tumors: Improvement of tumor uptake, lowering of systemic toxicity, and distinct tumor imaging *in vivo*. *Adv. Drug Deliv. Rev.* **65**, 71–9 (2013).
- Acharya, S. & Sahoo, S. K. PLGA nanoparticles containing various anticancer agents and tumour delivery by EPR effect. *Adv. Drug Deliv. Rev.* **63**, 170–83 (2011).
- Gustafson, H. H., Holt-Casper, D., Grainger, D. W. & Ghandehari, H. Nanoparticle uptake: The phagocyte problem. *Nano Today* **10**, 487–510 (2015).
- Suk, J. S., Xu, Q., Kim, N., Hanes, J. & Ensign, L. M. PEGylation as a strategy for improving nanoparticle-based drug and gene delivery. *Adv. Drug Deliv. Rev.* **99**, 28–51 (2016).
- Luxenhofer, R. *et al.* Poly(2-oxazoline)s as polymer therapeutics. *Macromol. Rapid Commun.* **33**, 1613–31 (2012).
- Ulbricht, J., Jordan, R. & Luxenhofer, R. On the biodegradability of polyethylene glycol, polypeptides and poly(2-oxazoline)s. *Biomaterials* **35**, 4848–4861 (2014).
- Hrabý, M., Filippov, S. & Štěpánek, P. Smart polymers in drug delivery systems on crossroads: Which way deserves following? *Eur. Polym. J.* **65**, 82–97 (2015).
- Verbraken, B., Monnery, B. D., Lava, K. & Hoogenboom, R. The chemistry of poly(2-oxazoline)s. *Eur. Polym. J.* **88**, 451–469 (2017).
- Bauer, M. *et al.* Poly(2-ethyl-2-oxazoline) as alternative for the stealth polymer poly(ethylene glycol): Comparison of *in vitro* cytotoxicity and hemocompatibility. *Mascomolecular Biosci.* **12**, 986–98 (2012).
- Konradi, R., Pidhatiká, B., Muhlebach, A. & Textor, M. Poly-2-methyl-2-oxazoline: A peptide-like polymer for protein-repellent surfaces. *Langmuir* **24**, 613–616 (2008).
- Amozgar, Z. & Yeo, Y. Recent advances in stealth coating of nanoparticle drug delivery systems. *Wiley Interdiscip. Rev. Nanomed. Nanobiotechnol.* **4**, 219–33 (2012).
- Glassner, M., Vergaelen, M. & Hoogenboom, R. Poly(2-oxazoline)s: A comprehensive overview of polymer structures and their physical properties. *Polym. Int.* **67**, 32–45 (2018).

23. Sebak, S., Mirzaei, M., Malhotra, M., Kulamarva, A. & Prakash, S. Human serum albumin nanoparticles as an efficient nescapine drug delivery system for potential use in breast cancer: preparation and *in vitro* analysis. *Int. J. Nanomedicine* **5**, 525–532 (2010).
24. Nguyen, P. M. & Hammond, P. T. Amphiphilic linear-dendritic triblock copolymers composed of poly(amidoamine) and poly(propylene oxide) and their micellar-phase and encapsulation properties. *Langmuir* **22**, 7825–32 (2006).
25. Rudolph, C., Lausier, J., Naundorf, S., Müller, R. H. & Rosenecker, J. *In vivo* gene delivery to the lung using polyethylenimine and fractured polyamidoamine dendrimers. *J. Gene Med.* **2**, 269–278 (2000).
26. Sedláček, O. *et al.* 19F magnetic resonance imaging of injectable polymeric implants with multiresponsive behavior. *Chem. Mater.* **30**, 4892–4896 (2018).
27. Zhao, J., Yang, H., Li, J., Wang, Y. & Wang, X. Fabrication of pH-responsive PLGA(UCNPs/DOX) nanocapsules with upconversion luminescence for drug delivery. *Sci. Rep.* **7**, 18014 (2017).
28. Ganji, M. D., Mirzaei, S. & Dalirandeh, Z. Molecular origin of drug release by water boiling inside carbon nanotubes from reactive molecular dynamics simulation and DFT perspectives. *Sci. Rep.* **7**, 4669 (2017).
29. Larson, N. & Hamidreza, G. Polymeric Conjugates for Drug Delivery. *Chem. Mater.* **24**, 840–853 (2012).
30. Tian, H., Tang, Z., Zhuang, X., Chen, X. & Jing, X. Biodegradable synthetic polymers: Preparation, functionalization and biomedical application. *Prog. Polym. Sci.* **37**, 237–280 (2012).
31. Ulery, B., Nair, L. & Laurencin, C. Biomedical applications of biodegradable polymers. *J. Polym. Sci. B. Polym. Phys.* **49**, 832–864 (2011).
32. Filippov, S. *et al.* Glycogen as a biodegradable construction nanomaterial for *in vivo* use. *Macromol. Biosci.* **12**, 1731–8 (2012).
33. Zhang, L. *et al.* Folate-decorated polysaccharide-doxorubicin polymer: Synthesis, characterization, and activity in HeLa cells. *Bull. Korean Chem. Soc.* **36**, 1999–2005 (2015).
34. Tonnesen, H. H. & Karlens, J. Alginate in drug delivery systems. *Drug Dev. Ind. Pharm.* **28**, 621–630 (2002).
35. Wang, H. *et al.* Self-assembly assisted fabrication of dextran-based nanohydrogels with reduction-cleavable junctions for applications as efficient drug delivery systems. *Sci. Rep.* **7**, 40011 (2017).
36. Huang, S. & Huang, G. Preparation and drug delivery of dextran-drug complex. *Drug Deliv.* **26**, 252–261 (2019).
37. Sreekumar, S., Goycoolea, F. M., Moerschbacher, M. & Rivera-Rodriguez, G. Parameters influencing the size of chitosan-TPP nano- and microparticles. *Sci. Rep.* **8**, 4695 (2018).
38. Babu, A. *et al.* Chemodrug delivery using integrin-targeted PLGA-Chitosan nanoparticle for lung cancer therapy. *Sci. Rep.* **7**, 14674 (2017).
39. Morris, G., Kok, M., Harding, S. & Adams, G. Polysaccharide drug delivery systems based on pectin and chitosan. *Biotechnol. Genet. Eng. Rev.* **27**, 257–284 (2010).
40. Kean, T. & Thanou, M. Biodegradation, biodistribution and toxicity of chitosan. *Adv. Drug Deliv. Rev.* **62**, 3–11 (2010).
41. Varshosaz, J. Dextran conjugates in drug delivery. *Expert. Opin. Drug. Deliv.* **9**, 509–23 (2012).
42. Cascone, M. & Maltinti, S. Hydrogels based on chitosan and dextran as potential drug delivery systems. *J. Mater. Sci. Mater. Med.* **10**, 301–307 (1999).
43. Paleos, C. M., Sideratou, Z. & Tsiourvas, D. Drug delivery systems based on hydroxyethyl starch. *Bioconjug. Chem.* **28**, 1611–1624 (2017).
44. Xu, X., Jha, A., Harrington, D., Farach-Carson, M. & Jia, X. Hyaluronic acid-based hydrogels: From a natural polysaccharide to complex networks. *Soft Matter* **8**, 3280–3294 (2012).
45. Smejkalova, D. *et al.* Selective *in vitro* anticancer effect of superparamagnetic iron oxide nanoparticles loaded in hyaluronan polymeric micelles. *Biomacromolecules* **15**, 4012–4020 (2014).
46. Jiratova, M. *et al.* Biological characterization of a novel hybrid copolymer carrier system based on glycogen. *Drug Deliv. Transl. Res.* **8**, 73–82 (2018).
47. Adeva, M. M., González-Lucán, M., Donapetry-García, C., Fernández, C. & Rodríguez, E. A. Glycogen metabolism in humans. *Biochim. Biophys. Acta* **1864**, 85–100 (2016).
48. Matsui, M., Kakut, M. & Misaki, A. Fine structural features of oyster glycogen: mode of multiple branching. *Carbohydr. Polym.* **31**, 227–235 (1997).
49. Jean-Luc, P., Buléon, A., Borsali, R. & Chanzy, H. Ultrastructural aspects of phyto-glycogen from cryo-transmission electron microscopy and quasi-elastic light scattering data. *Int. J. Biol. Macromol.* **26**, 145–150 (1999).
50. Vetrík, M. *et al.* Biopolymer-based degradable nanofibres from renewable resources produced by freeze-drying. *RSC Adv* **3**, 15282–15289 (2013).
51. Galisova, A. *et al.* A trimodal imaging platform for tracking viable transplanted pancreatic islets *in vivo*: F-19 MR, fluorescence, and bioluminescence imaging. *Mol. Imaging Biol.* **21**, 454–464 (2018).
52. Bouvain, P. *et al.* Dissociation of 19F and fluorescence signal upon cellular uptake of dual-contrast perfluorocarbon nanoemulsions. *Magn. Reson. Mater. Physics, Biol. Med.* **32**, 133–145 (2019).
53. Lin, S. P. & Brown, J. J. MR contrast agents: physical and pharmacologic basics. *J. Magn. Reson. Imaging* **25**, 884–99 (2007).
54. Kato, Y. *et al.* Acidic extracellular microenvironment and cancer. *Cancer Cell Int.* **13**, 89 (2013).

Acknowledgements

This study was supported by the Ministry of Health of the Czech Republic (Institute for Clinical and Experimental Medicine – IKEM, Project IN 00023001) and the Ministry of Education, Youth and Sports of the Czech Republic (Grant no: LTC19032). M.Hrubý and M.R. wish to acknowledge the Czech Grant Foundation (Grant no: 18-07983S) for its assistance.

Author contributions

A.G. designed the experiment, collected and analysed the data, was responsible for the data interpretation and wrote the manuscript, M.J. collected the data, M.R. synthesised the nanoparticles, E.S. performed the histological analysis, M. Hájek supervised the MR facility, M. Hrubý supervised the chemistry lab, D.J. designed and supervised the project, was responsible for the data interpretation and integrity of this work. All authors reviewed the manuscript and approved the final version.

Competing interests

The authors declare no competing interests.

Additional information

Supplementary information is available for this paper at <https://doi.org/10.1038/s41598-020-67277-y>.

Correspondence and requests for materials should be addressed to D.J.

Reprints and permissions information is available at www.nature.com/reprints.

Publisher's note Springer Nature remains neutral with regard to jurisdictional claims in published maps and institutional affiliations.




Open Access This article is licensed under a Creative Commons Attribution 4.0 International License, which permits use, sharing, adaptation, distribution and reproduction in any medium or format, as long as you give appropriate credit to the original author(s) and the source, provide a link to the Creative Commons license, and indicate if changes were made. The images or other third party material in this article are included in the article's Creative Commons license, unless indicated otherwise in a credit line to the material. If material is not included in the article's Creative Commons license and your intended use is not permitted by statutory regulation or exceeds the permitted use, you will need to obtain permission directly from the copyright holder. To view a copy of this license, visit <http://creativecommons.org/licenses/by/4.0/>.

© The Author(s) 2020

Article

Mannan-Based Nanodiagnostic Agents for Targeting Sentinel Lymph Nodes and Tumors

Markéta Jirátová^{1,2}, Andrea Gálisová¹, Maria Rabyk³, Eva Sticová¹, Martin Hrubý³ and Daniel Jiráček^{1,4,*} 

¹ Institute for Clinical and Experimental Medicine (IKEM), 140 21 Prague, Czech Republic; marketa.jiratova@gmail.com (M.J.); a.galisova@gmail.com (A.G.); evs@ikem.cz (E.S.)

² Department of Physiology, Faculty of Science, Charles University, 128 00 Prague, Czech Republic

³ Institute of Macromolecular Chemistry, Czech Academy of Sciences, 162 00 Prague, Czech Republic; maria.rabyk@gmail.com (M.R.); mhruby@centrum.cz (M.H.)

⁴ Institute of Biophysics and Informatics, 1st Faculty of Medicine, Charles University, 121 08 Prague, Czech Republic

* Correspondence: daji@ikem.cz

Abstract: Early detection of metastasis is crucial for successful cancer treatment. Sentinel lymph node (SLN) biopsies are used to detect possible pathways of metastasis spread. We present a unique non-invasive diagnostic alternative to biopsy along with an intraoperative imaging tool for surgery proven on an *in vivo* animal tumor model. Our approach is based on mannan-based copolymers synergistically targeting: (1) SLNs and macrophage-infiltrated solid tumor areas via the high-affinity DC-SIGN (dendritic cell-specific intercellular adhesion molecule-3-grabbing non-integrin) receptors and (2) tumors via the enhanced permeability and retention (EPR) effect. The polymer conjugates were modified with the imaging probes for visualization with magnetic resonance (MR) and fluorescence imaging, respectively, and with poly(2-methyl-2-oxazoline) (POX) to lower unwanted accumulation in internal organs and to slow down the biodegradation rate. We demonstrated that these polymer conjugates were successfully accumulated in tumors, SLNs and other lymph nodes. Modification with POX resulted in lower accumulation not only in internal organs, but also in lymph nodes and tumors. Importantly, we have shown that mannan-based polymer carriers are non-toxic and, when applied to an *in vivo* murine cancer model, offer promising potential as the versatile imaging agents.

Keywords: mannan; SLN; cancer; multimodality imaging; 4T1 cells; MRI



Citation: Jirátová, M.; Gálisová, A.; Rabyk, M.; Sticová, E.; Hrubý, M.; Jiráček, D. Mannan-Based Nanodiagnostic Agents for Targeting Sentinel Lymph Nodes and Tumors. *Molecules* **2021**, *26*, 146. <https://doi.org/10.3390/molecules26010146>

Academic Editor: Takuya Terai
Received: 12 December 2020
Accepted: 29 December 2020
Published: 31 December 2020

Publisher's Note: MDPI stays neutral with regard to jurisdictional claims in published maps and institutional affiliations.



Copyright: © 2020 by the authors. Licensee MDPI, Basel, Switzerland. This article is an open access article distributed under the terms and conditions of the Creative Commons Attribution (CC BY) license (<https://creativecommons.org/licenses/by/4.0/>).

1. Introduction

It is widely known that cancer is one of the leading causes of death worldwide, and despite the huge progress in cancer treatment over the recent years, many of the mechanisms involved in the complex process of tumor and especially metastasis development are still not fully understood. To address this deficit, efforts are being made to more precisely diagnose and treat metastasis spreading. Axillary lymph node (ALN) status serves as a metastasis prognostic factor. As an alternative to ALN dissection, sentinel lymph node (SLN) biopsy is used as a standard clinical procedure [1–3]. SLNs play a key role in metastasis spreading as they form the lymphatic drainage system closest to the tumor and therefore, they are the most probable site of early metastasis [4]. However, SLN biopsy is still an invasive procedure with the possibility of complications. In addition to biopsy, various methods are used for metastasis and SLN detection, including standard blue-dye intraoperative detection and imaging methods such as magnetic resonance imaging (MRI) [5–7], ultrasound [8], single-photon emission computed tomography (SPECT), fluorescence, lymphoscintigraphy, and others [9,10]. Each method provides different information, but also comes with limitations, e.g., the low specificity of MRI and the optical signal attenuation. Multimodal imaging is used to overcome these issues. Combining MRI with sensitive

and convenient optical imaging provides complementary and precise information on the anatomy as well as the distribution and degradability of contrast agents and drug delivery systems. Reliable imaging methods are crucial for improving both the accuracy of SLN detection and the efficiency of drug delivery systems. To that end, the ultimate goal is to create a specific, selective and non-invasive method of SLN metastasis prediction.

Macrophages, which are heavily present in SLNs, are one of the most important factors in cancer-promoting inflammatory reactions [11] as they are also accumulated in cancer tissue. These tumor-associated macrophages (TAMs) affect inflammation of the stroma among other effects [12]. Macrophages and dendritic cells express the dendritic cell-specific intercellular adhesion molecule-3-grabbing non-integrin (DC-SIGN) receptor on their surface [13,14], which is a target of mannan-based polymer carriers. Mannans high affinity to DC-SIGN mediated by 3- and 4-OH groups on mannans was previously proved in many other applications than targeting SLNs [15–19].

TAMs and dendritic cells could be targeted not only via their surface DC-SIGN receptor but also via different targeting strategies based on nanotherapeutic, drug delivery, immunotherapeutic or nano-immunotherapeutic approaches [20,21]. More specifically, dendritic cells express not only DC-SIGN receptors, but also toll-like receptors. Some of the immunotherapeutic approaches use toll-like receptors agonists for dendritic cells targeting [22]. Each of the respective approaches possess its own strengths and also limitations. However, we believe that mannan-based copolymers are quite universal and represent a versatile platform.

Mannans are well known for their use in the food industry [23,24], but their myriad biological functions include also storage and cell-wall signaling [25]. Mannan from yeast is formed by D-mannose units connected by $\alpha(1-6)$ bonds (backbone) and $\alpha(1-2)$ and $\alpha(1-3)$ bonds (branches) [26]. In this work, commercially available mannan from *Saccharomyces cerevisiae* was used as a biocompatible platform for mannan conjugate preparation that enables addition of other modalities (imaging probes, etc.). Natural polymers and, especially, polysaccharides such as mannans, provide benefit in that they are biocompatible, biodegradable and widely available within renewable resources [27]. Their sizes can also be easily modified to enable passive accumulation in solid tumors.

The optimal size for passive accumulation of the nanoparticles inside the solid tumors via the enhanced permeability and retention (EPR) effect is approx. up to 200 nm. The EPR effect is caused by a combination of highly permeable newly formed blood vessels and limited lymphatic drainage in tumors [28,29]. Nevertheless, the contribution of the EPR effect to the total accumulation of nanoprobings inside tumors may be affected by physiological features such as tumor intestinal fluid pressure [30,31]. Moreover, there has been a controversy about the EPR effect contribution to the nanoprobings accumulation inside solid tumors. Sindhvani et al. showed that large proportion of the nanoparticles are endocytosed actively into the solid tumors by endothelial cells [32].

Polymer accumulation in tumors via the EPR effect can be influenced by polysaccharides grafting to succinic acid or biocompatible synthetic polymers, a process that decreases the biodegradation rate and enables further chemical modification. This effect has been demonstrated for various types of polysaccharides, such as chitosan and dextrin [33,34]. For our purposes, grafting by poly(2-methyl-2-oxazoline) (POX) was chosen because of its low unspecific organ deposition, low immunogenicity [35,36] and higher stability compared to the polyethylene glycol (PEG) [37]. However, in recent years there is a need for an alternative like POX because of increasing evidence of anti-PEG immunity [38]. There has been reported anti-PEG antibodies not only in pretreated individuals but also in healthy population without previous treatment. The main issue with the anti-PEG antibodies is that they may limit treatment efficacy as well as they enhance adverse effect [39,40] and so the use of the POX seems to be a better grafting modality for nanomedicine field.

In this article, we compared a hybrid copolymer platform based on a biodegradable mannan core grafted with biocompatible hydrophilic POX with a hybrid copolymer without POX to verify the POX effect on accumulation in organs and tumors. Both mannan-based

conjugates were grafted also with gadolinium as the MR (magnetic resonance) contrast agent and the fluorescent probe IR800CW for multimodal imaging. POX grafting adjusts the biodegradation rate in dependence on its grafted dose. Both probes were previously tested on healthy animals in pilot experiments [41], with the results indicating favorable biological characteristics for potential use in experimental and clinical medicine.

Here a successful proof of the diagnostic potential of the mannan-based probes for SLNs detection in a relevant tumor animal model is shown together with a detailed toxicity and in vitro/in vivo characterization.

2. Results

2.1. Chemical Characterizations Are Consistent with Previous Studies

The characteristics of both unmodified and POX modified conjugates were the same as in the previous reported [41]: molecular weight was $52 \times 10^3 \text{ g}\cdot\text{mol}^{-1}$ for MN-DOTAGd-IR800 (MN) and $71.2 \times 10^3 \text{ g}\cdot\text{mol}^{-1}$ for MN-pMeOx-DOTAGd-IR800 (MNOX); hydrodynamic radius in PBS was 3.3 nm for MN and 3.6 nm for MNOX. ζ -potential in PBS was -11.5 mV for MN and -6.7 mV for MNOX. Synthesis paths are shown in Figure S1.

2.2. MN Is Accumulated Inside the Cells in Higher Extent Than MNOX

For determination of subcellular localization of the applied mannan-based carriers 4T1 cells were incubated with a green fluorescent dye for lysosomes (LysoTracker[®] Green), a blue fluorescent dye for a nucleus and with the fluorescent mannan-based carrier bearing IR800CW as a red fluorescent dye. The confocal microscopy analysis showed that the cells incubated with MNOX had lower fluorescence signal from the red spectrum, this red fluorescent signal was conclusively caused by IR800CW conjugated on mannan-based polymers (Figure S2). The Pearson coefficient, which indicates the co-localization levels of red and green signals (IR800CW and LysoTracker[®] Green), was also lower in the case of MNOX (0.324 for MNOX and 0.428 for MN), reflecting lower accumulation of the POX-modified polymer in cells compared to the non-modified variant.

2.3. MTT Assay Showed That Mannan-Based Polymers Are Not Cytotoxic

Because all carriers intended for future use in drug delivery need to be non-toxic, we performed an MTT cytotoxicity assay. Results from the MTT assay indicated that mannan-based polymers had no negative influence on survival or proliferation of 4T1 cells (Figure 1). No difference was found between control and treated cells. Even the highest concentration used (4.5 mM Gd^{3+}) showed no statistically significant cytotoxic effect on cells (all p -values ≥ 0.05).

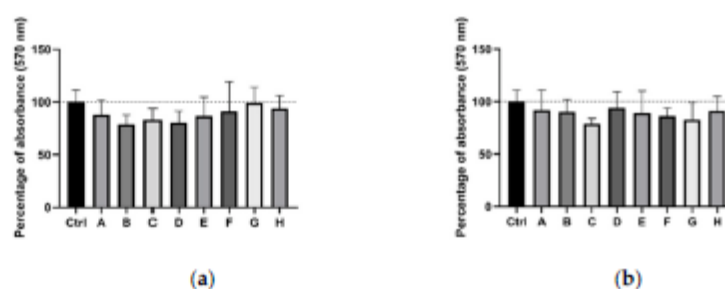


Figure 1. MTT assay results for 4T1 cells after 24 h of incubation with: (a) MN and; (b) MNOX. A-H represent different concentrations of MN and MNOX. Column A represents the highest concentration (4.5 mM Gd^{3+}) followed by fivefold serial dilution until the lowest concentration, represented by the H column. Data are displayed as a percentage of mean (\pm SD) absorbance ($n = 4$), 100% is the mean signal of untreated cells (controls-Ctrl).

2.4. Lymph Nodes on Tumor Site Showed Markedly Higher Fluorescence In Vivo Than Other Lymph Nodes

The analysis of the in vivo distribution, degradation and elimination rate of polymers were performed on tumor-bearing *Balb/c/c3H* mice. Animals were randomized into the three groups (MN, MNOX and DOT) after the tumors establishment. Fluorescence signal was measured repeatedly in several time-points after the injection of the mannan-based carriers. Data from these measurements showed the distribution of the mannan-based carriers in lymph nodes after absorption from the i.m. administration.

According to in vivo fluorescence optical imaging of the MN and MNOX groups (Figure 2), the highest signal issued from the inguinal lymph node next to the tumor and injection site (SLN) (Figure 3a, Figure S4a). The signal reached its maximum in both groups between the 4 and 24 hours after injection of MN or MNOX, one order of magnitude higher in the case of MN-DOTA Gd-IR800 (as with all other in vivo fluorescent signals). The second highest fluorescent signal measured originated from the liver (Figure 3e, Figure S4e), peaking at around 24 h after the injection of MN or MNOX and then continuously decreasing. This signal was again higher in the MN group. The DOT group had always a fluorescence signal lower than the background fluorescence signal.

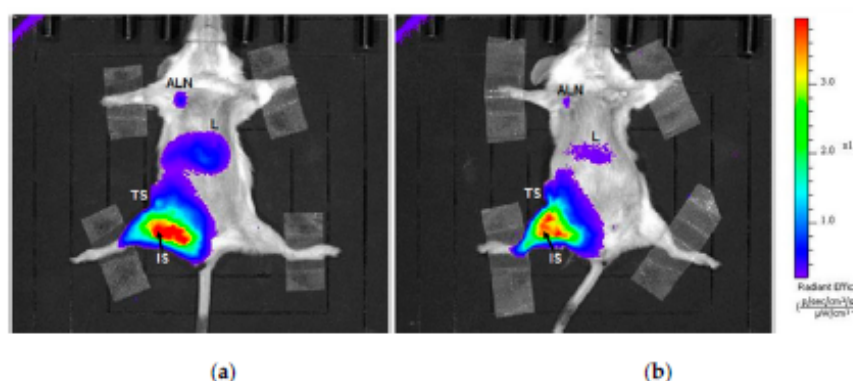


Figure 2. Representative images of in vivo fluorescence from (a) MN and (b) MNOX group. Fluorescent signals from axillary lymph nodes (ALN), livers (L), tumor sites (TS) and injection sites (IS). Images show mice three days after intramuscular injection of (a) MN or (b) MNOX.

We later detected the signal from the axillary lymph node on the tumor site (Figure 3b, Figure S4b), reaching its maximum 48 h after injection of MNOX (Figure S4b) and 72 h after injection of MN. The lowest fluorescent signal of all the measured lymph nodes issued from the axillary lymph node at a non-tumor site (Figure 3c, Figure S4c). However, the peak fluorescent signal from this lymph node was recorded only 2 h after administration of the contrast agent, a relatively short time span.

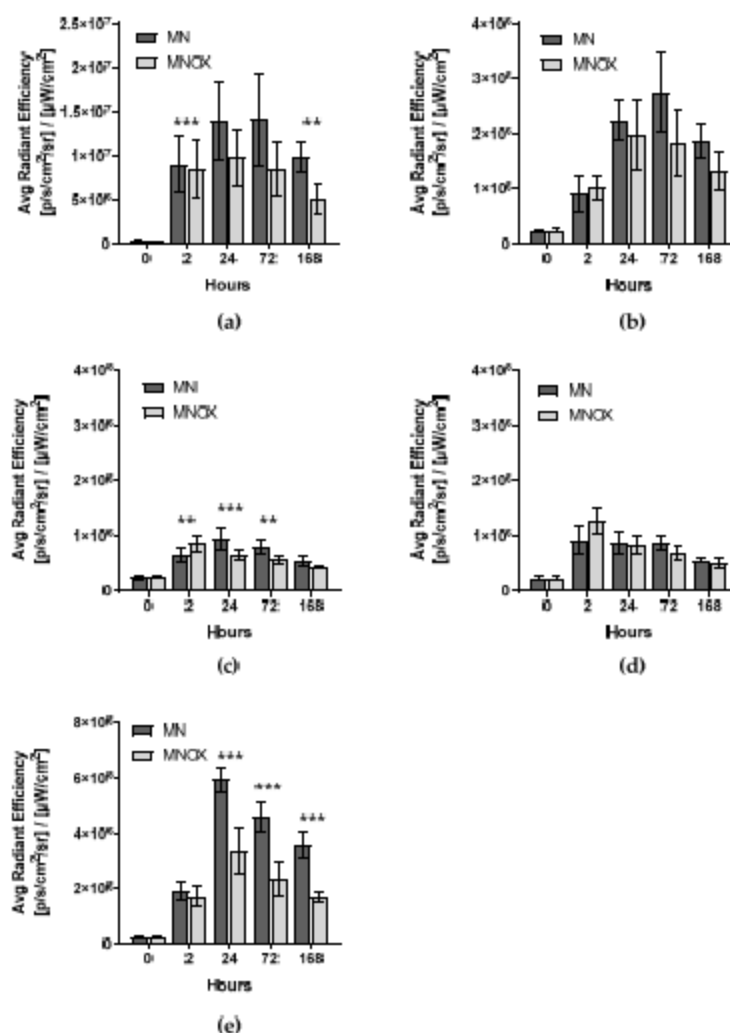


Figure 3. Quantification of fluorescence signals in different time intervals *in vivo*. Signals were quantified from (a) SLNs (inguinal lymph nodes on tumor site), (b) axillary lymph nodes on tumor sites, (c) axillary lymph nodes on non-tumor sites, (d) inguinal lymph nodes on non-tumor sites and (e) livers. The multiple one-tailed t-test was used for statistical evaluation ($n = 9$ for MN and $n = 9$ for MNOX). The fluorescent signal is represented as the average radiant efficiency (mean \pm SD), p -values: *** $p < 0.001$, ** $p < 0.01$, * $p < 0.05$.

2.5. Ex Vivo Fluorescence Signal from Internal Organs Decreased Progressively over Time

Due to the optical signal attenuation in the deeper organs (especially spleen and kidneys), the bio-distribution of the probes was assessed more precisely from *ex vivo* fluorescence signals (Figure 4, Figure S5). *Ex vivo* fluorescence signals from all organs decreased progressively over time (days 1, 3 and 7), with the exceptions of tumors and axillary and inguinal lymph nodes on tumor sites in the MNOX group. Fluorescence signal from *ex vivo* organs was higher for all organs from the MN group with two exceptions—tumors on day 3 and axillary lymph nodes on tumor sites on day 7. In these cases, fluorescence signal was higher in the MNOX group than in the MN group. In the MNOX

group, we observed lower fluorescence signals, especially from kidneys (Figure 4f), spleens (Figure 4g) and livers (Figure 4h). However, the trend of gradual decrease of fluorescence signal over time was the same as for the MN group. Fluorescent signal from tumors was the highest on day 1 in the MN group and on day 3 in the MNOX group (Figure 4e), pointing to the slowing of biodegradation due to POX conjugation. In the MNOX group, there was a slight delay in the accumulation of fluorescent probes inside tumors.

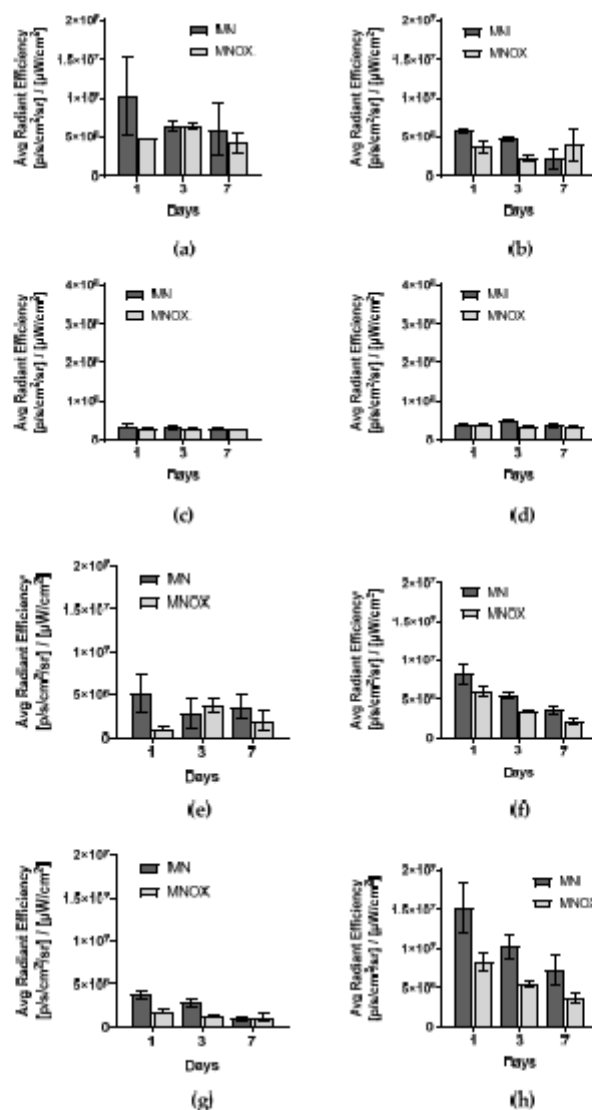


Figure 5. Quantification of ex vivo fluorescence signals. The fluorescence signal was quantified for (a) SLNs, (b) axillary lymph nodes on tumor sites, (c) axillary lymph nodes on non-tumor sites, (d) inguinal lymph nodes on non-tumor sites, (e) tumors, (f) kidneys, (g) spleens and (h) livers. Fluorescent signal is represented as the average radiant efficiency (mean ± SD). The multiple one-tailed t-test was used for statistical evaluation ($n = 9$ for MN and $n = 9$ for MNOX).

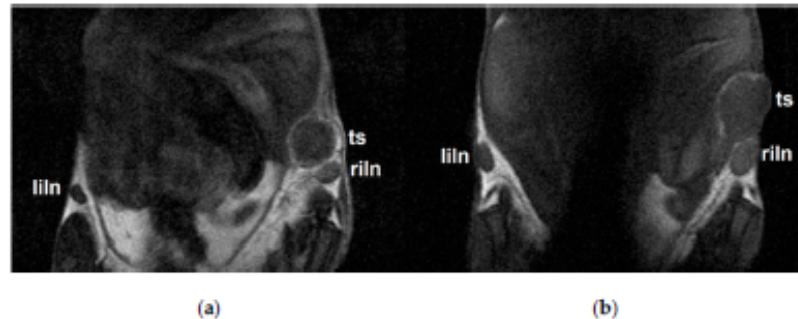


Figure 5. Representative coronal MR images measured three days after the injection of (a) MN or (b) MNOX into the right thigh muscle. Left inguinal lymph nodes (liln), tumors (ts) and right inguinal lymph nodes (riln) represent sites of polymer accumulation.

2.6. MRI Results Correlated with Results from In Vivo Fluorescence

As a complementary imaging method providing no attenuation of the signals in dependence to the tissue localization, we used a standard and non-invasive method routinely used both in experimental medicine and clinical practice: ^1H -MRI. Focusing on three anatomical sites—both inguinal lymph nodes and respective tumors (Figure 5)—MRI confirmed the results obtained from fluorescence imaging, namely preferential polymer accumulation in SLNs, with significantly higher uptake in animals in the MN and MNOX groups compared to the DOT group (Figure 6). This analysis revealed the highest accumulation in both inguinal lymph nodes in the MN group. The highest accumulation of mannan-based polymer carriers was observed 4 h after injection in the MN group and 24 h after injection in the MNOX group, comparable to fluorescence results. Although mannan-based polymer carrier accumulation in tumors was less prominent than in SLNs, accumulation inside tumors peaked approx. one hour after mannan-based polymer carrier injection (Figure 6c).

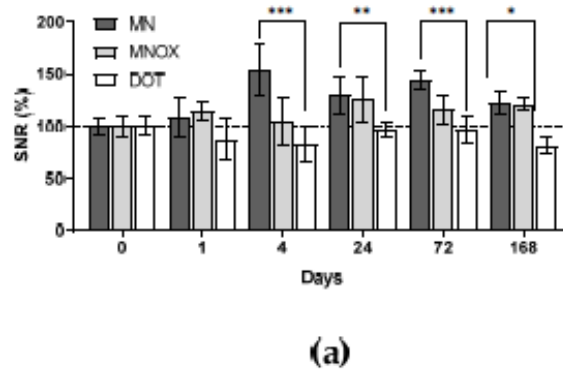
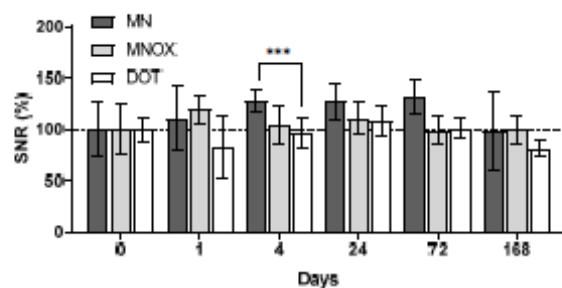
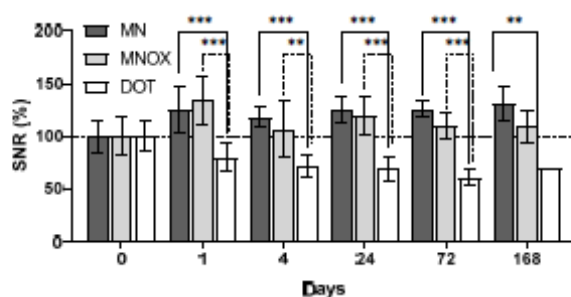


Figure 6. Cont.



(b)



(c)

Figure 6. Quantification of MR measurements. Results are presented as the SNR percentage mean \pm SD. Measurements performed before application of contrast agents are deemed 100%. Graphs show results from (a) inguinal lymph nodes on non-tumor sites, (b) inguinal lymph nodes on tumor sites (SLNs) and (c) tumors. The multiple one-tailed t-test was used for statistical evaluation ($n = 9$ for MN group, $n = 9$ for MNOX group and $n = 6$ for DOT group), p -values: *** $p < 0.01$, ** $p < 0.01$, * $p < 0.05$.

The imaging efficacy of the lower-molecular-weight MN probe was significantly higher compared to the higher-molecular-weight MNOX probe (modifying the same mannan with polyoxazoline increases the molecular weight of the conjugate). This might indicate the predominance of the targeting effect of the mannan-DC-SIGN receptor interaction compared to the less effective solid tumor-targeting EPR effect, as evidenced by the molecular weight of the conjugates.

2.7. Histology Did Not Find Any Pathologies in the Internal Organs after the Mannan Polymers Application

Histological analysis was performed in order to exclude pathological changes in the examined organs after the exposure to the mannan-based polymer carriers and to enable detailed monitoring of the induced tumors. No macroscopic or light-microscopic pathologies were observed for any of the investigated organs (Figure 7). Light microscopic examination revealed the preservation of tissue architecture, with no signs of dystrophic/degenerative change, necroinflammatory activity or fibrosis. No unexpected neoplastic processes were discernible in the organs examined (Figure 7(A1–A3),(B1–B3),(C1–C3)). Histological examination of the induced tumors revealed uncircumscribed masses composed of poorly differentiated, frankly atypical neoplastic cells with hyperchromatic nuclei, markedly in-

creased nucleo-cytoplasmic ratios, high mitotic activity, and atypical mitoses. Areas of coagulative necrosis were identified within neoplastic tissue.

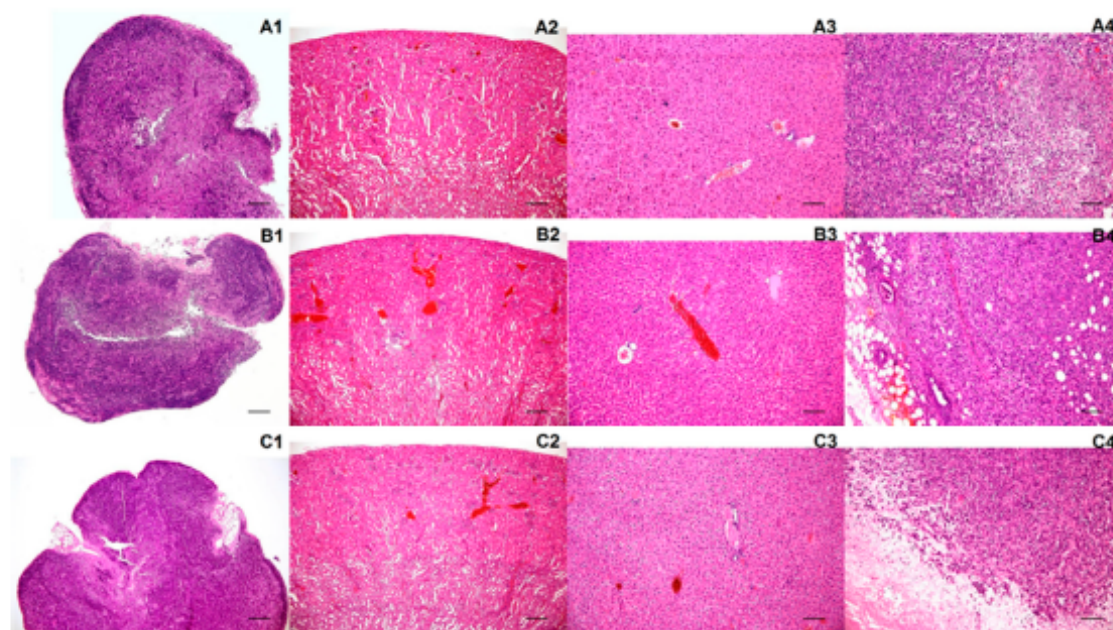


Figure 7. Representative histology images. Images represent (A1–A4) organs from MN-treated animals; (B1–B4) organs from MNOX-treated animals; (C1–C4) organs from animals treated with gadoterate meglumine. The following organs were analyzed: lymph nodes (A1,B1,C1), kidneys (A2,B2,C2), livers (A3,B3,C3) and tumors (A4,B4,C4). Hematoxylin-eosin staining; scale bars for A1–A3, B1–B3, C1–C3 represent 100× magnification, with those for A4, B4 and C4 representing 400× magnification.

3. Discussion

In this study, we tested a novel versatile platform based on mannan polymers that is intended for detection of SLNs infiltrated by metastasis and for tumor theranostics. We chose the 4T1 model, which is characterized by SLN infiltrated by metastatic cancer cells, a very common occurrence in breast cancer. Mannan-based polymers were modified with imaging probes for subsequent tracking. From a chemical point of view, the mannan-based probes were found to be stable, providing signals sufficient for both MRI and optical fluorescence imaging.

Confocal microscopy images showed lower fluorescent signals originating from MNOX carriers compared to carriers without polyoxazoline. MN and MNOX both co-localized with lysosomes to a similar extent; however, the Pearson coefficient of co-localization was lower in the case of the POX-modified conjugate due to lower intracellular uptake. The probe modified with POX seemed to exhibit lower endocytosis efficacy than MN without POX. This may have been caused partly by POX functionalization, which can hide mannan-based polymer carriers and thus preventing them from actively interacting with DC-SIGN receptors. POX functionalization can also affect the endocytosis rate. Previous studies focusing on other types of chemical functionalization (dextrin succinylation [33,34] or PEGylation [42]) have documented similar results.

In vivo multimodal imaging of mice with syngeneic tumors confirmed in vitro results. The overall higher in vivo fluorescence signals of MN in the lymph nodes and liver most likely indicates higher accumulation of the polymer without POX. This tallies with our

hypothesis and with previous studies which have shown that POX prolongs polymer circulation time, decreases accumulation in internal organs, and renders polymers less visible to the immune system [33,34]. Lower accumulation in organs such as the liver, kidneys and spleen, is beneficial because it diminishes the unwanted effects in off-target organs. On the other hand, a disadvantage of the modification is that the accumulation is also reduced in tumor and lymph nodes. Assisted by passive targeting via the EPR effect, MN offers stronger primary active targeting than MNOX because of its high affinity with DC-SIGN receptors. This is of no small importance given that DC-SIGN receptors are present on macrophages, especially those inside SLNs, the most common site of primary metastasis. Active targeting of this problematic site is therefore recommended, even at early stages of tumorigenesis. Our mannan-based polymer with POX seemed to have less availability of mannose for DC-SIGN receptors and slightly lower content of IR800CW. Further analysis is required to precisely equilibrate the dose of POX in this mannan-based conjugate to maximize its potential benefits, namely lower accumulation in organs, but still preserve the strong tumor- and lymph node-targeting properties.

Although polymers were accumulated mostly in SLNs, we also observed accumulation in other lymph nodes. The extent of accumulation in distant lymph nodes enabled us to monitor the spreading of our probe through lymphatic drainage. In accordance with fluorescence imaging, MRI measured direct signals from SLNs without signal contamination from the injection site and confirmed preferential uptake of mannan-based conjugates in lymph nodes compared to that offered by the commercially available MR contrast agent, gadoterate meglumine.

Ex vivo fluorescence signals from organs (liver, spleen, kidneys) decreased over time in the case of both mannan-based conjugates, a trend that indicates the gradual degradation and elimination of our polymer carriers. Degradation and elimination were slower for the POX probe, a finding that corresponds with other *in vivo* studies of natural polysaccharide-based conjugates [33,34]. Gradual biodegradation and elimination should prove beneficial characteristics for future clinical applications [43]. However, fluorescence signal activity in tumor and lymph nodes proved different. The decrease in fluorescence signal was not continuous for the MNOX group in the case of SLNs, ALNs on tumor sites, or tumors. Additionally, in both *in vivo* and *ex vivo* applications, the fluorescence signal from MN probes were higher with two exceptions: axillary lymph nodes on tumor sites on day 7 and tumors on day 3, where MNOX exhibited a higher fluorescence signal. These results may be due to the effect of POX, namely slower cell uptake, diminished biodegradation and prolonged circulation time.

Importantly, our results confirm the biocompatibility and non-toxicity of mannan-based carriers. The MTT assay results conclusively support our hypothesis that mannan-based polymers are non-toxic even when tested at maximum concentrations. Histological examination confirmed our mannan-based polymer carriers had no adverse effects on internal organs. As previously shown, Gd^{3+} can have a negative effect when cleaved from its structure [44–47]; however, as Gd^{3+} was chelated in mannan-based conjugate, its toxic effect was excluded. Furthermore, Gd^{3+} chelates are approved and routinely used for medical purposes, which suggests that our carriers could be easily implemented in clinical practice.

The polymers described here might not only serve as a diagnostic aid for tumors and metastasis but also as a beneficial therapeutic option. In future, drugs might be chemically incorporated into these polymers to serve as efficient drug delivery systems via local drug release in response to various stimuli (e.g., pH).

4. Materials and Methods

4.1. Chemistry

Mannan-based conjugates were prepared as described in [41]. Briefly, mannan was modified in two different ways to obtain conjugate bearing a fluorescent label and a probe for MRI.

The first approach was focused on the synthesis of polysaccharide-based conjugate without polyoxazoline in the structure (Figure S1a). The modification procedure was started by allylation of commercial mannan to obtain allyl groups-containing derivative. It was further reacted with cysteamine via thiol-click reaction introducing primary amino groups. This primary amino group-containing mannan was then conjugated with N-hydroxysuccinimide (NHS) esters of infra-red dye (IR800CW NHS-ester) and 1,4,7,10-tetraazacyclododecane-1,4,7,10-tetraacetic acid (DOTA NHS-ester). Finally, the obtained product reacted with gadolinium (III) chloride to chelate Gd^{3+} , resulting in mannan-based conjugate with the fluorescence and MR imaging labels, denoted as MN-DOTAGd-IR800 (in short version-MN).

Synthetic approach for preparation of mannan-based conjugate with grafted polyoxazoline chains was analogous to MN-DOTAGd-IR800 (Figure S1b). After dissolution in anhydrous DMSO, mannan sodium alkoxide was reacted with living poly(2-methyl-2-oxazoline) chains, obtained by ring-opening cationic polymerization. As allyl bromide was used for the polymerization of the polyoxazoline, the grafts contained terminal allyl groups which were then modified in the same way as described above for MN-DOTAGd-IR800. The polyoxazoline-containing conjugate was denoted as MN-pMeOx-DOTAGd-IR800 (in short version-MNOX).

4.2. Cell Line

For all in vitro and in vivo experiments, 4T1 cells (ATCC[®] CRL-2539[™], Prague, Czech Republic) were used. The cells were incubated under standard conditions (37 °C, 5% CO₂) in Roswell Park Memorial Institute (RPMI) 1640 incubation medium without phenol red supplemented with fetal bovine serum, L-glutamine and penicillin/streptomycin. RPMI 1640 incubation medium was purchased from Gibco[®] by LifeTechnologies[™] (Waltham, MA, USA).

RPMI 1640 incubation medium without phenol red was chosen in order to minimize background during fluorescent microscopy measurement. Fetal bovine serum that was added to RPMI 1640 media to final concentration 10% was purchased from Gibco[®] by LifeTechnologies[™]. L-Glutamine (stock solution 200 mM) and penicillin/streptomycin (stock solution containing 10,000 units of penicillin and 10 mg of streptomycin per 1 mL) were added to the RPMI 1640 media at a final concentration of 5%. Both L-glutamine and penicillin/streptomycin were purchased from Sigma-Aldrich Ltd. (Prague, Czech Republic).

The RPMI 1640 incubation medium without phenol red supplemented with fetal bovine serum, L-glutamine and penicillin/streptomycin was used as a medium for all experiments with 4T1 cell line (confocal microscopy, MTT cytotoxicity assay).

4.3. Confocal Microscopy

The 4T1 cells (0.1×10^6 /mL) were plated in an 8-well Nunc[™] Lab-Tek[™] II Chambered Coverglass dish (Thermo Scientific[™], Waltham, MA, USA) with a No. 1.5 borosilicate glass bottom. In their exponential phase of growth, cells were incubated for 24 h in media with a 4.5 mM Gd^{3+} concentration of mannan-based polymers. After the incubation period, cells were washed twice with Hank's balanced salt solution (HBSS, Biosera, Nuaille, France), with fluorescent dyes added in concentrations according to the producer's manual (60–70 nM for LysoTracker[®] Green and 1 µg/mL for Hoechst 33342). Incubation times were 60 min for LysoTracker[®] Green and 20 min for Hoechst 33,342 [48,49]. All fluorescent dyes were purchased from Invitrogen[™] by Life-Technologies (Prague, Czech Republic). After incubation, the cells were washed twice with HBSS followed by the addition of RPMI 1640 medium without phenol red. Cells were then measured under a TCS SP8 STED 3× microscope (Leica, Chicago, IL, USA; objective: HC PL APO CS2 100×/1.40 OIL). Images were displayed with automatically enhanced contrast and adjusted for brightness using ImageJ (version 1.46r, National Institutes of Health, Bethesda, MD, USA).

4.4. MTT Cytotoxicity Assay

The MTT (3-(4,5-dimethylthiazol-2-yl)-2,5-diphenyltetrazolium bromide) assay was performed according to a standard protocol [50]. For the cytotoxicity test, the 4T1 cell line (incubated in RPMI 1640 medium without phenol red supplemented with fetal bovine serum, L-glutamine and penicillin/streptomycin) was used at a concentration of 0.01×10^6 /mL. The highest concentration of the tested sub-stance (4.5 mM of Gd^{3+}) was used to reflect the optimal concentration for all other *in vitro* experiments. Fivefold serial dilution of the initial concentration was used to prepare other samples. After 24 h of incubation with the mannan-based polymers (MN or MNOX), cells were washed with HBSS before adding 200 μ L of fresh media, and then incubated for another 5 days. The medium was removed followed by the addition of the MTT solution (5 mg/mL in RPMI 1640, 250 μ L per well) for 6 h. The MTT solution was then replaced with dimethyl sulfoxide (DMSO, 200 μ L per well) and glycine buffer (30 μ L per well). Absorbance at 570 nm was immediately measured on the Multi-Mode Reader (Synergy™ 2, BioTek® Instruments, Inc., Burlington, VT, USA), with tests performed in tetraplicate. Both MTT and DMSO were purchased from Sigma-Aldrich, Ltd.

4.5. Animal Model

For all *in vivo* measurements, female 5-week-old *Balb/c*3H mice were used. With this animal strain, syngeneic tumors can be induced by injecting 4T1 cells. The animals (purchased from Velaz Ltd., Prague, Czech Republic) were kept under a standard day/night cycle (12/12 h) and given free access to food and water. All protocols were approved by the Ethics Committee of the Institute for Clinical and Experimental Medicine, with all experiments carried out in accordance with European Union Council Directive 2010/63/EU.

4.6. Tumor Induction

4T1 cells were chosen for tumor induction. The cell line originates from the mammary gland of *Mus musculus* (*Balb/c*3H strain), representing an animal stage IV human breast cancer. These cells allow syngeneic tumor induction in *Balb/c*3H mice and can form metastases from primary tumors. Additionally, tumors formed from 4T1 cells have homogeneous regions, which are beneficial for imaging and subsequent quantification.

Tumors were induced in *Balb/c*3H mice by an injection of $0.30 \pm 0.05 \times 10^6$ 4T1 cells suspended in 50 μ L PBS into the right abdominal mammary gland. Cells were harvested under standard conditions (37 °C, % CO₂). On the day of the injection, cells were trypsinized, centrifuged, counted, diluted in PBS at the desired concentration, and then injected into the anesthetized animals, which were kept under inhalation anesthesia using isoflurane (5% for induction, 2% during the surgery).

When tumors reached at least 2 mm in diameter (assessed by MRI), the animals were divided into three groups: MNOX group-*i.m.* administration with MN-pMeOx-DOTAGd-IR800 (n = 9); MN group-*i.m.* administration with MN-DOTAGd-IR800 (n = 9); DOT control group-*i.m.* administration with gadoterate meglumine, a clinically approved contrast agent (n = 6). Gadoterate meglumine was chosen as a control due to its common use in clinical practice thus the signal mannan-based conjugates could be directly compared to widely use contrast agent.

The probes (50 μ L dose) were injected into the right thigh muscle at an 18 mM Gd^{3+} concentration per ml (0.05361 mg IR800CW per ml in case of MN or 0.04932 mg IR800CW per ml in case of MNOX). 18 mM Gd^{3+} concentration gives signal that is strong enough for measurement with 4.7 T MR scanner and subsequent analysis.

4.7. Fluorescence Imaging

IVIS® Lumina XR optical imager (PerkinElmer Inc., Waltham, MA, USA) (excitation filter: 745 nm, emission filter: 810–875 nm) was used for *in vivo* experiments. The animals were scanned (exposure time: 60 s) at several time points: before, immediately, and then 2, 4, 6, 24, 48, 72 and 168 h after the injection. After fluorescence imaging, animals were

measured by MRI (except at the 48-h time point). Two animals from each group were sacrificed on the 1st and 3rd day and five animals on the 7th day after the polymer injection. Fluorescent signals from organs (liver, kidneys, spleen, lymph nodes and tumors) were also measured to determine level of fluorescence in these sites.

4.8. Magnetic Resonance Imaging

MRI examination was carried out on a 4.7 T MR scanner (Bruker BioSpin, Ettlingen, Germany) using a homemade surface coil. T1-weighted axial and coronal MR images of mouse calf muscles and lymph nodes were acquired via standard two-dimensional rapid acquisition and the relaxation enhancement (RARE) multispin echo sequence using the following parameters: repetition time TR = 339 ms, effective echo time TE = 12 ms, turbo factor 2, spatial resolution $0.16 \times 0.16 \times 0.70 \text{ mm}^3$, scan time 8 min 40 s. Data were analyzed and presented as percentages of the signal- (from the appropriate lymph node or tumor mass) to-noise ratio (SNR), with values measured before probe application at 100%.

4.9. Histology

Livers, kidneys, SLNs and tumors were analyzed histologically. Two mice from each group (MN, MNOX and DOT) were randomly chosen for analysis. Mice were sacrificed by anesthesia overdose 7 days after polymer application. After a thorough macroscopic inspection, internal organs (kidneys, livers, lymph nodes) as well as tumor tissue were fixed in 4% formaldehyde and routinely processed for histological examination. Sections ($4\mu\text{m}$) were stained with hematoxylin and eosin (HE) and the Verhoeff-van Gieson protocol to highlight collagen and elastic fibers.

4.10. Statistical Methods

The R 3.6.2 a language and environment for statistical computing (R Foundation for Statistical Computing, Vienna, Austria) was used for statistical analysis of MTT assay data using linear mixed-effects model (lme4 package). For fluorescence in vivo imaging and MRI the multiple t-test in GraphPad Prism 8 (GraphPad Software, Inc., San Diego, CA, USA) was used.

5. Conclusions

We showed in this article the diagnostic potential of the mannan-based probes for SLNs in a relevant fully immunocompetent tumor animal model. The conjugates were accumulated in vitro inside 4T1 cells and in vivo after intramuscular administration in the lymph nodes and internal organs of mice. No toxic effects were observed, the conjugates proved highly biocompatible. The probes were preferentially accumulated in SLNs and tumors in the same animal model. Fluorescence imaging confirmed the biodegradability of the probes (with or without POX modification). Considering the promising potential of polymer conjugates as a precise and efficient theranostic multimodal imaging modality, the next step will be to test their application in various anti-cancer drug systems. The binding with various anti-cancer drugs targeted to specific cancer subtype could overcome the limitation of the mannan-based probes (targeting to DC-SIGN only), increase their efficiency and conjugated anti-cancer drugs could benefit from the mannan-based probes versatility, targeting via EPR effect and possibility of local anti-cancer drug release in response to various stimuli (which would depend on the type of conjugation). Therefore, these combinations could form a very promising various drug delivery systems based on the mannan copolymer platform which have been presented and described in this article.

Supplementary Materials: The following are available online, Figure S1: Synthesis paths for mannan modification, Figure S2: Representative confocal microscopy images, Figure S3: Change in fluorescence signal in vivo in time (representative example), Figure S4: Quantification of in vivo fluorescence signals (all time points), Figure S5: Representative example of ex vivo fluorescence signal on day 3 (after the application of MN/MNOX).

Author Contributions: Conceptualization, D.J. and M.H.; synthesis of the mannan based polymers, M.R.; methodology MRI, A.G.; methodology in vitro and in vivo fluorescence M.J.; histology analyses, E.S.; writing—original draft preparation, M.J.; writing—review and editing, D.J.; supervision, D.J. All authors have read and agreed to the published version of the manuscript.

Funding: This research was funded by the Grant Agency of the Ministry of Health, Czech Republic (grant number 16-30544a (MH)), MH CR-DRO (Institute for Clinical and Experimental Medicine IKEM, IN00023001), the Czech Science Foundation (grant number 18-07983S) and the Charles University Grant Agency (project No. 282216).

Institutional Review Board Statement: All protocols were approved by the Ethics Committee of the Institute for Clinical and Experimental Medicine, with all experiments carried out in accordance with European Union Council Directive 2010/63/EU.

Informed Consent Statement: Not applicable.

Data Availability Statement: The data presented in this study are available on request from the corresponding author.

Acknowledgments: We wish to thank the Light Microscopy Core Facility, IMG ASCR, Prague, Czech Republic, supported by MEYS (LM2015062, CZ.02.1.01/0.0/0.0/16_013/0001775), OPVK (CZ.2.16/3.1.00/21547) and MEYS (LO1419) for their support with the confocal and image analyses and to Vera Lanska, CSc. for support with the statistical analysis.

Conflicts of Interest: The authors declare no conflict of interest.

Sample Availability: Samples of the compounds are available from the authors upon reasonable request.

References

1. Veronesi, U.; Paganelli, G.; Viale, G.; Luini, A.; Zurrada, S.; Galimberti, V.; Intra, M.; Veronesi, P.; Robertson, C.; Maisonneuve, P.; et al. A randomized comparison of sentinel-node biopsy with routine axillary dissection in breast cancer. *N. Engl. J. Med.* **2003**, *349*, 546–553. [\[CrossRef\]](#) [\[PubMed\]](#)
2. Lyman, G.H.; Giuliano, A.E.; Somerfield, M.R.; Benson, A.B., 3rd; Bodurka, D.C.; Burstein, H.J.; Cochran, A.J.; Hiram, S.C., 3rd; Edge, S.B.; Galper, S.; et al. American Society of Clinical Oncology guideline recommendations for sentinel lymph node biopsy in early-stage breast cancer. *J. Clin. Oncol.* **2005**, *23*, 7703–7720. [\[CrossRef\]](#)
3. Qiu, S.Q.; Zhang, G.J.; Jansen, L.; de Vries, J.; Schroder, C.P.; de Vries, E.G.E.; van Dam, G.M. Evolution in sentinel lymph node biopsy in breast cancer. *Crit. Rev. Oncol. Hematol.* **2018**, *123*, 83–94. [\[CrossRef\]](#)
4. Karaman, S.; Detmar, M. Mechanisms of lymphatic metastasis. *J. Clin. Investig.* **2014**, *124*, 922–928. [\[CrossRef\]](#) [\[PubMed\]](#)
5. Evertsson, M.; Kjellman, P.; Cinthio, M.; Andersson, R.; Tran, T.A.; In't Zandt, R.; Grafström, G.; Toftvall, H.; Fredriksson, S.; Ingvar, C.; et al. Combined Magnetomotive ultrasound, PET/CT, and MR imaging of (68)Ga-labelled superparamagnetic iron oxide nanoparticles in rat sentinel lymph nodes in vivo. *Sci. Rep.* **2017**, *7*, 4824. [\[CrossRef\]](#) [\[PubMed\]](#)
6. Dong, Y.; Feng, Q.; Yang, W.; Lu, Z.; Deng, C.; Zhang, L.; Lian, Z.; Liu, J.; Luo, X.; Pei, S.; et al. Preoperative prediction of sentinel lymph node metastasis in breast cancer based on radiomics of T2-weighted fat-suppression and diffusion-weighted MRI. *Eur. Radiol.* **2018**, *28*, 582–591. [\[CrossRef\]](#) [\[PubMed\]](#)
7. Krischer, B.; Forte, S.; Niemann, T.; Kubik-Huch, R.A.; Leo, C. Feasibility of breast MRI after sentinel procedure for breast cancer with superparamagnetic tracers. *Eur. J. Surg. Oncol.* **2018**, *44*, 74–79. [\[CrossRef\]](#)
8. Garcia-Urbe, A.; Erpelding, T.N.; Krumholz, A.; Ke, H.; Maslov, K.; Appleton, C.; Margenthaler, J.A.; Wang, L.V. Dual-Modality Photoacoustic and Ultrasound Imaging System for Noninvasive Sentinel Lymph Node Detection in Patients with Breast Cancer. *Sci. Rep.* **2015**, *5*, 15748. [\[CrossRef\]](#)
9. Joseph, E.J.; van Oepen, A.; Friebe, M. Breast sentinel lymph node biopsy with imaging towards minimally invasive surgery. *Biomed. Tech.* **2017**, *62*, 547–555. [\[CrossRef\]](#)
10. Jain, R.; Dandekar, P.; Patravale, V. Diagnostic nanocarriers for sentinel lymph node imaging. *J. Control. Release* **2009**, *138*, 90–102. [\[CrossRef\]](#)
11. Mantovani, A.; Schioppa, T.; Porta, C.; Allavena, P.; Sica, A. Role of tumor-associated macrophages in tumor progression and invasion. *Cancer Metastasis Rev.* **2006**, *25*, 315–322. [\[CrossRef\]](#) [\[PubMed\]](#)
12. Sica, A.; Schioppa, T.; Mantovani, A.; Allavena, P. Tumour-associated macrophages are a distinct M2 polarised population promoting tumour progression: Potential targets of anti-cancer therapy. *Eur. J. Cancer* **2006**, *42*, 717–727. [\[CrossRef\]](#) [\[PubMed\]](#)
13. Ezekowitz, R.A.; Williams, D.J.; Kozziel, H.; Armstrong, M.Y.; Warner, A.; Richards, F.F.; Rose, R.M. Uptake of *Pneumocystis carinii* mediated by the macrophage mannose receptor. *Nat. Cell Biol.* **1991**, *351*, 155–158. [\[CrossRef\]](#) [\[PubMed\]](#)
14. Garcia-Vallejo, J.J.; van Kooyk, Y. The physiological role of DC-SIGN: A tale of mice and men. *Trends Immunol.* **2013**, *34*, 482–486. [\[CrossRef\]](#)

15. Hu, J.; Wei, P.; Seeberger, P.H.; Yin, J. Mannose-Functionalized Nanoscaffolds for Targeted Delivery in Biomedical Applications. *Chem. Asian J.* **2018**, *13*, 3448–3459. [[CrossRef](#)]
16. Lepenies, B.; Lee, J.; Sonkaria, S. Targeting C-type lectin receptors with multivalent carbohydrate ligands. *Adv. Drug Deliv. Rev.* **2013**, *65*, 1271–1281. [[CrossRef](#)]
17. Feinberg, H.; Mitchell, D.A.; Drickamer, K.; Weis, W.I. Structural basis for selective recognition of oligosaccharides by DC-SIGN and DC-SIGNR. *Science* **2001**, *294*, 2163–2166. [[CrossRef](#)]
18. Feinberg, H.; Castelli, R.; Drickamer, K.; Seeberger, P.H.; Weis, W.I. Multiple modes of binding enhance the affinity of DC-SIGN for high mannose N-linked glycans found on viral glycoproteins. *J. Biol. Chem.* **2007**, *282*, 4202–4209. [[CrossRef](#)]
19. Guo, Y.; Feinberg, H.; Conroy, E.; Mitchell, D.A.; Alvarez, R.; Blixt, O.; Taylor, M.E.; Weis, W.I.; Drickamer, K. Structural basis for distinct ligand-binding and targeting properties of the receptors DC-SIGN and DC-SIGNR. *Nat. Struct. Mol. Biol.* **2004**, *11*, 591–598. [[CrossRef](#)]
20. Yong, S.B.; Chung, J.Y.; Song, Y.; Kim, J.; Ra, S.; Kim, Y.H. Non-viral nano-immunotherapeutics targeting tumor microenvironmental immune cells. *Biomaterials* **2019**, *219*, 119401. [[CrossRef](#)]
21. Gardner, A.; Ruffell, B. Dendritic Cells and Cancer Immunity. *Trends Immunol.* **2016**, *37*, 855–865. [[CrossRef](#)] [[PubMed](#)]
22. Chiang, C.L.; Kandalafi, L.E. In vivo cancer vaccination: Which dendritic cells to target and how? *Cancer Treat. Rev.* **2018**, *71*, 88–101. [[CrossRef](#)] [[PubMed](#)]
23. Buckeridge, M.S. Seed cell wall storage polysaccharides: Models to understand cell wall biosynthesis and degradation. *Plant Physiol.* **2010**, *154*, 1017–1023. [[CrossRef](#)] [[PubMed](#)]
24. Edwards, M.; Scott, C.; Gidley, M.J.; Reid, J.S. Control of mannose/galactose ratio during galactomannan formation in developing legume seeds. *Planta* **1992**, *187*, 67–74. [[CrossRef](#)] [[PubMed](#)]
25. Pauly, M.; Gille, S.; Liu, L.; Mansoori, N.; de Souza, A.; Schultink, A.; Xiong, G. Hemicellulose biosynthesis. *Planta* **2013**, *238*, 627–642. [[CrossRef](#)] [[PubMed](#)]
26. Dos Santos, M.A.; Grønha, A. Polysaccharide nanoparticles for protein and Peptide delivery: Exploring less-known materials. *Adv. Protein Chem. Struct. Biol.* **2015**, *98*, 223–261. [[CrossRef](#)]
27. Zia, F.; Zia, K.M.; Zuber, M.; Ahmad, H.B.; Muneer, M. Glucomannan based polyurethanes: A critical short review of recent advances and future perspectives. *Int. J. Biol. Macromol.* **2016**, *87*, 229–236. [[CrossRef](#)]
28. Fang, J.; Nakamura, H.; Maeda, H. The EPR effect: Unique features of tumor blood vessels for drug delivery, factors involved, and limitations and augmentation of the effect. *Adv. Drug Deliv. Rev.* **2011**, *63*, 136–151. [[CrossRef](#)]
29. Taurin, S.; Nehoff, H.; Greish, K. Anticancer nanomedicine and tumor vascular permeability; Where is the missing link? *J. Control. Release* **2012**, *164*, 265–275. [[CrossRef](#)]
30. Barar, J.; Omid, Y. Dysregulated pH in Tumor Microenvironment Checkmates Cancer Therapy. *Bioimpacts* **2013**, *3*, 149–162. [[CrossRef](#)]
31. Omid, Y.; Barar, J. Targeting tumor microenvironment: Crossing tumor interstitial fluid by multifunctional nanomedicines. *Bioimpacts* **2014**, *4*, 55–67. [[CrossRef](#)] [[PubMed](#)]
32. Sindhwani, S.; Syed, A.M.; Ngai, J.; Kingston, B.R.; Maiorino, L.; Rothschild, J.; Macmillan, P.; Zhang, Y.; Rajesh, N.U.; Hoang, T.; et al. The entry of nanoparticles into solid tumours. *Nat. Mater.* **2020**, *19*, 566–575. [[CrossRef](#)] [[PubMed](#)]
33. Duncan, R.; Gilbert, H.R.; Carbajo, R.J.; Vicent, M.J. Polymer masked-unmasked protein therapy. 1. Bioresponsive dextrin-trypsin and -melanocyte stimulating hormone conjugates designed for alpha-amylase activation. *Biomacromolecules* **2008**, *9*, 1146–1154. [[CrossRef](#)] [[PubMed](#)]
34. Hreczuk-Hirst, D.; Chicco, D.; German, L.; Duncan, R. Dextrins as potential carriers for drug targeting: Tailored rates of dextrin degradation by introduction of pendant groups. *Int. J. Pharm.* **2001**, *230*, 57–66. [[CrossRef](#)]
35. Luxenhofer, R.; Han, Y.; Schulz, A.; Tong, J.; He, Z.; Kabanov, A.V.; Jordan, R. Poly(2-oxazoline)s as polymer therapeutics. *Macromol. Rapid Commun.* **2012**, *33*, 1613–1631. [[CrossRef](#)]
36. Amoozgar, Z.; Yeo, Y. Recent advances in stealth coating of nanoparticle drug delivery systems. *Wiley Interdiscip. Rev. Nanomed. Nanobiotechnol.* **2012**, *4*, 219–233. [[CrossRef](#)]
37. Pidhatika, B.; Rodenstein, M.; Chen, Y.; Rakhmatullina, E.; Muhlebach, A.; Agikgoz, C.; Textor, M.; Konradi, R. Comparative stability studies of poly(2-methyl-2-oxazoline) and poly(ethylene glycol) brush coatings. *Biointerphases* **2012**, *7*, 1. [[CrossRef](#)]
38. Grube, M.; Leiske, M.N.; Schubert, U.S.; Nischang, I. PCx as an Alternative to PEG? A Hydrodynamic and Light Scattering Study. *Macromolecules* **2018**, *51*, 1905–1916. [[CrossRef](#)]
39. Yang, Q.; Lai, S.K. Anti-PEG immunity: Emergence, characteristics, and unaddressed questions. *Wires Nanomed. Nanobiotechnol.* **2015**, *7*, 655–677. [[CrossRef](#)]
40. Zhang, P.; Sun, F.; Liu, S.J.; Jiang, S.Y. Anti-PEG antibodies in the clinic: Current issues and beyond PEGylation. *J. Control. Release* **2016**, *244*, 184–193. [[CrossRef](#)]
41. Rabyk, M.; Galisova, A.; Jiratova, M.; Patsula, V.; Srbova, L.; Loukotova, L.; Parnica, J.; Jirak, D.; Stepanek, P.; Hruby, M. Mannan-based conjugates as a multimodal imaging platform for lymph nodes. *J. Mater. Chem. B* **2018**, *6*, 2584–2596. [[CrossRef](#)]
42. Suk, J.S.; Xu, Q.; Kim, N.; Hanes, J.; Ensign, L.M. PEGylation as a strategy for improving nanoparticle-based drug and gene delivery. *Adv. Drug Deliv. Rev.* **2016**, *99 Pt A*, 28–51. [[CrossRef](#)]
43. Naahidi, S.; Jafari, M.; Edalat, F.; Raymond, K.; Khademhosseini, A.; Chen, P. Biocompatibility of engineered nanoparticles for drug delivery. *J. Control. Release* **2013**, *166*, 182–194. [[CrossRef](#)]

44. Oh, N.; Park, J.H. Endocytosis and exocytosis of nanoparticles in mammalian cells. *Int. J. Nanomed.* **2014**, *9* (Suppl. 1), 51–63. [CrossRef]
45. Chang, Y.; Lee, G.H.; Kim, T.J.; Chae, K.S. Toxicity of magnetic resonance imaging agents: Small molecule and nanoparticle. *Curr. Top. Med. Chem.* **2013**, *13*, 434–445. [CrossRef]
46. Zhou, Z.; Lu, Z.R. Gadolinium-based contrast agents for magnetic resonance cancer imaging. *Wiley Interdiscip. Rev. Nanomed. Nanobiotechnol.* **2013**, *5*, 1–18. [CrossRef]
47. Lansman, J.B. Blockade of current through single calcium channels by trivalent lanthanide cations. Effect of ionic radius on the rates of ion entry and exit. *J. Gen. Physiol.* **1990**, *95*, 679–696. [CrossRef]
48. LysoTracker® and LysoSensor™ Probes. 2018. Available online: <https://www.thermofisher.com/document-connect/document-connect.html?url=https://assets.thermofisher.com/TFS-Assets/LSG/manuals/mp07525.pdf&title=THlzblRyYWNrZXIgaW5kIEEx5c29TZW5zb3IgaUJvYmVz> (accessed on 11 November 2018).
49. Hoechst Stains. 2018. Available online: <https://www.thermofisher.com/document-connect/document-connect.html?url=https://assets.thermofisher.com/TFS-Assets/LSG/manuals/mp21486.pdf&title=SG9lY2hzdCBTdGFpbmM=> (accessed on 11 November 2018).
50. Freshney, R.L. *Culture of Animal Cells: A Manual of Basic Technique and Specialized Applications*; Wiley: Hoboken, NJ, USA, 2011.